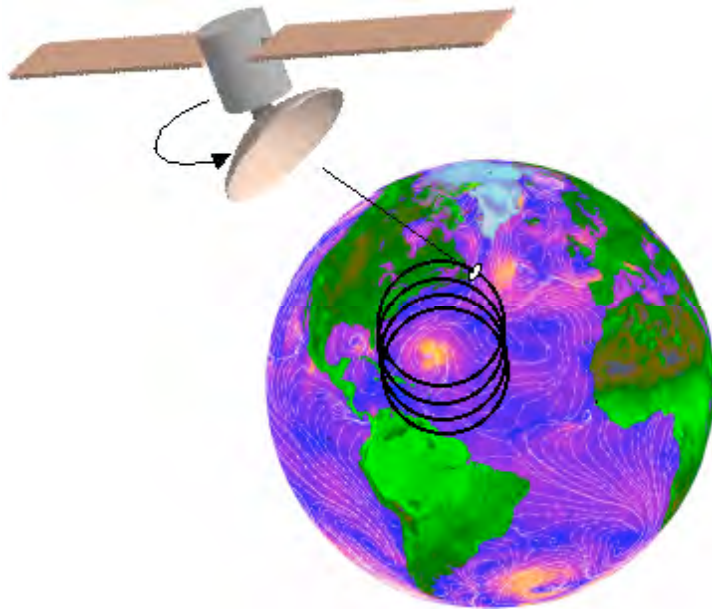




# Medium Earth Orbit Scatterometer (MEOScat) Concept Phase-I Study

*Study Lead: Michael Spencer*



**National Aeronautics and  
Space Administration**

**Jet Propulsion Laboratory  
California Institute of Technology  
Pasadena, California**

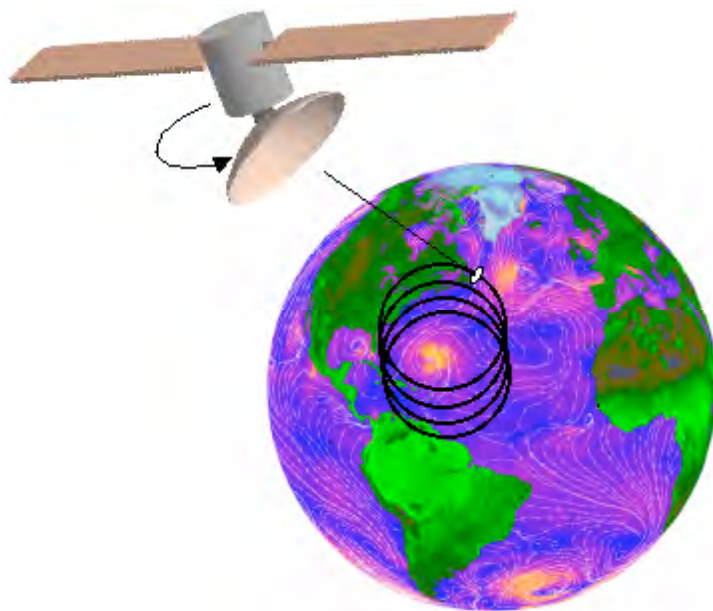
---

*March 2004*



# Medium Earth Orbit Scatterometer (MEOScat) Concept Phase-I Study

*Study Lead: Michael Spencer*



**National Aeronautics and  
Space Administration**

**Jet Propulsion Laboratory  
California Institute of Technology  
Pasadena, California**

---

*March 2004*

## **Acknowledgment**

This publication was prepared at the Jet Propulsion Laboratory,  
California Institute of Technology, under a contract with  
the National Aeronautics and Space Administration.

## TABLE OF CONTENTS

Introduction, Phase I Study .....	1
1. Performance Guidelines for NASA Next-Generation Scatterometer Concept Study.	3
1.1 Overview .....	3
1.2 Published OVW Requirements .....	3
1.3 Current and Future OVW Measurement Capabilities .....	5
1.4 Adopted Guidelines for Next-Generation Scatterometer Study.....	7
1.5 References .....	9
2. Scatterometer Measurement Requirements and Constraints .....	10
2.1 Overview .....	10
2.2 Scatterometer Measurement Fundamentals and Definitions.....	11
2.3 Spaceborne Scatterometer Model Functions.....	13
2.4 Model Function Sensitivity vs. Incidence Angle .....	14
2.5 Transmit Frequency Trade-Offs .....	15
2.5.1 Wind Sensitivity to Frequency .....	15
2.5.2 Rain Sensitivity.....	22
2.5.3 Transmit Frequency Guidelines For Trade-Off Studies.....	25
2.6 Incidence Angle Range .....	25
2.7 Polarimetric Radar Channels.....	27
2.7.1 Polarimetric Radar Theory .....	27
2.7.2 Polarimetric Radar Measurements.....	30
2.7.3 Polarimetric Radar Channel Conclusions .....	31
2.8 Radiometer Channels.....	31
2.8.1 Rain Detection and Correction Techniques.....	31
2.8.2 Polarimetric Radiometer Channels .....	33
2.8.3 Radiometer Channel Conclusions.....	34
2.9 Scatterometer Measurement Duration Issues.....	35
2.10 References .....	37
3. Scatterometer Instrument Concept Trade-Offs .....	40
3.1 Fan-Beam Systems .....	40
3.2 Pencil-Beam Systems .....	41
3.3 Other Scatterometer Beam Architectures .....	44
3.4 Architecture Trade-Offs and Baseline Architecture for Study.....	45
4. Orbit Trade-Offs.....	50
4.1 Overview .....	50
4.2 Single Satellite Orbit Trade-Offs.....	50
4.2.1 Orbit Analysis Methodology .....	51
4.2.2 Single Spacecraft Analysis Results.....	59
4.2.3 Summary of Single Satellite Revisit and Coverage Characteristics .....	61
4.3 Multiple Spacecraft (Constellation) Coverage Results.....	79
4.3.1 Single MEOScat Spacecraft Plus Single ASCAT on METOP .....	79
4.3.2 Multiple MEO Sensors.....	80
4.4 Radiation Considerations .....	86

5.	MEOScat System Design Parameter Trade-Offs.....	89
5.1	Antenna/Altitude Trade-off Study.....	89
5.1.1	System Geometry and Real-Aperture Resolution.....	89
5.1.2	Ambiguity Constraints and SAR Processing.....	92
5.1.3	Antenna Rotation Rate Issues.....	95
5.1.4	Imaging Times and Measurement Duration.....	97
5.2	Strawman Antenna Design Examples.....	98
5.3	Scatterometer Measurement Accuracy .....	102
5.4	References .....	108
6.	Conically-Scanning Antenna Design Trade-Offs .....	110
6.1	General Antenna Design Characteristics .....	110
6.2	Conically-Scanning Antenna Design Options.....	113
6.3	References .....	117
7.	Summary, Conclusions, and Recommendations.....	118
7.1	Study Summary .....	118
7.2	Recommendations for Future Work .....	119
	Appendix A.....	121

## Phase-I Study Introduction

This report summarizes the results of the MEOScat Phase-I Study. The goal of the study is to identify initial concept options for a next generation wind scatterometer system to operate in the post-SeaWinds timeframe. In order to meet the future requirements of scientific and operational users, a variety of approaches for improving wind vector products (relative to previous systems) are examined. Special emphasis is placed on addressing concept options that operate at higher altitudes in order to improve the temporal revisit time.

For this study, a “top down” approach is adopted:

1. *Survey science and operational requirements.* First, the wind vector needs of the science and operational user communities are surveyed. Because convening a science/operational user group to define the requirements was beyond the scope of the Phase-I study (such a group has been formed for future study phases), the general science/operational needs are assessed by examination of published requirements from operational agencies, examination of technical and position papers from the science community, and informal discussions with members of the science and operational communities. From these efforts, a set of general requirement guidelines is adopted to steer the instrument concept studies in order to address the most important wind requirements anticipated for the future.
2. *Specify scatterometer measurement requirements and constraints.* In order to accurately infer vector winds from measurements of radar backscatter, a series of fundamental conditions must be met. These conditions are referred to as “measurement requirements,” and include constraints on the transmit frequency, polarization, sensor geometry, etc. The specification of measurement requirements is critical because they form a set of geophysically-based “ground rules” for insuring that the scatterometer concepts considered will have the essential characteristics to allow the accurate retrieval of sea surface winds.
3. *Identify candidate instrument architectures.* With the science requirements and measurement requirements specified, the next step is to survey the variety of instrument architectures that could be utilized to meet these requirements. Past scatterometer systems have used a range of very different approaches – “fan-beam” systems were used for NSCAT and ERS-1,2, as opposed to a “pencil-beam” system which was employed for SeaWinds. The advantages and disadvantages of each architecture are considered, and a baseline architecture is selected as the primary subject of further study.
4. *Orbit studies.* After the instrument architecture, the most significant factor in determining the mission characteristics is the orbit. In general, the higher the orbit, the wider the swath, and the better the temporal revisit characteristics. A comprehensive trade-off study is performed for a single scatterometer system

operating in any orbit from 800 km (the altitude of current systems) and higher. For the Phase-I study, the emphasis is on a single satellite, but some key features of multi-satellite constellations will also be considered. The important issue of the more severe radiation environment encountered at higher orbits will be addressed.

5. *Instrument system requirements.* The instrument system requirements – in terms of the antenna size required, the transmit power required, etc. – will change as a function of altitude. To quantify this, a series of high-level instrument trade-off equations and curves are produced. These design curves are useful in assessing what technologies are required to operate in a given orbit.
6. *Antenna design options.* The primary goal of the Phase-I study is to identify scatterometer concept options and provide a preliminary assessment of their associated technology implications. Because of the dominant role the antenna plays in determining the scatterometer performance, risk, and cost; additional analysis is performed on the antenna implementation options.

After summarizing the results of the above analyses, the Phase-I report concludes with recommendations for promising areas that deserve more detailed design studies. Again, the MEOScat Phase-I study is just the initial effort in what is envisioned to be a series of studies leading to the selection of a specific instrument concept to be developed for flight.

The study team was multidisciplinary, with contributions from the following individuals:

Study Lead: Michael Spencer (JPL)  
Science Consultant Leads: Michael Freilich (OSU), Timothy Liu (JPL)  
System Engineering: Adam Freedman (JPL), Andrew Gerber (JPL)  
Measurement Requirements: Scott Dunbar (JPL)  
Orbit Analysis: Francois Rogez (JPL), Scott Dunbar (JPL)  
Mechanical Engineering: David Otth (JPL)  
Antenna Engineering: Aluizio Prata (USC), Yahya Ramat-Samii (UCLA)  
Radiation Environment: J. Martin Ratliff (JPL), Suzanne Thompson (JPL)

Additional contributions from Mark Thompson at NGC Astro and Greg Konicke of Spectrum Astro are also gratefully acknowledged.

# **1. Performance Guidelines for NASA Next-Generation Scatterometer Concept Study**

## **1.1 Overview**

The primary goal of this study is to investigate and develop concept options for a more capable “next-generation” NASA scatterometer to operate in the post-SeaWinds timeframe. A critical first step is thus to establish what operational and science needs for ocean vector winds (OVWs) will exist in the post-Seawinds era. These needs will be used to form a set of guidelines that will define both the minimum and desired performance of a next-generation system, and also define the trade-space boundaries as various concept options are considered. Generating such a set of guidelines is critical to insuring that the various concept options identified by this study address future science and operational needs.

The following approach is adopted: First, a survey of published OVW measurement requirements that reside in existing documentation is performed. Such documents include official requirements generated by operational agencies (such as the Integrated Operational Requirements Document, or IORD, for example), position papers from workshops and conferences, and refereed journal articles. Second, a survey of other, non-NASA OVW sensors that are slated to be in operation during the post-SeaWinds timeframe is performed. Clearly, the contributions of a NASA next-generation scatterometer must be considered in light of the other capabilities that will exist during the same timeframe, and should be synergistic with them. Finally, after a review of the above information, a set of general performance guidelines will be developed to govern and steer the study of concept options for a next-generation system. Ideally, each step in this process is reviewed by individuals who are intimately familiar with the operational and science communities, who in turn are the ultimate customers for the OVW product.

It should be noted that, in recent years, scatterometer data has found wide utility not just in ocean vector winds applications, but in land and cryospheric research as well. Such applications include sea ice extent and classification, iceberg tracking, soil moisture, flooding, and monitoring of the Greenland and Antarctic ice sheets. Our approach will be to focus on the improvement of OVW measurements, and address these other applications as secondary considerations. In general, the improvement of scatterometer OVW performance (improved revisit, resolution, etc.) will result in an improvement of the product for these other applications as well.

## **1.2 Published OVW Requirements**

A key document in articulating the OVW needs of the operational community is the revised Integrated Operational Requirements Document, IORD-II. The IORD-II is a compilation of requirements both from NOAA and DoD that guide the development of National Polar-orbiting Operational Environmental Satellite System (NPOESS). For the



purposes of this study, we shall regard the relevant sections of the IORD-II as an authoritative statement of both the minimum and desired OVW measurement capability by the operational community in the timeframe that a post-SeaWinds mission would fly. A selected set of key IORD-II requirements for OVW's is shown in Table 1-1. The requirements shown were selected because of their impact on the instrument system design.

**Table 1-1: Operational OVW requirements and current/future OVW system requirements.**

Performance Parameter	IORD-II Requirements		Current/Future Planned Instrument Measurement Requirements		
	Threshold	Objective	SeaWinds	ASCAT/Metop	CMIS (Threshold only)
Resolution	20 km	1 km	25 km	50 km (routine) 25 km (capability)	20 km
Measurement Range	3–25 m/s	1–50 m/s	3–30 m/s (not to preclude 50 m/s)	4– 24 m/s	3–25 m/s
Speed Accuracy	Greater of 2 m/s or 10%	Greater of 1 m/s or 10%	2 m/s for 3–20 m/s 10% for 20–30 m/s	2 m/s (or 10%)	Greater of 2 m/s or 20%
Direction Accuracy	20° (for wind speed > 5 m/s) 25° (for wind speed 3–5 m/s)	10° (for wind speed > 3 m/s)	20°	20°	20°
Refresh	6 hours	1 hour	<i>19 hr at equator (see Note 1)</i>	<i>27 hr at equator (see Note 1)</i>	<i>(see Note 2)</i>
Geographic Coverage	Global ice-free ocean	Global ice-free ocean	Global ice-free ocean	Global ice-free ocean	Global ice-free ocean

**Note 1:** No specific refresh requirement is given for these sensors. These values for SeaWinds and ASCAT are as calculated in (Milliff, et al. 2001) (see Figure 1) for the case where each sensor is operating alone.

**Note 2:** CMIS refresh will be consistent with that achieved with the required swath width and the number of NPOESS platforms operating by a given date.

Some additional points can be drawn from the IORD-II document. The requirements are not specifically for a single sensor on a single spacecraft, but could be met by multiple sensors including non-NPOESS assets (IORD-II, p. 1). The “refresh” requirement specifies the maximum value of the local revisit time over the set of all locations on the Earth’s surface (IORD-II, p. GII-9). Related to this is a stated desire to obtain contiguous data for successive swaths near the equator for tropical storm forecasting (IORD-II, p. 9). Although it is recognized that current sensor technology may have difficulty in meeting the wind speed and direction requirements in the presence of rain, it is nevertheless desired that the requirements be satisfied even under such adverse conditions (IORD-II, p. RCM-II-5). The data latency requirements of between 90 minutes (threshold) and 15

minutes (objectives) are also important for ensuring the utility of the OVW product (IORD-II, p. 19).

Other published statements of requirements for OVW are largely consistent with the IORD. In the tropics, there is a desire to have refresh rates sufficient to observe the diurnal cycle, and ideally at a rate of every 6 hours (Milliff et al. 2001 and M. Freilich, personal communication). At mid-latitudes, the refresh rate should at least be sufficient to resolve the inertial cycle, corresponding to a sampling rate of roughly 6-12 hours, depending on latitude (Milliff et al. 2001). The desirability to avoid “gaps” in the swath coverage for tropical storms is stated (Isaksen and Stofflen, 2000). Significantly for the instrument design, a minimum resolution of 25 km is considered crucial for addressing storms and key coastal processes (Quilfen et al. 1998), with resolution better than 10 km considered highly desirable for observing key features internal to tropical cyclones (Yueh et al. 2001; T. Liu, personal communication).

### ***1.3 Current and Future OVW Measurement Capabilities***

The last three columns of Table 1-1 describe the required capabilities of OVW measurement systems that are planned to operate in the 2003+ timeframe:

SeaWinds is a conically scanning Ku-Band scatterometer with a total measurement swath width of 1800 km. SeaWinds has a nominal resolution of 25 km, but, taking advantage of the high range resolution available with radars, winds posted at 12.5 km resolution have been demonstrated with good results. SeaWinds has been demonstrated to meet the stated requirements over the majority of this swath, with some degradation in performance at the outer swath edges and near nadir. Because Ku-Band is particularly sensitive to precipitation, degradation in performance also occurs under rainy conditions. Two SeaWinds instruments are currently operating in orbit. SeaWinds on QuikSCAT was launched in June of 1999. The QuikSCAT spacecraft has exceeded its design life, and it is unclear to what extent technical or programmatic considerations will allow future continuation of the mission. SeaWinds on ADEOS-II was launched in December of 2002, and the initiation of calibrated data release occurred in October 2003. The required design life of the SeaWinds/ADEOS-II mission is a minimum of 3 years, but sufficient propellant exists for a 5-year mission.

ASCAT (Advanced Scatterometer) is a C-Band scatterometer built by the European Space Agency (ESA) and will fly on the Metop series of satellites. Metop is a polar orbiting weather satellite. Three Metop platforms are planned, each with a five year mission life. One will be launched every five years, with the first launch planned for 2005, for a total of 15 years of coverage (i.e., nominally out to 2020). ASCAT is a dual-swath instrument (similar to the Ku-Band NSCAT instrument flown in 1996-97), and is an improved version of the successful single-swath scatterometers flown on the ERS-1 and ERS-2 missions. ASCAT has two swaths, each up to 550 km wide, with a 660 km gap centered on the subsatellite track.

The CMIS (Conical-Scanning Microwave Imager Sounder) instrument will fly on the NPOESS platform and obtain a variety of environmental parameters, including wind speed and direction. CMIS will use a single-look, passive radiometer polarimetric technique, rather than the traditional multi-look, active scatterometer technique employed by SeaWinds and ASCAT, to determine the wind vector. The recently launched WINDSAT mission is designed to test the validity of this approach from space. NPOESS will be launched as necessary to replace the current polar orbiting weather platforms. The first CMIS/NPOESS launch is expected to occur no earlier than 2009-2010.

Examining Table 1-1, all three sensors are required to meet (or very nearly meet) the IORD “threshold” requirement for resolution, but are far from meeting the “objective.” Based on several years of on-orbit data from SeaWinds/QuikSCAT and ERS-1,2; we conclude that SeaWinds and ASCAT will meet (or, again, very nearly meet) the threshold requirements on wind measurement range, speed accuracy, and direction accuracy. The capability of CMIS to likewise meet these requirements is, as stated, currently in the process of being validated. The IORD objective requirement of accurately measuring winds up to the very high speed of 50 m/s appears to be a challenge given the current technology, although some recent research indicates that this is possible with the SeaWinds scatterometer (see Yueh et al. 2001).

The issue of refresh rate for current and planned scatterometer systems has been examined by (Milliff et al. 2001), the results of which are shown in Figure 1-1. First, note that a single scatterometer system (whether SeaWinds or ASCAT) by itself has relatively poor sampling – between 19 and 27 hours at the equator. When contemporaneously operating scatterometer systems are considered as a constellation – either a combination of SeaWinds/ADEOS-II and ASCAT or SeaWinds/ADEOS-II and SeaWinds/QuikSCAT – the revisit time is observed to improve significantly, although not yet achieving the ideal revisit time at low latitudes. When the full three-satellite constellation of CMIS/NPOESS sensors are in orbit, a refresh rate not quite achieving the desired 6 hours will be achieved.

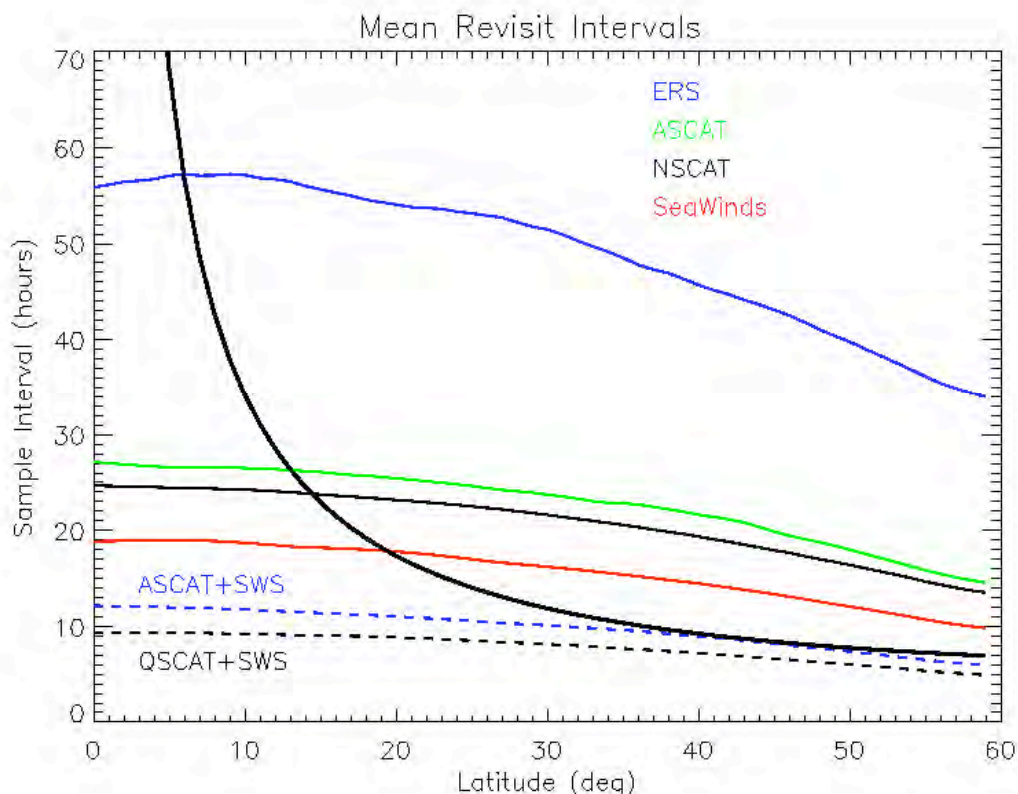


**Figure 1-1: Mean time between samples vs. latitude for current and planned scatterometer systems (also NSCAT). SWS is an abbreviation for SeaWinds. A dark solid line indicates a timescale approximately twice the local inertial period as a function of latitude (from Milliff, et al.).**

#### **1.4 Adopted Guidelines for Next-Generation Scatterometer Study**

Reviewing the preceding information, an overall comparison of the desired performance and the anticipated sensor capabilities indicates that some key requirements will not be met. Even when we consider a constellation including both the SeaWinds and ASCAT instruments, the best scatterometer revisit time at the equator is approximately 12 hours, and is double the 6 hours desired for producing weather forecasts at the desired frequency and for resolving the diurnal cycle in the tropics. Although spatial resolution capabilities meet the minimal requirements, further improving the resolution -- ultimately towards the objective requirement of 1 km -- enables a variety of new operational and scientific applications. In coastal regions, large wind gradients are observed to exist over spatial scales of 5-10 km. Higher resolution wind measurements are desired in such conditions to meet DoD tactical requirements and NOAA requirements for forecasting marine hazard events (IORD-II, p. RCM-II-26). In addition, the modeling community now utilizes mesoscale numerical prediction models with nested grids down to 4 km. Higher

resolution data are critical for the accurate initialization and data assimilation of these models (IORD-II, p. RCM-II-27). Winds at horizontal scales of  $\leq 10$  km are also needed for the resolution of band structure and the eye of hurricanes, for observing topographically induced features such as Von Kármán vortices, for the study of phenomena related to coastal upwelling, and for observing processes adjacent to the ocean/sea ice interface.

We therefore develop a set of requirement guidelines in order to govern the next-generation scatterometer concept study. These guidelines address both minimum acceptable performance for such a system, and improved capabilities to be explored.

***Refresh/Coverage:*** Follow-on scatterometer concepts that significantly improve the refresh rate beyond the capabilities of current sensors will be explored. This will involve the consideration of higher altitude orbits and wider swaths. An area of particular focus will be systems that improve the revisit statistics and swath coverage in the important tropical latitudes. In performing this analysis, the complementary coverage of other planned sensors, such as ASCAT/Metop, shall be taken into account, effectively making these other sensors components of a future constellation. Consequently it is allowable for the NASA next-generation mission, taken alone, to either systematically exclude or otherwise undersample a given region (high latitudes for example) in order to improve the overall refresh characteristics of the constellation. Because the first CMIS is not expected to fly until 2009-2010 at the earliest, for the purposes of this study the potential complementary coverage contributed by CMIS shall not be considered in the revisit analysis.

***Spatial Resolution:*** In order to meet the minimum operational and science requirements, a next-generation system must be able to generate winds with at least 25 km resolution, with the capability to produce special wind products posted on a 12.5 km grid. This requirement has a significant impact on the concept study because it dictates the minimum antenna length required for a given orbital altitude. Beyond this minimum requirement, system concepts will be explored that achieve better than 10 km resolution for tropical storm analyses, and, ideally, even approaching the 1 km resolution specified in the IORD objectives.

***Wind Vector Retrieval Range and Accuracy:*** In order to meet operational and scientific needs, the measurement range, wind speed accuracy, and direction accuracy must be at least those specified in the IORD threshold requirements and/or that required of current scatterometer designs (which are all similar levels of performance). In cases where spatial resolution higher than 25 km is achieved, somewhat worse performance may be allowed for some wind speeds (lower speeds, for example), but the desired requirements must be still be met over the entire wind speed range when these products are averaged up to 25 km. To address key goals for a next-generation system, design concepts that either extend the measurement range beyond that achieved with current systems, or improve performance under precipitating conditions will be explored as part of this study.

## 1.5 References

CMIS 2001, “Conical Scanning Microwave Imager/Sounder (CMIS) Sensor Requirements Document,” Version Three, Integrated Program Office, March 2, 2001.

Gelsthorpe, R.V., E. Schied, J.J.W. Wilson, “ASCAT – Metop’s Advanced Scatterometer,” ESA Bulletin No. 102, May 2000.

Isaksen, L. and Stoffelen, A., “ERS Scatterometer Wind Impact on ECMWF’s Tropical Cyclone Forecasts, *IEEE Trans. on Geosci. and Remote Sensing* , 38, pp. 1885-1892, 2000.

Liu, W.T., “Progress in Scatterometer Application,” *Journal of Oceanography*, Vol. 58, pp. 121-136, 2002.

Milliff, R.F., Freilich, M.H., Liu, W.T., Atlas, R., and Large, W.G., “Global Ocean Surface Vector Wind Observations from Space.” In *Observing the Oceans in the 21st Century*, C.J. Koblinsky and N.R. Smith (Eds), pp. 102-119, 2001.

NPOESS 2001, “NPOESS Integrated Operational Requirements Document (IORD-II),” Joint Agency Requirements Group, December 10, 2001.

Quilfen, Y., Chaperon, B., Elfouhaily, T., Katsaros, K., and Tournadre, J., “Observation of Tropical Cyclones by High Resolution Scatterometry, *J. Geophys. Res.*, 103, pp. 7767-7786, 1998.

Yueh, S.H., Stiles, B.W., Tsai, W-Y., Hu, H., and Liu, W.T., “QuikSCAT Geophysical Model Function for Tropical Cyclones and Application to Hurricane Floyd,” *IEEE Trans. on Geosci. and Remote Sensing*, Vol. 39, No. 12, pp. 2601-2612, December 2001.

## 2. Scatterometer Measurement Requirements and Constraints

### 2.1 Overview

In Section 1, the science goals for a future scatterometer system were discussed. Another area that places fundamental constraints on the instrument concept study is the measurement approach – i.e., the phenomenology associated with backscatter from the ocean surface and its relationship to the wind vector. Measurement approach questions to be addressed in this section include:

*What is the best frequency (or frequencies) to employ?* A key question is how sensitive the backscatter is to changes in wind speed and direction at different transmit frequencies. Another fundamental trade-off is that lower frequencies are less sensitive to precipitation, but higher frequencies allow the use of smaller antennas to achieve the same resolution.

*What is the acceptable range of incidence angles for making scatterometer measurements of the wind vector?* This question will impact the largest swath available to a given scatterometer architecture and will, in turn, impact the refresh period.

*What is the potential of radar polarimetry to improve scatterometer performance and ease instrument accommodation on the spacecraft?* Simulation and limited aircraft experiments have demonstrated that polarimetric scatterometry has the potential to alleviate some of the problems associated with achieving multiple azimuth measurements of the surface.

*What are the requirements on a collocated radiometer measurement for rain detection and correction?* At higher scatterometer frequencies, rain may contaminate the measurement. Radiometer measurements may be used both to detect and correct for the influence of precipitation. Because passive measurements of the sea surface are also sensitive to the wind, the potential also exists to use radiometer measurements more directly in determining the wind vector.

*Based on ocean wind phenomenology, what is the maximum time allowable between different azimuth measurements of the surface?* In order to measure the wind vector, a scatterometer typically measures the backscatter from a given point on the surface from different azimuth directions as it flies by. The time between these measurements is a function of the orbit ground speed, swath width and number of feeds, and will consequently grow longer as higher altitudes are considered.

This section addresses these questions and issues, and furthers defines the concept trade-space that will meet the desired wind performance.

## 2.2 Scatterometer Measurement Fundamentals and Definitions

The normalized backscatter cross-section of the ocean's surface,  $\sigma_0$ , is well modeled by the following expression:

$$\sigma_0 = A_0(U, \theta, P) + A_1(U, \theta, P)\cos(\phi) + A_2(U, \theta, P)\cos(2\phi),$$

where  $U$  is the neutral stability wind at a given height,  $\theta$  is the incidence angle of the radar signal on the surface,  $P$  is the polarization with respect to the surface,  $\phi$  is the measurement azimuth angle defined with the respect to the upwind direction. This relationship is often referred to as the *Geophysical Model Function*. In Figure 2-1, the Ku-Band model function is plotted versus measurement azimuth for different polarizations, incidence angles, and wind speeds. Note that the  $A_0$  coefficient largely determines the magnitude of  $\sigma_0$  as a function of wind speed, the  $A_1$  coefficient represents the upwind/downwind modulation, and the  $A_2$  coefficient represents the upwind/cross wind modulation.

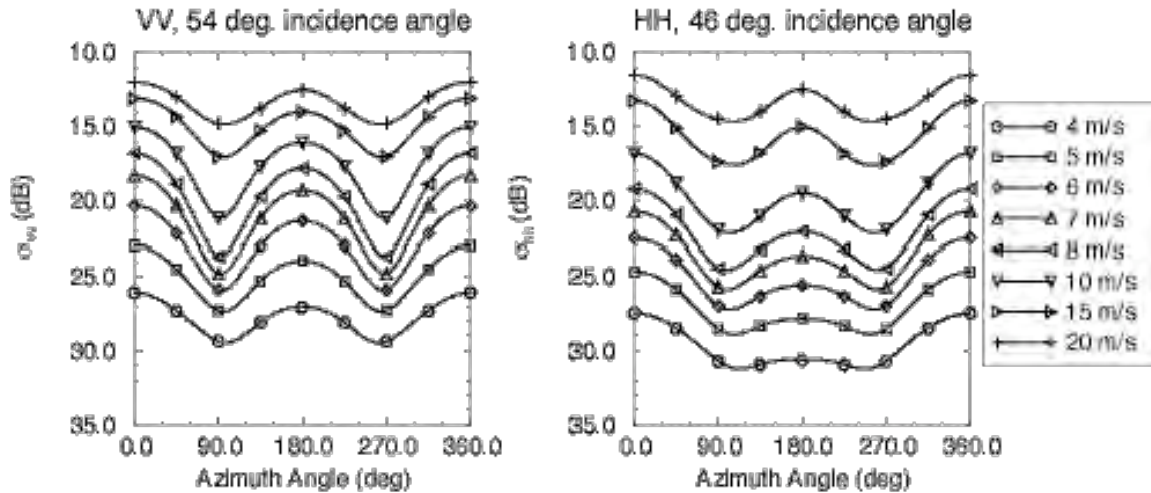
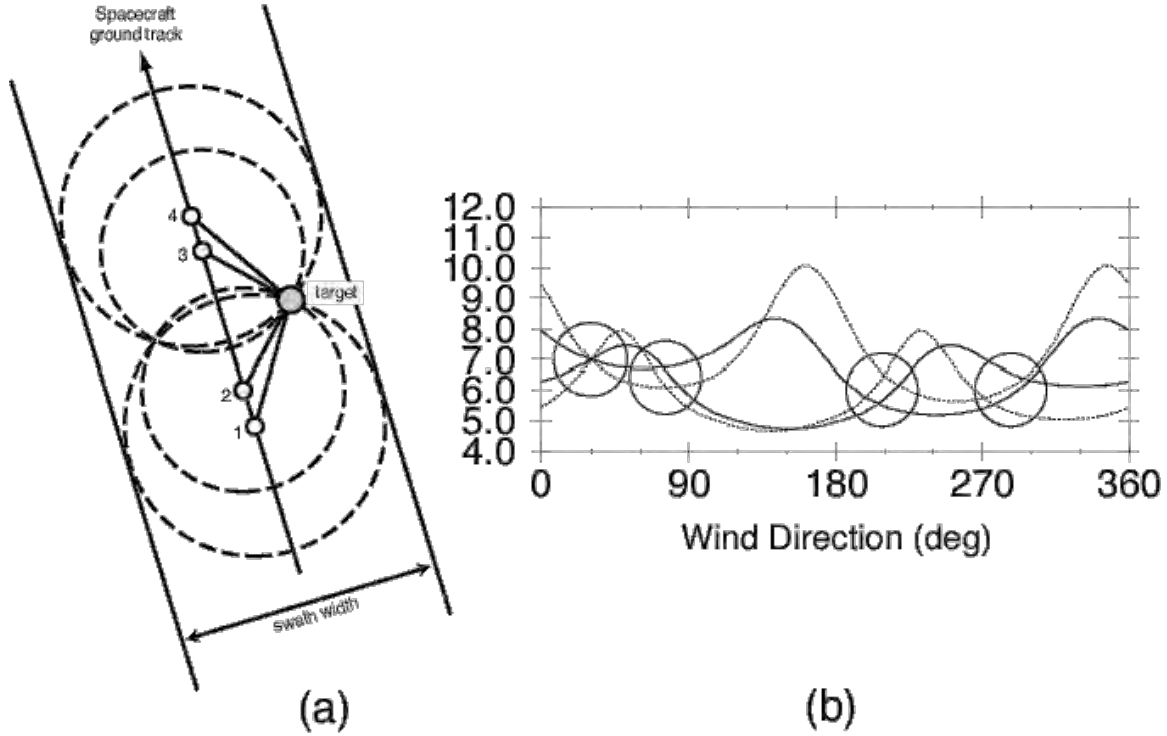


Figure 2-1: Sample Ku-Band model function plots.

In order to determine the wind vector, the ocean surface is measured from multiple azimuth angles as the spacecraft flies by (see Figure 2-2a). Given a set of measured  $\sigma_0$ 's, and knowing  $\theta$ ,  $P$ ,  $A_0$ ,  $A_1$ , and,  $A_2$ ; the equation above can be solved for the wind speed  $U$  and direction  $\phi$  using an estimation algorithm such as least squares or maximum likelihood. This process is illustrated conceptually in Figure 2-2b, where possible wind vector solutions are plotted as curves in  $U$ - $\phi$  space for each of four measurements made at different azimuth angles. The point where all the curves intersect represents the correct solution. Note that, in order to determine a unique solution, measurements of the surface must be made from at least three distinct azimuth angles. Other points where the curves



nearly intersect are known as wind “ambiguities” because they may be mistaken for correct solutions when the  $\sigma_0$  measurements are noisy. In general, the accuracy of the wind retrieval is a function of the noise on the  $\sigma_0$  measurements, the geometry of the measurements, and the sensitivity of the solutions as determined by the parameters  $A_0$ ,  $A_1$ , and,  $A_2$ .



**Figure 2-2: a) Diagram of how a conically scanning system such as SeaWinds makes the multiple azimuth angle measurements required for wind retrieval. Backscatter cross-section is measured at multiple azimuth angles (in this case, 4) as the spacecraft flies past. b) Sample plot of wind retrieval process from four azimuth measurements. Circles indicate ambiguities, with true solution at 7 m/s and 30°.**

The RMS error associated with the measurement of  $\sigma_0$ ,  $\Delta\sigma_0$ , is typically defined as

$$\Delta\sigma_0 = K_p \sigma_0,$$

where the  $K_p$  parameter is the normalized standard deviation of the measurement, and is thus defined by

$$K_p = \frac{\sqrt{\text{Var}[\sigma_0]}}{\sigma_0}.$$

For a radar measurement, the  $K_p$  parameter is, in general, given by

$$K_p = \sqrt{K_{pr}^2 + K_{pc}^2},$$

where  $K_{pr}$  is the normalized standard deviation of the calibration error and  $K_{pc}$  is the radar precision due to random fading and noise. (Note that the subscript “c” in  $K_{pc}$  stands for “communication noise” and the subscript “r” in  $K_{pr}$  stands for “retrieval noise.” These rather confusing designations are used for historical reasons. Care should be taken to not associate them with “calibration” and “random,” respectively.)  $K_{pc}$  is given by:

$$K_{pc} = \frac{1}{\sqrt{N}} \left( 1 + \frac{2}{SNR} + \frac{1}{SNR^2} \right)^{1/2},$$

where  $N$  is the equivalent radar looks associated with the measurement and  $SNR$  is the signal-to-noise ratio defined by

$$SNR = \frac{P_t G^2 A_c \lambda^2 \tau \sigma_0}{(4\pi)^3 R^4 L N_0},$$

where  $P_t$  is the transmit power,  $G$  is the antenna gain in the direction of the measurement cell,  $A_c$  is the area of the measurement cell,  $\lambda$  is the wavelength,  $\tau$  is the integration time,  $R$  is the slant range to the resolution cell,  $L$  is the system loss, and  $N_0$  is the equivalent system noise power spectral density.

### 2.3 Spaceborne Scatterometer Model Functions

In order to assess the measurement sensitivity as a function of frequency and incidence angle, the exact quantitative relationship between the wind vector and  $\sigma_0$  must be considered. The most reliable model functions are those formulated using the largest data sets collected over the widest possible sets of conditions. In general, these are the model functions derived from spaceborne scatterometer missions which have occurred over the past decade. In particular, the model functions derived from “fan-beam” scatterometer missions, which cover a large range of incidence angles, are most appropriate for the present analysis. These fan-beam missions include the NASA Scatterometer (NSCAT) mission at Ku-Band, and the AMI scatterometer on the ERS-1 and ERS-2 platforms at C-Band.

NSCAT made measurements at Ku-Band between incidence angles of 17°-61° for VV polarization, and between 17°-52° for HH polarization. The model function derived from these measurements should therefore only be considered truly valid in these ranges. Good wind performance was observed using measurements over this entire range (see Tsai, et al. 2000). The Seasat-A Scatterometer System (SASS) made HH and VV measurements out to 67°, but the amount of ground truth verification for these measurements is sparse. The SeaWinds scatterometer instrument on the QuikSCAT spacecraft has collected an extensive amount of data, but only at the discrete incidence

angles of 47° for HH polarization and 55° for VV polarization, and consequently form an incomplete data set for incidence angle trade-off studies.

At C-Band the AMI scatterometer on ERS-1,2 collected VV-pol data from 18°-45° on the center beam, and from 25°-59° on the fore/aft beams. The ASCAT instrument on METOP will also operate at VV-pol, but the incidence angles covered by the middle and fore/aft beams have been moved out to 25°-55° and 34°-65° respectively, in order to broaden the overall swath, and improve the ambiguity removal performance in the interior portion of the swath (Kerkmann and Klaes, 1998).

## 2.4 Model Function Sensitivity vs. Incidence Angle

Because it is beyond the scope of the present analysis to do full-up simulation for every conceivable instrument implementation, we instead derive some simple sensitivity metrics that can be applied to the model function. We then use these metrics to assess the relative sensitivity as a function of frequency and incidence angle.

To first order, the speed sensitivity of the backscatter is given by the  $A_0$  term in the model function. In general, the change in the wind speed,  $\Delta U$ , given an “error” in  $\sigma_0$ ,  $\Delta\sigma_0$ , is given by

$$\Delta U = \frac{dU}{d\sigma_0} \Delta\sigma_0.$$

This, in turn, can be approximated on average as

$$\Delta U = \frac{dU}{dA_0} \Delta\sigma_0.$$

Recall that  $\Delta\sigma_0 = K_p \sigma_0$ . When the  $K_p$  parameter is dominated by calibration accuracy as opposed to radiometric precision (i.e.,  $K_{pr} > K_{pc}$ ), then  $\Delta\sigma_0 \propto \sigma_0$  for all values of  $\sigma_0$  and we have that

$$\Delta U \propto \frac{dU}{dA_0} A_0.$$

Defining the “wind speed sensitivity” as  $1/\Delta U$  (i.e., the higher  $1/\Delta U$ , the more sensitive the model backscatter to changes in wind speed), we then obtain a convenient metric for evaluating the sensitivity of the measurement versus incidence angle. We can similarly define a “upwind/downwind discrimination sensitivity” metric  $A_1/A_0$ , and an “upwind cross-wind sensitivity” metric  $A_2/A_0$ . These metrics are plotted for Ku-Band VV polarization (blue), Ku-Band HH polarization (light blue), and C-Band (red) for wind speeds of 3, 5, 10, 15, 20, and 25 m/s in Figures 2-3 to 2-8.

The above metrics were derived assuming that calibration error dominates. In cases where the radiometric precision dominates (i.e.,  $K_{pr} > K_{pc}$ ), then, when SNR is high,  $K_p$  is approximately equal to the square root of the number of radar looks ( $K_p \approx 1/\sqrt{N}$ ). When the backscatter is high, we can generally take proportionately more looks for a given transmit power, so consequently  $N \propto A_0$ . Using the same methodology as described above, we obtain the following alternate expression for  $\Delta U$ :

$$\Delta U \propto \frac{dU}{dA_0} \sqrt{A_0}$$

The wind direction sensitivity metrics can similarly be alternately defined as  $A_1 / \sqrt{A_0}$  and  $A_2 / \sqrt{A_0}$ . Because the backscatter cross-section generally decrease as a function on incidence angle, these alternate metrics take into account the additional number of looks that can be taken at lower incidence angles.

## 2.5 Transmit Frequency Trade-Offs

From the standpoint of the *measurement approach*, the two primary considerations in selecting the transmit frequency are the NRCS sensitivity to the wind vector and the sensitivity of the overall measurement to contamination from rain. These are addressed in turn below. Obviously, the transmit frequency has *implementation* consequences as well – such as the required dimensions of the antenna. The implementation trade-offs of a given frequency are addressed in Section 3.

### 2.5.1 Wind Sensitivity to Frequency

The dominant scattering mechanism that is sensitive to the wind vector over the ocean is Bragg scattering, which follows a power-law spectrum. As the wind blows over the ocean, centimeter scale capillary waves are formed, and are at equilibrium with the local wind field. Naturally, different transmit frequencies are sensitive to different frequency components of the Bragg wave spectrum, so variations in performance are expected at different frequencies. Although these differences can be qualitatively understood from theoretical analysis, an empirical analysis based on available measured data is necessary to conclusively identify the advantages/disadvantages associated with operating at a given frequency.

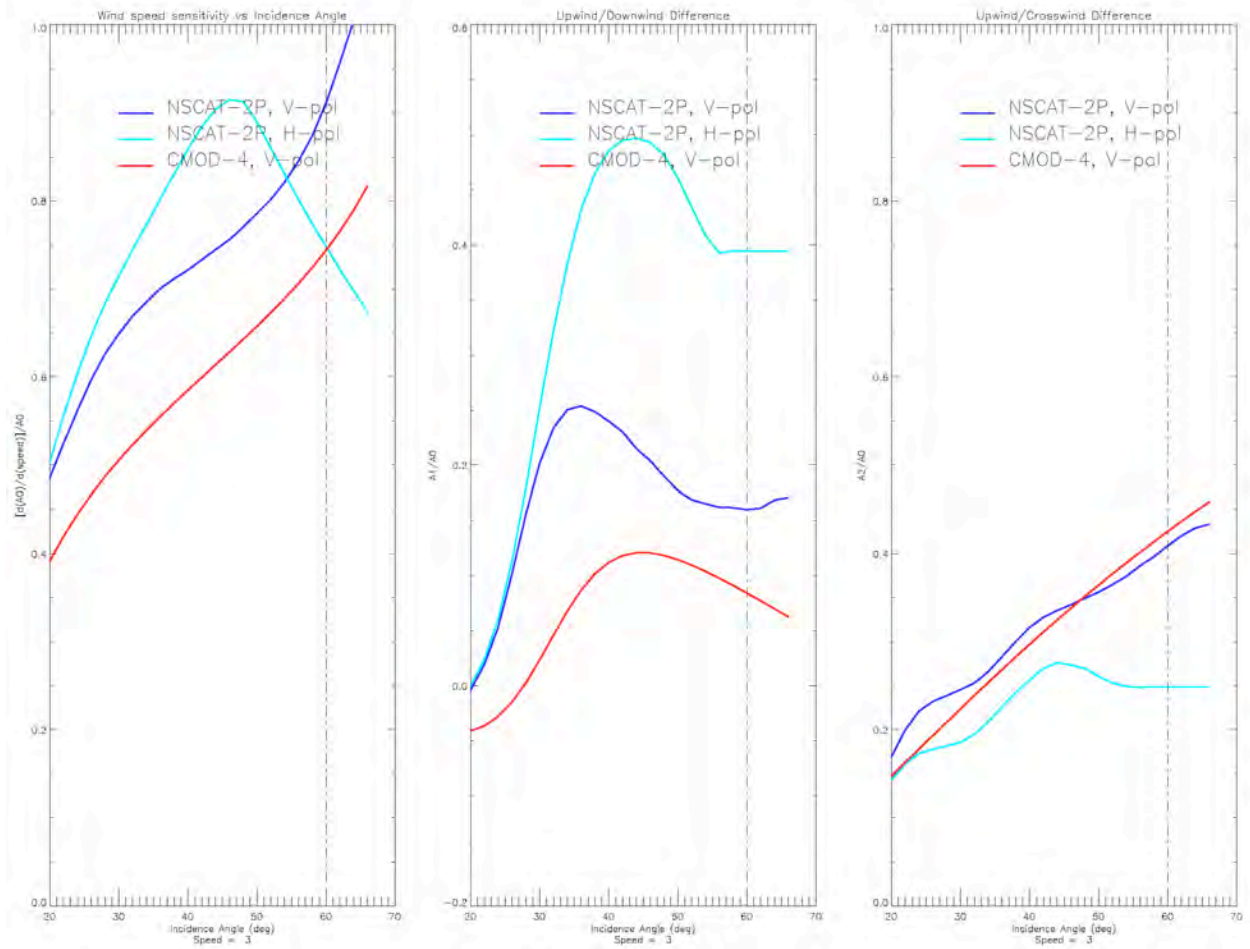


**Figure 2-3: Wind speed, upwind downwind, and upwind/crosswind sensitivity plotted for Ku-Band V-Pol, Ku-Band H-Pol and C-Band H-Pol as a function of incidence angle for a wind speed of 3 m/s. The vertical line at 60° indicates the point beyond which the Ku-Band V-Pol model function becomes largely an extrapolation.**

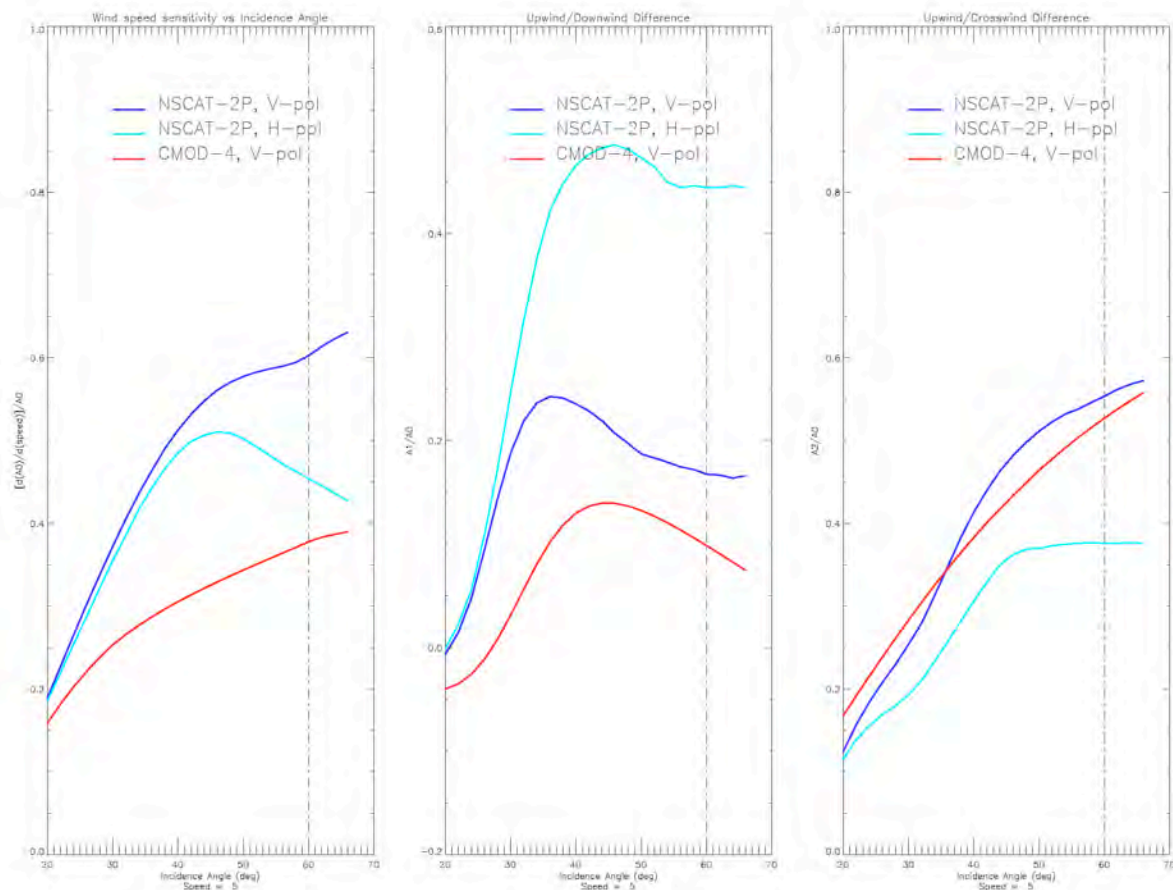


**Figure 2-4: Wind speed, upwind downwind, and upwind/crosswind sensitivity plotted for Ku-Band V-Pol, Ku-Band H-Pol and C-Band H-Pol as a function of incidence angle for a wind speed of 5 m/s. The vertical line at 60° indicates the point beyond which the Ku-Band V-Pol model function becomes largely an extrapolation.**

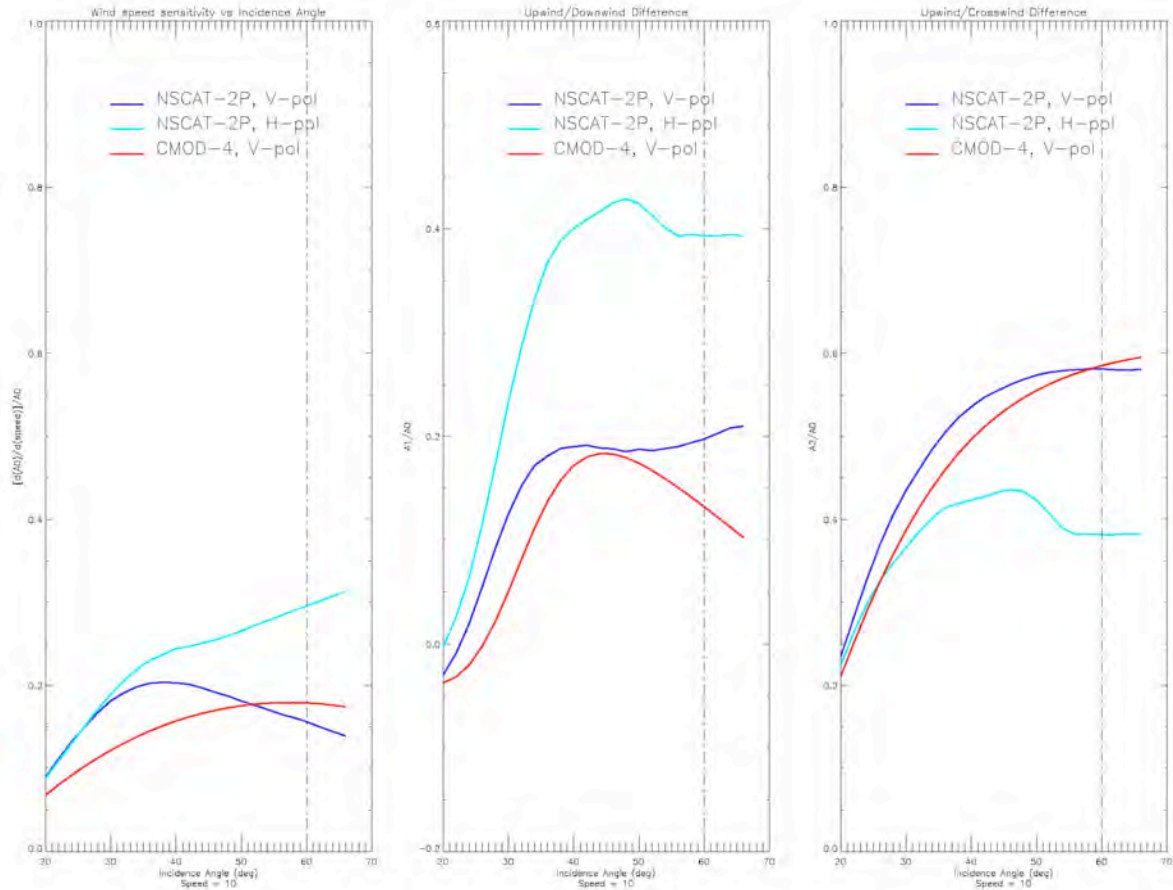


**Figure 2-5: Wind speed, upwind downwind, and upwind/crosswind sensitivity plotted for Ku-Band V-Pol, Ku-Band H-Pol and C-Band H-Pol as a function of incidence angle for a wind speed of 10 m/s. The vertical line at 60° indicates the point beyond which the Ku-Band V-Pol model function becomes largely an extrapolation.**

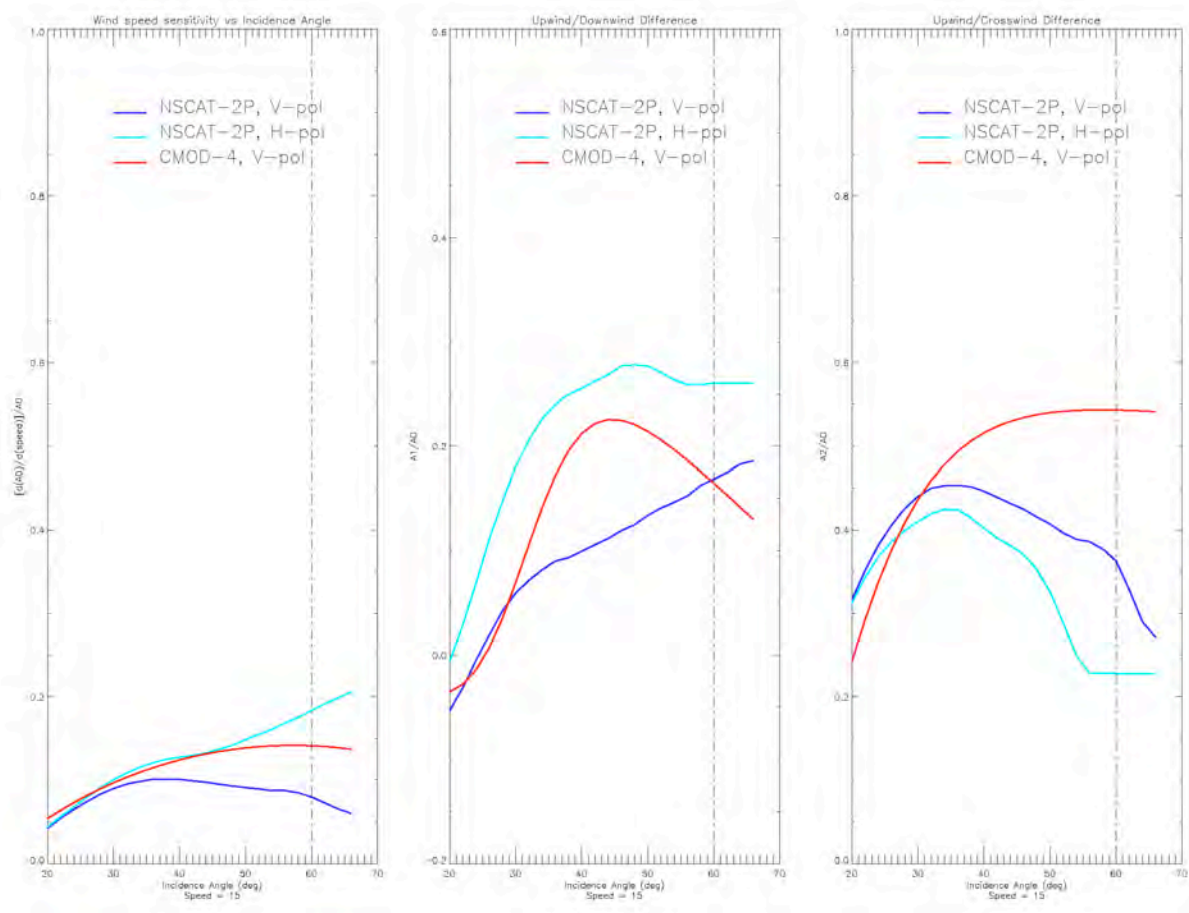


**Figure 2-6: Wind speed, upwind downwind, and upwind/crosswind sensitivity plotted for Ku-Band V-Pol, Ku-Band H-Pol and C-Band H-Pol as a function of incidence angle for a wind speed of 15 m/s. The vertical line at 60° indicates the point beyond which the Ku-Band V-Pol model function becomes largely an extrapolation.**



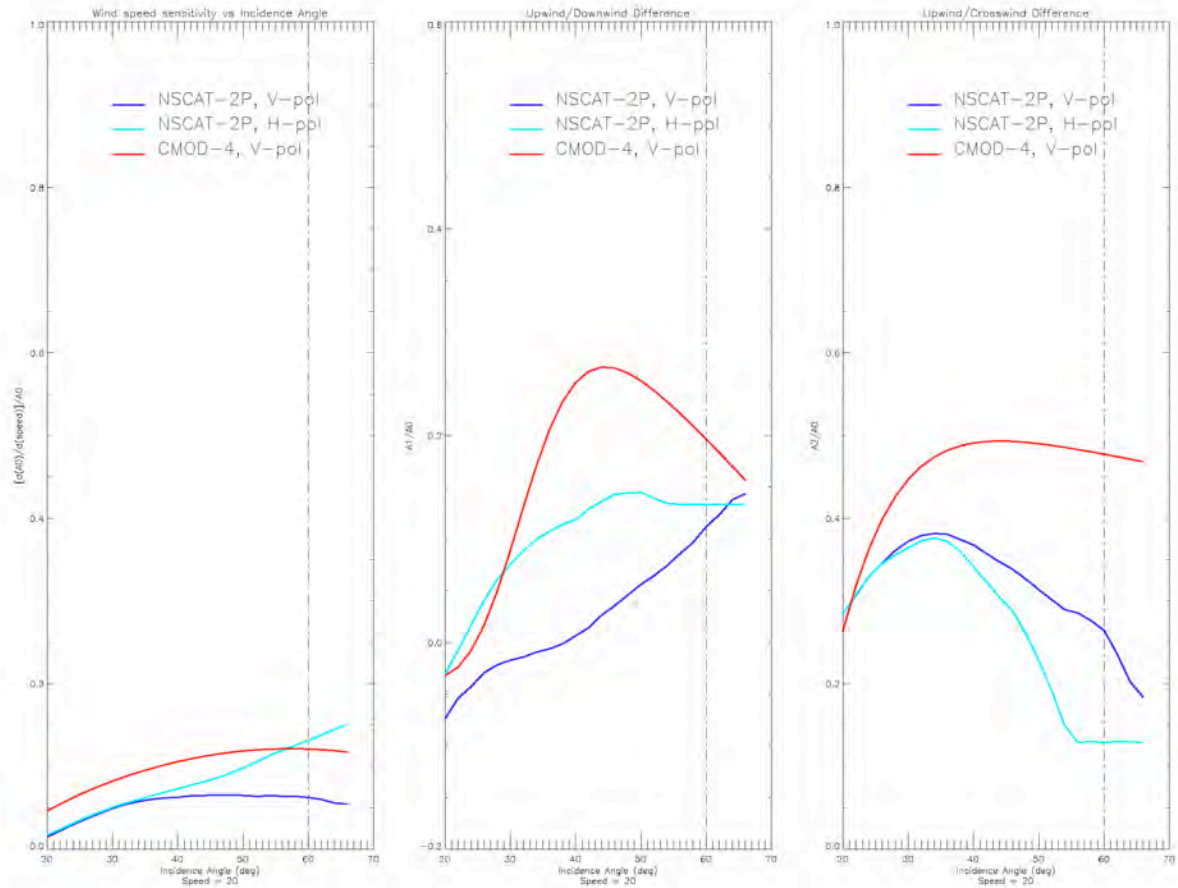


**Figure 2-7: Wind speed, upwind downwind, and upwind/crosswind sensitivity plotted for Ku-Band V-Pol, Ku-Band H-Pol and C-Band H-Pol as a function of incidence angle for a wind speed of 20 m/s. The vertical line at 60° indicates the point beyond which the Ku-Band V-Pol model function becomes largely an extrapolation.**

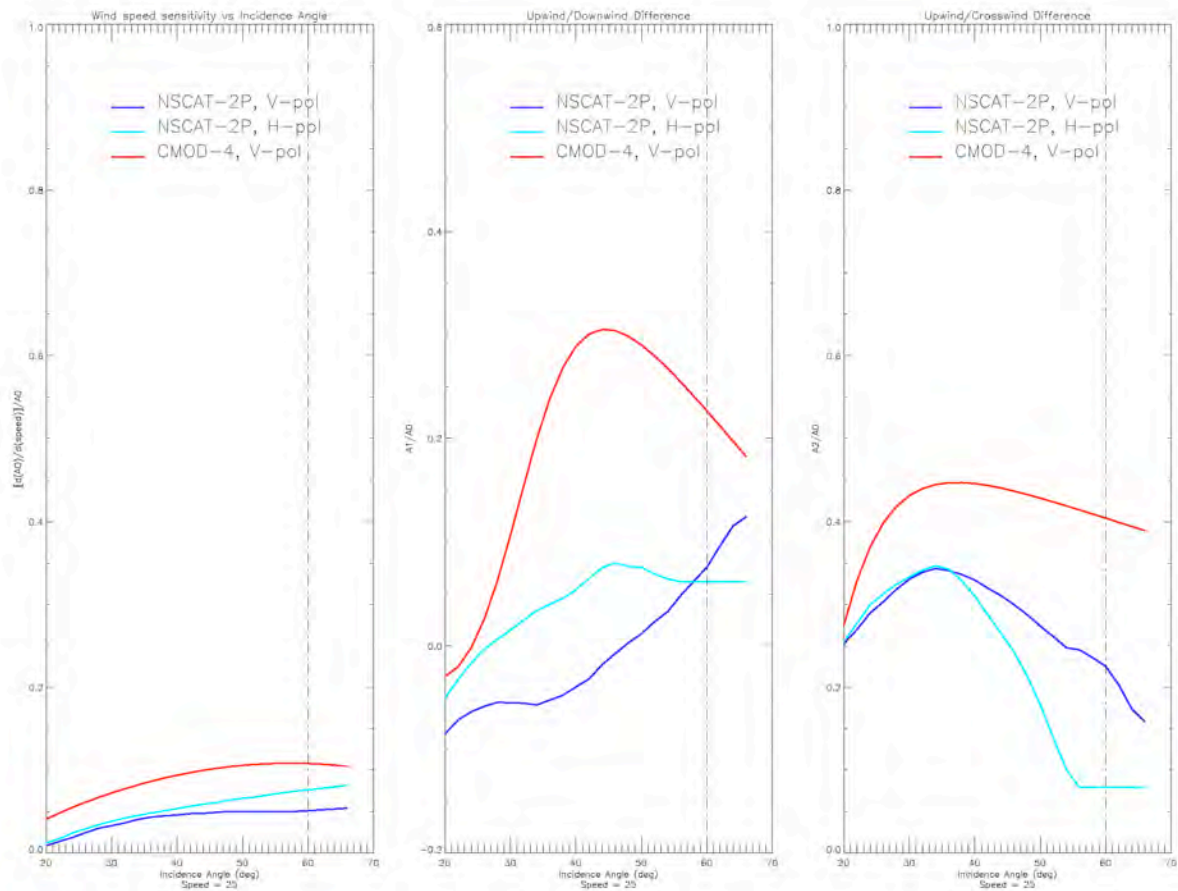


**Figure 2-8: Wind speed, upwind downwind, and upwind/crosswind sensitivity plotted for Ku-Band V-Pol, Ku-Band H-Pol and C-Band H-Pol as a function of incidence angle for a wind speed of 25 m/s. The vertical line at 60° indicates the point beyond which the Ku-Band V-Pol model function becomes largely an extrapolation.**

A direct comparison between the two frequencies actually employed by current and previous spaceborne scatterometers—Ku-Band (14 GHz) and C-Band (5.3 GHz)—is readily available by an examination of the model function sensitivity curves in the preceding Figures 2-3 to 2-8. At the relatively low wind speeds of 3 and 5 m/s, the performance of Ku-Band is superior both in terms of wind speed sensitivity and upwind/downwind sensitivity. This is a well-known deficiency at C-Band, and it is acknowledged that ERS-1,2 and ASCAT only can meet wind accuracy requirements for wind speeds above 4 m/s (see Table 1-1).

At the moderate wind speeds of 10 and 15 m/s, the performance of C-Band and Ku-Band seems comparable, the only significant exception being the significantly higher upwind/downwind sensitivity of the Ku-Band HH polarization. For the model functions plotted, the sensitivity of C-Band appears superior to that of Ku-Band for all metrics at the high winds of 20 and 25 m/s. Care must be taken, however, in interpreting these

results. In (Donnelly et al. 1999) it was demonstrated that currently used C-Band model functions may be substantially in error for high wind speeds. The sensitivity to high winds at C-Band in particular is observed to be somewhat less than what the CMOD4 model function predicts. This is due to a saturation effect, which begins to be significant at wind speeds above about 15 m/s for both Ku-Band and C-Band measurements. Despite this saturation effect, some sensitivity to both wind speed and wind direction persists for very high wind speeds up in the 35-50 m/s range (see Donnelly et al., 1999, Yueh et al. 2001, and Quilfen, et al. 1998). Although the curves presented in (Donnelly et al. 1999) actually suggest that there may be a slight advantage to Ku-Band in high-wind (and rain-free) conditions, the paucity of the data constrains us to conclude that Ku-Band and C-Band wind sensitivity are comparable in this regime.

Although not employed by operational spaceborne scatterometers, the wind sensitivity at other frequencies (besides Ku-Band and C-Band) have been examined. Aircraft experiments described by (Masuko et al. 1986) demonstrated wind sensitivity at both X-band and Ka-Band. Over the low to moderate wind speed regime examined, the results of this study indicated comparable sensitivity to that of C-Band and Ku-Band. Using a larger data set collected using the JERS-1 SAR, an L-Band wind model function was constructed by Shimada et al. At this low frequency, however, it was observed that no significant directional information can be obtained for wind speeds below about 8 m/s.

## 2.5.2 Rain Sensitivity

Another factor that may influence the selection of the scatterometer operating frequency is the sensitivity to rain contamination. In general, the modification of the backscatter measurement due to rain can be expressed as:

$$\sigma_m = \alpha(\sigma_0 + \sigma_{se}) + \sigma_r,$$

where  $\sigma_m$  is the measured value of the backscatter cross-section by the radar,  $\sigma_0$  is the backscatter cross-section that would have existed in the presence of wind only,  $\sigma_{se}$  is the enhancement (or reduction) in the backscatter cross-section due to rain drops impacting the surface,  $\alpha$  is the attenuation of the signal from the surface due to rain in the atmosphere, and  $\sigma_r$  is the rain equivalent cross-section due to radar scattering from the airborne drops (i.e., the apparent backscatter cross-section that would exist if the backscatter were coming only from the rain).

The atmospheric effects associated with  $\alpha$  and  $\sigma_r$  are relatively straightforward to quantify. We can utilize any one of several parameterizations in common use by researchers investigating the impact of rain on microwave signals (see Spencer and Shimada, 1991). These formulae are derived from measurements and Mie scattering theory and, though large variations are observed in nature, represent reasonable average parameterizations for a given rain rate. They also allow a relatively straightforward comparison of the effects of atmospheric rain at different frequencies.

For a uniform rain layer of depth  $d$  km, and horizontal extent  $> d$ , the value of  $\alpha$  can be approximated by:

$$\alpha = 10^{-0.2\kappa d / \cos\theta},$$

where  $\theta$  is the incidence angle of the measurement and  $\kappa$  is the rain attenuation coefficient in dB/km. The coefficient  $\kappa$  can generally be parameterized as

$$\kappa = \kappa_1 r^b,$$

where  $r$  is the rain rate. From measurements, reasonable values for  $\kappa_1$  and  $b$  are given by:  $\kappa_1 = 0.22\lambda^{-2.8}$ , and  $b = 1.17$ . Note the strong dependence on transmit frequency for  $\kappa_1$ .

The volume backscatter coefficient of rain,  $\sigma_{vr}$ , is well approximated by:

$$\sigma_{vr} = 5.5 \times 10^{-6} r^{1.6} \lambda^{-4}.$$

Again, note the strong dependence on  $\lambda$ . Assuming a uniform rain layer of depth  $d$  and relatively large horizontal extent (as above for the attenuation calculation), and taking into account the attenuation between each element within the rain layer and the sensor, the volume backscatter can be integrated to yield rain equivalent backscatter cross section (see Spencer and Shimada, 1991):

$$\sigma_r = \sigma_{vr} \frac{1 - \alpha}{0.2\kappa \ln 10}.$$

Utilizing the above equations, the impact of airborne rain on the scatterometer backscatter measurement can be estimated as a function of frequency. The result of such a calculation is shown in Figure 2-9. Here, the error due to the presence of atmospheric rain between the measured backscatter and the actual surface backscatter, defined as the ratio  $\sigma_m/\sigma_0$ , is plotted as a function of the surface backscatter cross section for several different transmit frequencies. The value of  $\sigma_m$  was calculated using the above formulae and assuming a rain layer depth of 4 km, and a constant moderate rain rate of 10 mm/hr. The shape of the curves is due to relative strength of the backscatter from the surface and from the rain. For large values of surface  $\sigma_0$ , the return from the surface dominates the backscatter from the rain, and consequently the measured  $\sigma_m$  is essentially an attenuated value of the surface  $\sigma_0$ . For small values of surface  $\sigma_0$ , however, the backscatter from the rain is dominant, and consequently appears to increase the value of the cross-section in the measurement. Note that, qualitatively, these effects are common at all frequencies, but the magnitude of the influence of rain increases dramatically at higher frequencies. For the 10 mm/hr rain rate assumed, the modification of a C-Band measurement due to rain would be less than 1 dB for a surface cross-section of  $-20$  dB. At Ku-Band, the same conditions would produce a 6 dB change in the measured cross-section. This is

obviously due to the strong wavelength dependence – on the order of  $\lambda^3$  and  $\lambda^4$ , respectively – for the attenuation and volume backscatter associated with rain.

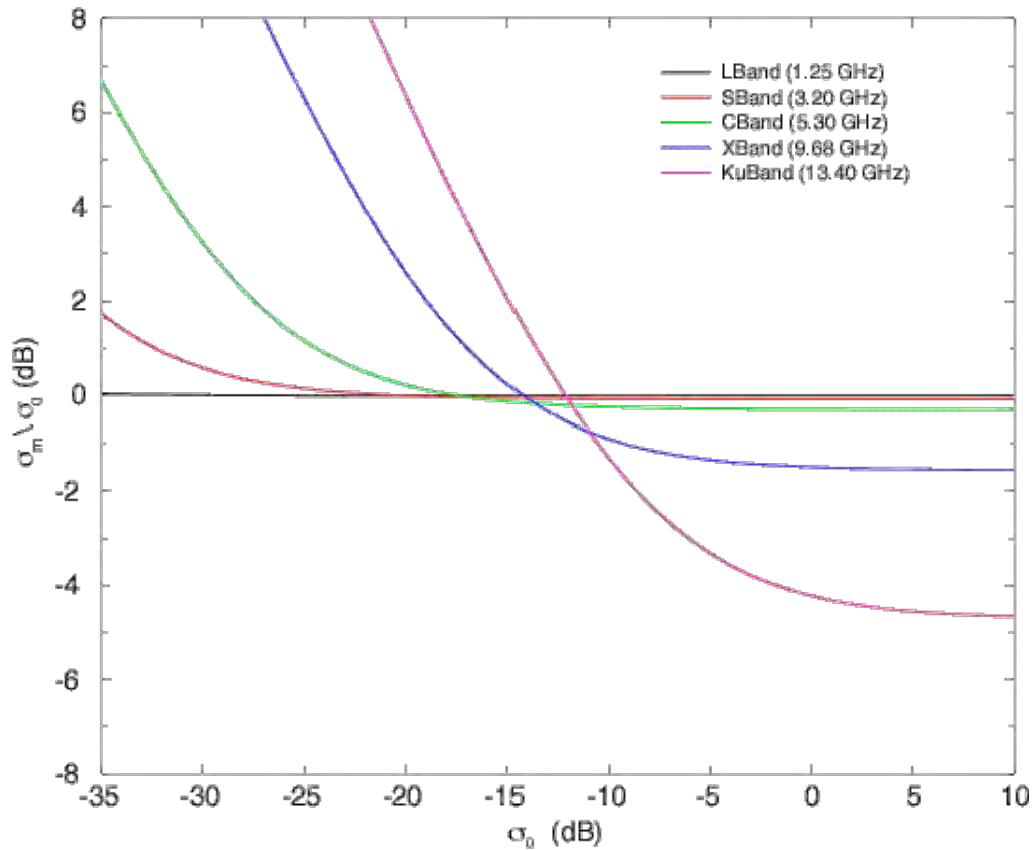


**Figure 2-9: Error between measured surface cross-section and actual surface cross-section due to the presence of rain, plotted as a function of surface cross-section, for different transmit frequencies. In generating these curves, a uniform rain layer with a rain rate of 10 mm/hr and a depth of 4 km is assumed.**

It is important to note that Figure 2-9 only shows the relative sensitivity when rain is present. Studies have indicated that only 5% of the ocean has rainfall rates greater than 2 mm hr<sup>-1</sup> km<sup>-2</sup>. Further, even when rain is present and significantly impacts the scatterometer measurement (as may be the case with Ku-Band measurements), the backscatter measurements may be corrected to yield reasonably accurate retrievals. In (Yueh, et al. 2001), Ku-Band measurements from SeaWinds/QuikSCAT were successfully corrected for the presence of rain using rain rates derived from collocated SSM/I radiometer measurements. In (Draper and Long, 1999), an algorithm was developed capable of retrieving the rain and wind simultaneously, when no separate measurement of rain rate was available.

The actual modification of the wind roughened surface due to the impact of rain, given by the parameter  $\sigma_{se}$ , is due to splash “stalks” formed by the raindrop impacts and centimeter scale “ring waves” radiating out from the point of impact. Both experimental and

theoretical analysis of these phenomena indicate that the rain impacts tend to *increase* the value of the surface NRCS. Analyses by (Craeye et al. 1997) at Ku-Band show an enhancement of several dB, with the increase larger for higher rain rates and/or lower wind speeds. A comparison of the expected effects due to atmospheric rain from Figure 2-9 and those due to rain impacts from (Craeye et al. 1997) tend to suggest that the greater corruption of the scatterometer measurements is likely due to the atmospheric components.

Anecdotal evidence to support the assertion that atmospheric rain has a larger effect than surface modification due to rain is provided by (Grassotti et al. 1998), where a raining region contemporaneously observed by ERS-2 and NSCAT was examined. In this study, a suspected tropical rain cell was identified in GOES infrared data (GOES can flag convective rain cells with some fidelity when the clouds tops appear excessively cold in the infrared). Given the meteorological conditions, relatively constant easterly winds were expected. Indeed, outside the raining region, both NSCAT and ERS-2 agreed on an easterly flow of 15 to 25 knots. Within the raining region, however, whereas the C-Band measurements were consistent with the surrounding wind field, the Ku-Band measurements were significantly larger (up to 30 to 40 knots), with wind directions indicating a southerly flow. As expected from Figure 2-9, clear evidence of atmospheric impact was observed at Ku-Band, but no discernable effect of surface modification was observed at C-Band.

### **2.5.3 Transmit Frequency Guidelines For Trade-Off Studies**

From the perspective of measurement sensitivity and accuracy, we conclude that use of frequencies between 5 and 14 GHz (i.e., C-Band to Ku-Band) can be successfully used by an operational spaceborne scatterometer, and will be considered in the OVWM implementation trade-offs. Operating at the higher end of this band yields more sensitivity at low to moderate wind speeds (and, as will be shown in Section 3, has some significant implementation advantages as well), but at a cost of greater sensitivity to rain. If a higher frequency is selected, provisions to either flag or, preferably, to correct for, raining areas must be included as part of the scatterometer design. (The requirements on a radiometer channel to be included as part of the scatterometer instrument in order to detect and correct for rain are discussed later in this section.) Frequencies lower than 5 GHz have too little wind sensitivity, and frequencies higher than 14 GHz are too susceptible to atmospheric effects, and shall not be considered in the trade-off study.

## **2.6 Incidence Angle Range**

The determination of an allowable range of incidence angles for the scatterometer measurement is a critical parameter to determine both the extent of the swath and the wind performance. In general, the wider the range of allowable incidence angles, the broader the swath coverage, and the better the revisit statistics. The limits of the

incidence angle range are determined by the regime where the model function is sufficiently sensitive to yield good wind performance. At incidence angles below about 20°, the model function becomes insensitive to wind speed. At incidence angles above about 60°, the magnitude of  $\sigma_0$  falls off precipitously, and it is difficult to maintain adequate SNR. For these reasons, most spaceborne scatterometer systems have operated in the 20°- 60° incidence angle regime.

Examining Figures 2-3 to 2-8, we make the following general observations:

1. For both frequencies (Ku-Band and C-Band), and at all wind speeds, there is a dramatic decrease in sensitivity below an incidence angle of 20°.
2. In the high incidence angle regime (> 50°) the situation is more mixed. Some metrics are better for higher incidence angles at some wind speeds but not at others. In general, the sensitivity metrics are observed to vary relatively slowly in this regime.
3. One prominent exception to conclusion #2 above is the upwind/downwind sensitivity metric ( $A_l/A_0$ ) for Ku-Band HH polarization. This metric consistently peaks at around 50° at all wind speeds. Similarly, the same metric for C-Band VV pol consistently peaks around 45° at all wind speeds.

Taking these observations into account, and considering the fact that the model function is most reliable for the range of data actually collected (as opposed to the regions where the model function has been extrapolated) we adopt the following guidelines for performing trade-offs in the scatterometer instrument design:

1. The minimum incidence angle employed should not be less than 20°.
2. A nominal maximum incidence angle of 60° shall be assumed for swath width calculations in the orbit/revisit analysis.
3. For system concepts that utilize a wide range of different incidence angles (such as fan-beam concepts similar in architecture to NSCAT and ASCAT), a more aggressive maximum value of 65° may be assumed. The wider range is allowed because only a small percentage of the measurements will be made at these higher incidence angles.
4. For system concepts that utilize discrete incidence angles (such as conically scanning pencil-beam concepts similar to SeaWinds), a more conservative maximum incidence angle of 55° shall also be evaluated in calculating the swath and revisit time. This will ensure that, if future analyses show that collecting *all* the data at 60° is too aggressive, sufficient data exists to evaluate the more conservative option as well.

## 2.7 Polarimetric Radar Channels

To this point, we have discussed *co-polarized* scatterometer measurements made at either vertical or horizontal polarizations (i.e., either VV or HH polarized measurements). In remote sensing applications, the *cross-polarized* return often contains additional information about the surface. Of particular interest in wind scatterometry is the mathematical correlation of the co-polarized and cross-polarized return (typically denoted by  $\sigma_{hvvh}$  or  $\sigma_{vhvh}$  and here referred to simply as a *polarimetric* measurement). In this section, the potential for polarimetric radar measurements to improve the scatterometer design is summarized.

### 2.7.1 Polarimetric Radar Theory

In addition to the extra information provided by using multiple polarizations, there is also value in the measurement of the cross-polarized signal as well. Theoretical studies have demonstrated that whereas the azimuthal modulation of both the pure co-polarized and pure cross-polarized returns from the ocean surface are even functions of azimuth, the correlation between the co- and cross-polarized signals is an odd function of azimuth. In Figure 2-10a, values of the co-polarized and cross-polarized model functions for a sample ocean wind case are plotted. Note that the cross-polarized return is significantly lower than the co-polarized return. Because the cross-polarized return has essentially the same modulation as the co-polarized case, no additional information exists to benefit the wind retrieval. In Figure 2-10b, a theoretically derived function for the co/cross correlation term has been generated using the techniques described in (W-Y. Tsai et al. 2000). Note that, here, the function looks significantly different. In addition to the odd symmetry, the function has no wind-speed dependent bias (i.e., it is zero mean). The shape of this function holds out the possibility that additional information exists to further constrain the wind solution. Indeed, aircraft measurements reported by (Yueh et al. 2002, discussed below) have validated that this polarimetric phenomenology exists, although the magnitude of the effect is somewhat less than that shown in Figure 2-10b.



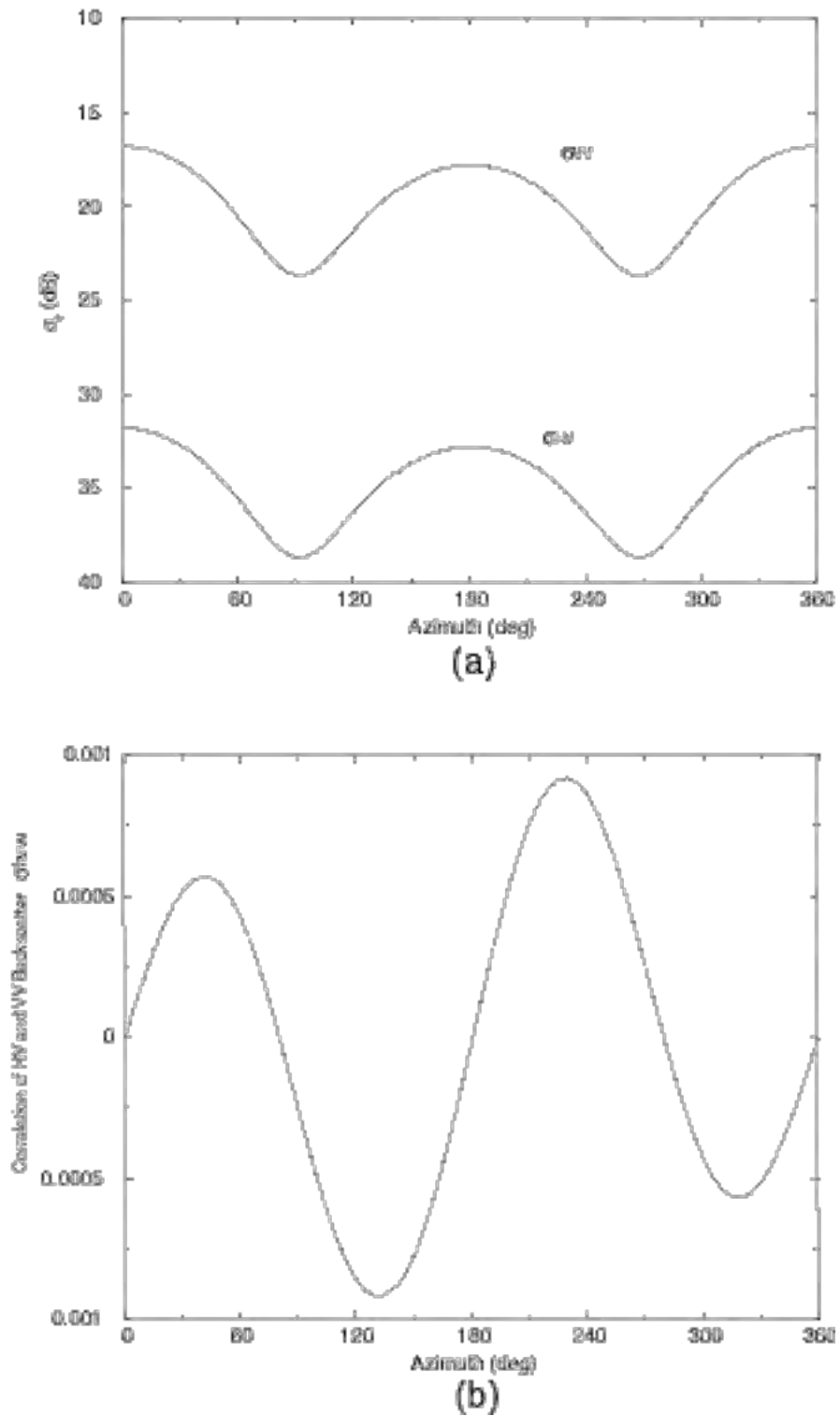
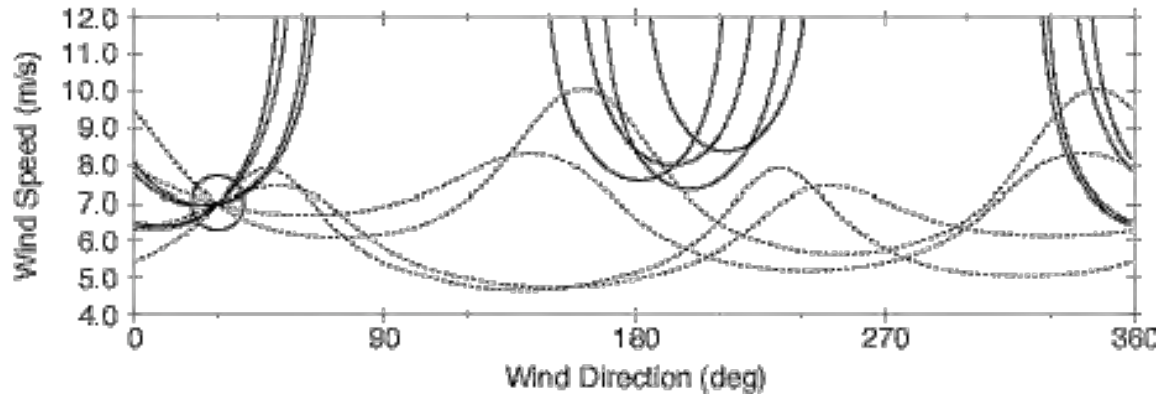


Figure 2-10: a) Ku-Band co-polarized and cross-polarized backscatter vs. relative wind azimuth for 8 m/s wind. b) Theoretical result for co/cross correlation polarimetric term for 8 m/s wind.

To see the potential for polarimetric measurements to improve the wind retrieval, consider Figure 2-11. Here, the dotted curves represent the solutions derived from the co-polarized measurements of a 7 m/s wind blowing at an azimuth of  $30^\circ$  (identical to the solutions shown in Figure 2-2b). The solid lines represent the solutions that would be derived from a set of polarimetric measurements made at the same time and with the same geometry. Note that, whereas in the co-polarization-only case, there were multiple wind direction ambiguities present, when the polarimetric data is included, the true solution (indicated by the intersection of all of the curves) stands out much more prominently.



**Figure 2-11: Wind vector solutions plot for 7 m/s wind blowing at relative azimuth of  $30^\circ$ . Dotted lines are co-polarized solutions for measurements (as also shown in Figure 2-2). Solid lines are solutions for theoretical polarimetric measurement made for the same geometry. The “true” solution is indicated by the circle.**

Polarimetric wind retrieval simulations have been performed at JPL for the conically scanning pencil-beam (i.e., SeaWinds-like) scatterometer case. These simulations were performed using a theoretical polarimetric model function, adjusted somewhat to agree with the limited aircraft results reported by (Yueh et al. 2002). A summary of conclusions from these studies was provided by W-Y. Tsai at the Ocean Vector Winds Science Team Meeting in Oxnard, CA, on January 16, 2003. These conclusions are as follows:

1. When polarimetric radar measurements are added to the co-polarized measurements collected with a SeaWinds-like sensor, there is a significant potential for improvement of wind retrieval accuracy. In particular, ambiguity selection can be successfully performed without resorting to “nudging” (imposing constraints from external numerical weather model results). Furthermore, wind retrieval performance in the nadir and outer-swath regions where the azimuth diversity of a conically scanning system is weak (see Section 3) is significantly improved. Both of these results are due to the fact that the polarimetric measurements are providing the equivalent of an another orthogonal azimuth “look” for each measurement.

2. When a polarimetric channel is employed on a conically scanning system, there is significant potential for operating with only one beam (as opposed to the two beams that SeaWinds uses to obtain the required number of co-polarized azimuth looks). Again, this is because the polarimetric measurements are providing the equivalent of an another orthogonal azimuth “look” for each measurement. Operating with one beam would significantly simplify the antenna design. (Note, however, that this one beam system must scan over the entire  $360^\circ$  azimuth range just like SeaWinds).
3. When polarimetric channels are added to a two-beam system, it is possible to obtain similar performance to SeaWinds by just operating over  $180^\circ$  of the antenna scan. This may dramatically ease spacecraft accommodation when obtaining an entire  $360^\circ$  field-of-view is difficult.

Although these simulation results were performed for a conically scanning, pencil-beam antenna architecture, the conclusions are applicable to other architectures (such as fan-beam) systems as well. For these other architectures, the addition of polarimetric channels may improve wind retrieval performance or allow a simplification of the antenna design.

## **2.7.2 Polarimetric Radar Measurements**

Although the theoretical results discussed above are quite promising, actual measurements of the polarimetric signature are necessary to fully demonstrate this capability. To date, only one aircraft measurement campaign has been performed with the focused objective of measuring the polarimetric radar signature of ocean winds. The results from this campaign are described in (Yueh et al. 2002). Measurements at Ku-Band were made on two days during August 2002 over the Pacific Ocean off of Monterey, California. The overall conclusions of the study were extremely positive, with the theoretically predicted polarimetric signature qualitatively verified. The magnitude and phase of the modulation signature, however, was somewhat different than what the theory had predicted. Furthermore, because only two days of data were collected, the data set is extremely limited. Currently data is only available between 9 and 11 m/s and at an incidence angle of  $45^\circ$ . The study concludes that a more extensive campaign is required in order to obtain a sufficiently complete understanding of the polarimetric model function under a full range of conditions.

In addition to the issue of the model function, it is important to consider some real-world implementation issues associated with polarimetric measurements. Polarimetric measurements generally require a co-pol to cross-pol channel isolation on the order of 30-40 dB. This requirement primarily drives the antenna design, and is achievable, but not trivial. Phase stability and/or knowledge on the order of  $20^\circ$  between the co-pol and cross-pol channels is another design consideration that may add implementation complexity.

### 2.7.3 Polarimetric Radar Channel Conclusions

Based on the above survey of polarimetric theory and measurements, the following is concluded for the purposes of the present OVWM study:

1. Due to the significant potential of polarimetric radar measurements to improve wind performance or lead to less complex instrument implementations, a more extensive airborne polarimetric campaign should be seriously considered.
2. Until additional data is available, we should not adopt a scatterometer design that *relies* on polarimetric channels in order to meet minimum performance requirements (i.e., all minimum performance requirement should be able to be met with the available co-polarized measurements). Examples of scatterometer designs which require polarimetric channels include the “forward half-scan” or “single-beam” conically-scanning architectures described in Section 3.
3. Despite conclusion #1 above, polarimetric channels should be considered as supplementary measurements to purely co-pol systems where possible. Such a capability may make sense, for instance, when the hardware implementation is such that the polarimetric channels could be added relatively easily.

## 2.8 Radiometer Channels

As discussed in Section 2.5.2, when frequencies higher than C-Band (i.e., X-Band and Ku-Band) are used, atmospheric rain has a significant effect on the accuracy of the scatterometer measurement. When such “high” frequencies are employed, some type of rain flagging to alert the user to the potential inaccuracies associated with the data is mandatory. Where possible, it is also highly desirable to correct the measurements for the presence of rain. Passive radiometer measurements, collocated to the backscatter measurements, are a demonstrated way to flag or improve scatterometer wind measurements. In addition, polarimetric radiometer channels, like polarimetric scatterometer channels, may be used to aid and improve the wind retrieval fidelity. In this section the utility of passive radiometer measurements is reviewed. As in other sections, this data is interpreted to construct a set of guidelines for the system trade-off study analysis.

### 2.8.1 Rain Detection and Correction Techniques

The detection of the presence of rain and rain intensity from space has been demonstrated using both visible/infrared and passive/active microwave sensors. Of these data sets, multi-frequency microwave radiometer retrievals of rain have been particularly useful because of their accuracy and wide coverage swath. During the calibration of the SeaWinds instrument, co-located SSM/I rain rate data was used to flag scatterometer data where rain contamination was likely. In Yueh et al. 2001, it was demonstrated that co-

located SSM/I rain rate data could actually be used to correct for the effects of rain in Ku-Band scatterometer data, as opposed to simply flagging contaminated regions. In this analysis, the SSM/I derived rain rate was used together with hurricane wind field models to derive a rain-dependent model function to be used when retrieving winds within tropical cyclones. Using this technique, substantial wind speed retrieval improvement was noted for Hurricane Floyd. The key significance of this study is the demonstration that, under certain conditions, Ku-Band scatterometer data can be corrected for rain contamination when co-located rain rate data is available.

Despite the convenience of utilizing data from existing spaceborne radiometer instruments, this method of rain detection/correction is of limited utility on an operational basis. This is because rain events are rapidly changing phenomena, and collocations with the scatterometer data are not always sufficiently contemporaneous to ensure that the rain has been characterized to the desired accuracy. Even for the Global Precipitation Measurement (GPM) system – which will ultimately utilize multiple platforms carrying microwave radiometers – the revisit time in the tropics will not be better than three hours. Thus it is desirable to use radiometer measurements that are made from the same platform as the scatterometer, and are therefore guaranteed to be contemporaneous.

The QuikSCAT mission provided a unique opportunity to explore different techniques for detecting rain. The SeaWinds scatterometer was the only instrument aboard QuikSCAT, and there were no other sensors designed specifically to provide collocated rain data. Jones et al. 2000 noted, however, that the Ku-Band radar receiver itself could be used to obtain radiometer measurements which were sensitive to the presence of rain. Although these measurements were single frequency and had relatively coarse precision and calibration accuracy versus that typically obtained with radiometer instruments, some success was demonstrated retrieving rain rate (Jones et al. 2002) and correcting for rain within tropical cyclones (Adams et al. 2002) using these measurements. If the Ku-Band receiver electronics are designed with radiometer measurements in mind a priori, both radiometric precision and calibration accuracy can be improved to yield even better sensitivity to rain. A combined radar/radiometer operating at the same frequency is attractive because many of the antenna and electronics components can be shared, leading to significant cost savings. One question to be resolved about this approach is whether or not utilizing a single radiometer frequency will yield a rain detection/correction of sufficient accuracy.

Another technique developed from the QuikSCAT data is the use of the scatterometer backscatter measurements themselves to identify raining regions. In Huddleston and Stiles, it is noted that the backscatter signature from raining regions is different from that of rain-free ocean regions. When rain is present, the wind speed is higher on average, the H-polarized return is larger relative to the V-polarized return, there is an increased tendency for the wind vectors to be aligned orthogonally to the satellite ground track, and the wind retrieval goodness-of-fit as determined by the maximum likelihood is degraded. These metrics, along with the SeaWinds Ku-Band brightness temperatures described by (Jones et al. 2000), were used to develop a conditional probability for the presence of rain using collocated SSM/I data as the truth set. This technique, which is known as

Multidimensional Histogram (MUDH) Rain-Flagging, was adopted as the operational rain-flagging algorithm for the SeaWinds/QuikSCAT mission. When the MUHD rain-flag is tuned to flag 5% of the scatterometer data as rain contaminated (which is the percentage of measurements where integrated rain rates exceeding 2 km mm/hr should be observed according to SSM/I), approximately 70% of all raining regions are correctly detected and flagged as “rain.” Care should be taken in interpreting this result, however, because many of the missed detections are for cases where integrated rain rates greater than 2 km mm/hr exist, but do not significantly effect the measurement because the wind speed is relative high (see Figure 2-9).

The idea that scatterometer data itself can be used to correct for rain has also been demonstrated by (Draper and Long, 1999). In their technique, the unique scatterometer signature associated with the presence of rain is utilized to develop an inversion technique that retrieves both the rain rate and the surface wind velocity. The wind retrievals obtained by this approach are shown to be significantly better than wind retrievals where no attempt is made to correct for rain. This study represents another strong indication that information contained in radar backscatter can also be used to detect/correct the effects of rain.

SeaWinds on ADEOS-II will have the benefit of flying with the AMSR multi-frequency microwave radiometer. AMSR’s many frequencies and polarizations, high precision and calibration accuracy, as well as high spatial resolution will enable high fidelity retrievals of rain rate that can be used for flagging and correcting the SeaWinds data.

Although the previous studies described above for QuikSCAT have demonstrated the potential for rain detection and correction, they have primarily been geared towards addressing the question: “What can we do with what we have?” For the next generation OVWM scatterometer system, we are much more interested in understanding the answer to “What is the most cost-effective suite of measurements to get adequate rain detection/correction performance?” Although this optimum measurement suite will almost certainly consist of radiometer channels, the question of which frequencies and polarizations are necessary remains unanswered. The results of (Huddleston and Stiles, 2000) and (Draper and Long, 2003) suggest that information derived from the scatterometer data itself, when combined with collocated radiometer data, may possibly reduce the need for all but one or two radiometer frequencies in performing rain detection/correction. The existence of the AMSR data, collocated and contemporaneous with SeaWinds backscatter measurements, represents an excellent opportunity to study rain detection/correction fidelity as a function of the frequency and accuracy of radiometer channels.

## **2.8.2 Polarimetric Radiometer Channels**

Like active scatterometer measurements, passive radiometer measurements are also sensitive to wind speed and direction. In an analogous fashion to backscatter cross-section, the vertically and horizontally polarized brightness temperatures are even

functions of wind direction (see Yueh et al. 1998). Further, the third and fourth Stokes parameters of ocean emission,  $U$  and  $V$  respectively, are odd functions of wind direction similar to the polarimetric backscatter measurements that are described in Section 2.7. Obtaining the third and/or fourth Stokes parameter therefore has significant potential for improving the wind retrieval performance, similar to that which was described for the polarimetric radar case.

Unlike the polarimetric radar measurements, however, significantly more aircraft based measurements have confirmed the nature of this phenomenon for a variety of different sea surface and atmospheric conditions. Passive polarimetric measurements of the sea surface have been obtained at 10, 19, and 37 GHz, all indicating a clear sinusoidal modulation associated with the third (and fourth) Stokes parameters. Further, as reported by (West and Yueh, 1996), observations under cloudy conditions have shown that the odd modulation associated with the third (and, by inference, fourth) Stokes measurements are readily evident under cloudy conditions as well. With the launch of WindSat in 2003, the utility and characteristics of these measurements is being further confirmed from space.

Unlike the multifrequency radiometer wind retrievals envisioned for WindSat (and, ultimately, CMIS), the supplemental use of a polarimetric radiometer channel with a scatterometer is likely to only require one frequency. All that is required is that a modulation signal orthogonal to the co-polarized backscatter signature be obtained. This by itself could lead to a dramatic improvement in wind retrievals where the azimuth diversity is non-optimal (as in the case of the nadir and outer-swath regions of conically scanning scatterometers such as SeaWinds). Naturally, efforts must be made in the design process to ensure that the polarimetric measurements can be made with sufficient accuracy. In particular, cross-polarization levels approaching  $-30$  dB are desired.

### **2.8.3 Radiometer Channel Conclusions**

Based on the above survey of the utility of radiometer channels, the following is concluded for the purposes of the present OVWM study:

1. For scatterometer concepts that employ relatively high radar frequencies (i.e.,  $> 6$  GHz), collocated passive radiometer measurements shall also be collected in order to, at minimum, flag measurements contaminated by rain. The ability to correct for the effects of rain contamination is highly desirable.
2. A study should be conducted in order to determine the optimal combination of backscatter/radiometer measurements in order to detect and correct for the effects of rain. In advance of the conclusions of this study, the OVWM system architectures considered during the concept trade-off study shall not preclude the collection of passive microwave measurements.

3. An analysis should be conducted to determine the requirements for including a polarimetric radiometer measurement to enhance the wind retrieval performance. In advance of the conclusions of this study, the OVWM system architectures considered during the concept trade-off study shall not preclude the collection of passive polarimetric measurements.

## **2.9 Scatterometer Measurement Duration Issues**

Scatterometer “measurement duration” is defined as the time that it takes to complete all of the azimuth looks necessary in order to retrieve the wind vector. As the orbital altitude goes up, and the swath becomes larger, the time that it takes to make all of the azimuth measurements increases. This is an important consideration for this study because it may place an additional fundamental limit on the altitude of a multi-azimuth-look system. For the goals of the Phase I study, we therefore would like to establish reasonable criteria for how long the measurement duration can be at a given resolution.

A detailed analysis of the impact of increasing measurement duration requires simulated wind retrievals over time evolving wind fields with spatial scales much smaller than the desired resolution of the sensor. Such an analysis is quite complex, and beyond the scope of the present study. We therefore must make some simplifying assumptions to quantify the effect of measurement duration. One reasonable assumption, valid under many circumstances, is that the wind feature – such as a front or a storm – can be modeled as a feature which is only translating in time. In other words, such a wind feature more or less holds its shape over the measurement interval, but is moving horizontally at some speed.

To first order, the translating wind feature model is analogous to motion blurring that occurs for any imaging system. If a target is moving through the image plane of a camera, and no attempt is made to pan the camera during the integration time, a blurred image will result. The blurring function is a rectangular function of width equal to the product of the target speed and the integration time. The final resolution is then given by the convolution of the camera aperture function (the inherent resolution) and the blurring function. Camera resolutions significantly better than the order of the blurring resolution therefore achieve diminishing returns.

For scatterometers, the integration time is the measurement duration, which is the time that transpires between the first azimuth look and the last. A plot of this duration for conically scanning systems (discussed in Section 3) as a function of altitude for selected swath incidence angles is shown in Figure 2-12. For instance, for an incidence angle of  $60^\circ$ , and an altitude of 3000 km, the maximum measurement duration is 20 minutes. Note that for a conically scanning scatterometer, the maximum measurement duration is along the nadir track. At a point that is half way between the nadir track and the swath edge -- in the middle of the “sweet spot” -- this duration is reduced by a factor of approximately 0.86 (square-root three over two). At the swath edge, it approaches 0.



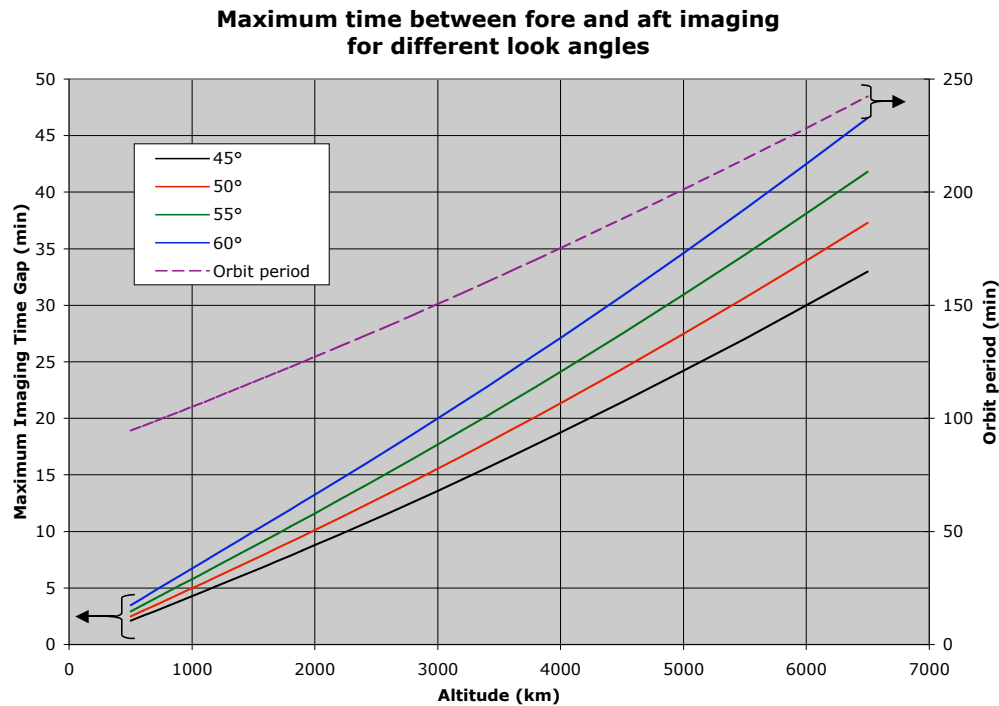


**Figure 2-12: Maximum measurement duration times for conically scanning scatterometer system as a function of altitude.**

The amount of “blurring” is given by the measurement duration times the translational (or advection) speed. Many interesting features “advect” at 10 m/s, and this value was judged to be a reasonable one to use for this analysis (M. Freilich, personal communication). Adopting 10 m/s as the feature translation speed, and using the above curves, we obtain the following blurring function resolutions for the 60° incidence case for different altitudes: 3 km resolution for 800 km orbit, 6 km resolution for 1500 km orbit, 12 km resolution for 3000 km orbit, 25 km resolution for 6000 km orbit.

Assuming that these blurring resolutions then indicate the maximum useful instrument resolutions at these altitudes, we would conclude the following:

1. Since the coarsest possible resolution that we could tolerate for OVWM is 25 km, orbits above 6000 km are likely not to be acceptable.
2. Orbits significantly above the MEO altitude of 1500 km may be marginal for achieving high resolution (i.e., resolutions better than 10 km).

Of course, these conclusions are very much a function of what advection speed we assume. As an example, a quick analysis was performed on how fast hurricanes move. The historical data base for the last five years on tropical storms was used, filtered for hurricane force winds, and plotted as a histogram of hurricane movement speed (the translation speed of the center of the storm). The results are shown in Figure 2-13. Both the mean and the mode are around 5 m/s, and there is a significant percentage of

occurrences above 10 m/s. Again, this does not represent movement of bands within the storm itself, which are likely to translate faster.

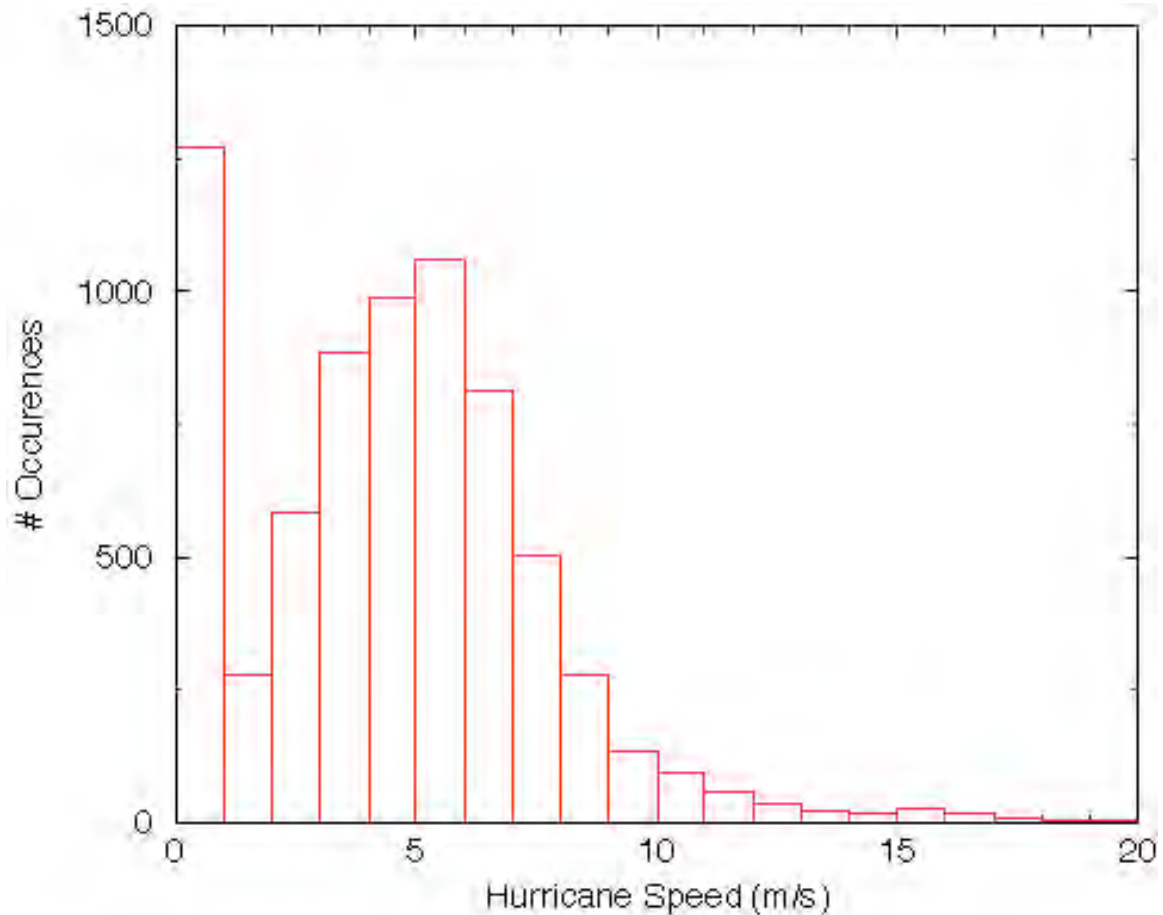


**Figure 2-13: Histogram of occurrences of hurricane advection speeds for years 1998-2003.**

## 2.10 References

Adams, I.S., Jones, W.L., Park, J.D., and Kasparis, T., "Improved Hurricane Wind Speed Algorithm for the SeaWinds Satellite Scatterometer," *Oceans '02 MTS/IEEE*, Volume 4, October 29-31, 2002.

Craeye, C., Sobieski, P.W., and Bliven, L.F., "Scattering by Artificial Wind and Rain Roughened Water Surfaces at Oblique Incidences," *Int. J. Remote Sens.*, Vol. 18, No. 10, 1997.

Donnelly, W.J., Carswell, J.R., McIntosh, R.E., Chang, P.S., Wilkerson, J., Marks, F., and Black, P.G., "Revised Ocean Backscatter Models at C and Ku-Band Under High-Wind Conditions," *JGR*, Vol. 104, No. C5, May 1999.

Draper, D.W., and Long, D.G., "Simultaneous Wind and Rain Measurements from SeaWinds Data," *SPIE International Symposium*, San Diego, CA, August 2003.

Grassotti, C., Leidner, S.M., Louis, J-F., and Hoffman, R.N., "Development and Application of a Visible-Infrared Rain Flag for Scatterometer Data," from *ESA Workshop on Emerging Scatterometer Applications*, ESTEC, Noordwijk, The Netherlands, October 1998.

Huddleston, J., and Stiles, B., "Multidimensional Histogram (MUDH) Rain Flag, Product Description Version 3.0," Jet Propulsion Laboratory, California Institute of Technology, May 1, 2000.

Jones, W.L., Mehershahi, R., Zec, J., and Long, D.G., "SeaWinds on QuikSCAT Radiometric Measurements and Calibration," *Proceedings of the International Geoscience and Remote Sensing Symposium*, July 2000.

Jones, W.L., Ahmad, K., Park, J.D., Kasparis, T., and Zec, J., "Validation of QuikSCAT Radiometer Rain Rates using the TRMM Microwave Radiometer," *Proceedings of the International Geoscience and Remote Sensing Symposium*, June 2002.

Kerkmann, J., and Klaes, D., "Perspectives for ASCAT on METOP," from *ESA Workshop on Emerging Scatterometer Applications*, ESTEC, Noordwijk, The Netherlands, October 1998.

Masuko, H., Okamoto, K., Shimada, M., and Shuntaro, N., "Measurement of Microwave Backscattering Signatures of the Ocean Surface Using X-Band and Ka-Band Airborne Scatterometers," *JGR*, Vol. 91, No. C11, 1986.

Quilfen, Y., Chaperon, B., Elfouhaily, T., Katsaros, K., and Tournadre, J., "Observation of Tropical Cyclones by High Resolution Scatterometry," *J. Geophys. Res.*, 103, pp. 7767-7786, 1998.

Shimada, T., Kawamura, H., and Shimada, M., "An L-Band Geophysical Model Function for SAR Wind Retrieval Using JERS-1 SAR," *IEEE Trans. Geosci. and Remote Sens.*, Vol. 41, No. 3, March 2003.

Spencer, M.W., and Shimada, M., "Effect of Rain on Ku-Band Scatterometer Wind Measurements," *Proceedings of the International Geoscience and Remote Sensing Symposium*, Helsinki, Finland, June 3-6, 1991.

Tsai, W-Y., Nghiem, S.V., Huddleston, J.N., Spencer, M.W., Stiles, B.W., and West, R.D., "Polarimetric Scatterometry: A Promising Technique for Improving Ocean Surface

Wind Measurements from Space,” *IEEE Trans. Geosci. and Remote Sens.*, Vol. 38, No. 4, July 2000.

West, R.D., and Yueh, S.H., “Atmospheric Effects on the Wind Retrieval Performance of Satellite Radiometers,” *Proceedings of the International Geoscience and Remote Sensing Symposium*, 1996.

Yueh, S.H., Wilson, W.J., and West, R., “Ocean Surface Wind Remote Sensing Using Microwave Backscatter and Brightness Temperatures,” *Proceedings of the International Geoscience and Remote Sensing Symposium*, 1998.

Yueh, S.H., Stiles, B.W., Tsai, W-Y, Hu, H., and Liu, T.W., “QuikSCAT Geophysical Model Function for Tropical Cyclones and Application to Hurricane Floyd,” *IEEE Trans. Geosci. and Remote Sens.*, Vol. 39, No. 12, December 2001.

Yueh, S.H., Wilson, W.J., and Dinardo, S., “Polarimetric Radar Remote Sensing of Ocean Surface Wind,” *IEEE Trans. Geosci. and Remote Sens.*, Vol. 40, No. 4, April 2002.

### 3. Scatterometer Instrument Concept Trade-Offs

In this section candidate scatterometer system architectures and their associated advantages and disadvantages are addressed. Based on the measurement requirements described in Section 2, there is a range of scatterometer architectures that could be envisioned. The most important issue, which impacts both performance and cost, is the antenna and scan architecture to be assumed. Wind scatterometers are radar instruments that are uniquely designed to measure the sea surface wind vector. In order to perform this measurement, the scatterometer instrument must have the following features:

1. *Multiple Azimuth Measurements:* A wind scatterometer must measure a given point on the ocean surface from at least three distinct azimuth angles in order to unambiguously retrieve the surface wind direction. (Note that this requirement may be relaxed when polarimetric scatterometry is fully demonstrated).
2. *Wide Swath:* A scatterometer must obtain a very wide swath of measurements in order to achieve adequate Earth coverage in a reasonable period of time.
3. *Radiometric Accuracy:* A scatterometer must obtain a very high degree of relative radiometric accuracy – on the order of 0.2 dB – in order to accurately retrieve the wind speed and direction, and be able to track subtle climate change signatures.

In addition to these required features, other design features, such as the ability to utilize multiple polarizations or the ability to make a collocated radiometer measurement, also enhance the performance of the system. In general, the dominant instrument design decision to be addressed in meeting these requirements is the selection of the antenna concept and the determination of how the surface is to be “scanned” by the antenna beam topology. Several scatterometer instrument architectures have been proposed over the years, and two distinct approaches – fixed antenna “fan-beam” systems and conically scanning “pencil-beam” systems – have been flown in space. In this subsection, the various options for scatterometer architecture are summarized.

#### 3.1 Fan-Beam Systems

The first radar instrument to thoroughly demonstrate the feasibility of wind measurement from space was the Seasat-A Scatterometer System (SASS) that was flown aboard the Seasat mission in 1978. The SASS instrument employed a “fan-beam” antenna approach. With the fan-beam design, several fixed antennas are used to cast long, narrow illumination patterns at the multiple azimuth angles required for wind retrieval (see Figure 3-1a). The narrow width of the antenna beam pattern provides resolution in one dimension, and Doppler or range filtering is employed to provide resolution in the elevation dimension of the footprint. Each point on the ground is viewed from different azimuth angles (corresponding to the different antennas on either side of the spacecraft)

as the satellite flies by. The SASS mission demonstrated the validity of the scatterometer wind technique and the utility of the resulting wind data. Due to this success, other fan-beam systems have been developed and flown during the last decade. These have included the C-Band scatterometer aboard the European Remote Sensing Satellite series (ERS-1 and -2) and the Ku-Band NASA Scatterometer (NSCAT) that flew aboard the Japanese Advanced Earth Observation Satellite (ADEOS-I). The fan-beam approach will also be used by the ESA ASCAT instrument.

The primary advantage of the fan-beam technique is that measurements on the surface are always made at the optimal azimuth angles. The ASCAT instrument, for instance, makes measurements at azimuths of  $45^\circ$ ,  $90^\circ$ , and  $135^\circ$  with respect to the spacecraft ground track direction, and thus yields a set of measurements with optimal “azimuth diversity” for wind retrieval. Another advantage is that the individual antennas are typically of rather simple construction (i.e., slotted waveguide), which do not need to be mechanically or electrically scanned.

From a science perspective, the primary disadvantage to fan-beam systems is that there is a distinct “nadir gap” region where the incidence angle is less than  $20^\circ$ , and consequently the wind cannot be retrieved (see Figure 3-1a). This nadir gap is typically a large percentage of the total swath, and limits Earth coverage as well as causes discontinuities in the measurements of large-scale features. From an implementation perspective, although the antennas are individually simple, the necessity for multiple antennas requires complex deployment mechanisms, and wide, unobstructed fields-of-view. Consequently, these systems can be difficult to accommodate aboard spacecraft. It is also impossible to make collocated radiometer measurements with fan-beam antennas due to the exceedingly long footprints. The loss associated with such antennas may also make them less than optimal for radiometer measurements.

### **3.2 Pencil-Beam Systems**

An alternate scatterometer design employed in recent years is the “pencil-beam” approach. In contrast to fan-beam systems, pencil-beam systems employ a single antenna that is conically scanned about the nadir axis to provide multiple azimuth measurements (see Figure 3-1b). Pencil-beam systems designed to measure ocean winds illuminate the surface with two beams slightly offset in angle: an “inner” beam and an “outer” beam. With this configuration, each point on the surface is viewed from up to four different azimuth directions -- twice by the inner beam looking forward then aft, and twice by the outer beam in the same fashion. This technique was employed by the Ku-Band SeaWinds scatterometer system launched on the QuikSCAT spacecraft in 1999 and the ADEOS-II spacecraft in 2002.

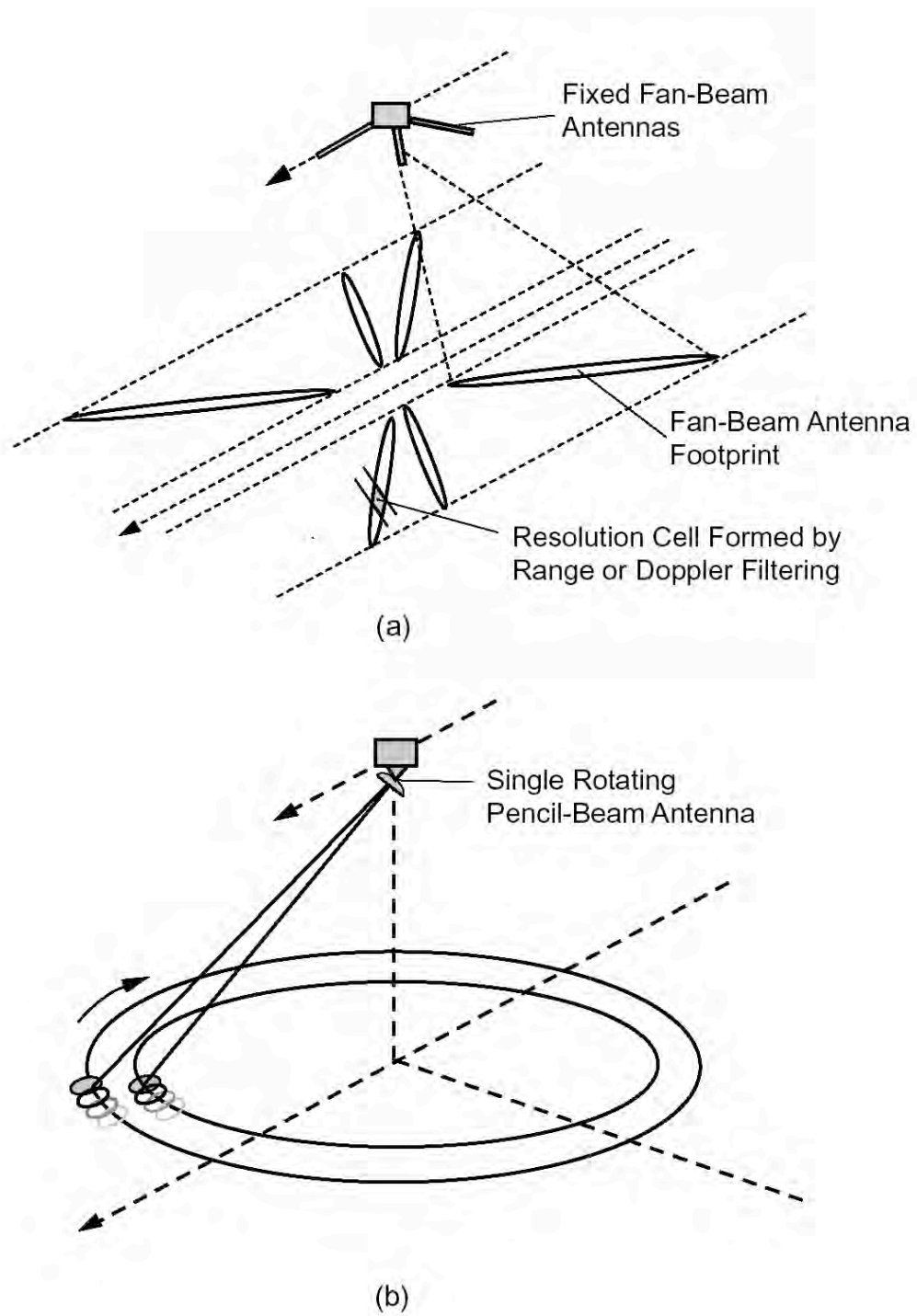


**Figure 3-1: a) Fan-beam scatterometer. b) Pencil-beam scatterometer.**

From a science perspective, the primary advantage of the pencil beam system is that it views the surface from a constant incidence angle, and there is thus no nadir gap region where the incidence angle is too small to retrieve the wind. Because of the narrow beamwidth in both the azimuth and elevation directions and because of the low-loss nature of most pencil-beam antenna designs, collocated radiometer measurements for rain correction can be made with the same antenna. Because the pencil-beam is typically formed using a reflector antenna, multiple polarizations and multiple frequencies are more easily incorporated. Also, because the beam can be made quite narrow, the potential exists to incorporate a SAR processing capability to improve the resolution an order of magnitude beyond the spot size -- i.e., to approximately 1 km. (Note that although a resolution of  $O(1 \text{ km})$  is a significant improvement relative to existing scatterometer systems, it is still much more coarse than that available with traditional side-looking SAR systems. This is because the scanning motion of the scatterometer antenna dramatically reduces the footprint dwell time, and hence synthetic aperture length. This issue is addressed in more detail later in this section.)

As higher orbits are considered, another advantage of the pencil-beam system is that the increase in the antenna gain compensates for the increased losses due to slant range. To see this, recall

$$SNR = \frac{P_t G^2 A_c \lambda^2 \tau \sigma_0}{(4\pi)^3 R^4 L N_0},$$

where  $P_t$  is the transmit power,  $G$  is the antenna gain in the direction of the measurement cell,  $A_c$  is the area of the measurement cell,  $\lambda$  is the wavelength,  $\tau$  is the integration time,  $R$  is the slant range to the resolution cell,  $L$  is the system loss, and  $N_0$  is the equivalent system noise power spectral density. The cell area is approximately given by

$$A_c \approx \frac{\lambda^2 R^2}{wh \cos \theta},$$

where  $w$  and  $h$  are the physical width and height of the antenna, and  $\theta$  is the incidence angle on the surface. The antenna gain can be similarly approximated by

$$G \approx \frac{4\pi wh}{\lambda^2}.$$

Using the two equations above, we can solve for the term  $wh$  and write

$$G = \frac{4\pi R^2}{A_c \cos \theta}.$$

Squaring the above expression for  $G$ , and inserting into the equation for  $SNR$ , we have that



$$SNR = \frac{P_t \lambda^2 \tau \sigma_0}{4\pi A_c \cos\theta L N_0}.$$

Note that if the area of the spot is kept as a constant, the *SNR* is independent of slant range from the surface, and  $P_t$  does not have to be increased in order to maintain *SNR*. This is a result of the fact that the antenna radius is proportional to the slant range.

From a science standpoint, the primary disadvantage of a pencil-beam scatterometer is that because the azimuth diversity varies over the swath, in some regions of the swath (such as the edges and near nadir) the wind retrieval performance may not be as accurate. From an implementation perspective, both the conically scanning motion of the antenna, and the increased area of the antenna to maintain a specific resolution present engineering challenges. Also, as the size of the antenna grows, the feed system may grow significantly more complex, as separate beams may be required for both transmit and receive.

### **3.3 Other Scatterometer Beam Architectures**

In addition to the fan-beam and pencil-beam architectures, a variety of other approaches have been considered to perform wind scatterometry from space. A summary of these architectures is given in Table 3-1, and a brief description is given below:

Table 3-1, Rows 1 and 2: These are the fan-beam and pencil-beam systems already discussed.

Table 3-1, Row 3: This concept utilizes an electrically steered set of pencil-beams, and was considered early in the development of SeaWinds. This system would combine the advantages the fan-beam approach (optimum azimuth angle diversity) with the advantages of the pencil-beam system (higher SNR, SAR possible, etc.). Although shown with a nadir gap, the beams could, in principle, be steered in elevation/azimuth space to yield measurements that close the gap. Such a system would require a relatively complex, electrically steered antenna, or perhaps multiple steered antennas.

Table 3-1, Row 4: This concept is essentially a conically scanning fan beam, and was proposed by Lin et al. as a follow-on to the C-Band fixed fan-beam antenna systems that the ESA is currently flying. The primary advantages are a much lower scanning rate than that required for a pencil-beam design and greater azimuth diversity going into the wind retrieval. Like traditional fan-beam systems, however, this system requires higher transmit power to achieve the same SNR, and cannot be used for radiometric or SAR measurements.

Table 3-1, Row 5: Here, the traditional fan-beam approach is altered to yield beams that avoid incidence angles lower than 20° and thus fill in the nadir gap. This is shown in Row 5 as two additional beams, but may also be satisfied by reorienting the existing

beams. Such a system will suffer all other noted disadvantages of a fan-beam architecture.

Table 3-1, Row 6: This concept simply recognizes the fact that the two pencil-beams need not be formed by the same antenna. In order to reduce the complexity of the feed, or to allow greater angular separation between the inner and outer beams, two antennas facing opposite directions may be employed. This approach was adopted for the JPL SCANSCAT proposal in the late 1980's.

Table 3-1, Row 7: The “half-scan” architecture shown here has only two azimuth looks at the surface, and therefore must take advantage of a polarimetric measurement in order to adequately constrain the wind direction. A key advantage of this approach is that it may be easier to accommodate on the spacecraft, particularly if the antenna is mounted on the top (i.e., zenith facing) surface of the bus.

Table 3-1, Row 8: Here, the “half-scan” is out to the side of the spacecraft ground track. Because four measurements are obtained, polarimetry is not required, but the swath is half as wide as in the previous example.

The above-discussed options are by no means exhaustive. Combinations of the various features from these approaches may be combined.

### **3.4 Architecture Trade-Offs and Baseline Architecture for Study**

As an example of the antenna architecture trade-offs encountered, we consider an example. Assume that the following general instrument characteristics are desired:

- 10 km spatial resolution
- 3400 km swath width (corresponds to an altitude of 1500 km for a 60° incidence angle)
- Ku-Band radar
- Antenna dimension of 4.5 m (derived from spatial resolution, altitude, and frequency)
- At least 3 azimuth “views” of the surface as the spacecraft flies by
- V and H polarized radar measurements
- Relative radar calibration stability of 0.2 dB (to allow wind measurements to have same accuracy as SeaWinds)
- Radiometer at 10 GHz or 18 GHz
- Current technology

To meet these parameters we consider three antenna architectures: the conically scanning pencil-beam system implemented as a rotating reflector, the azimuth/elevation scanning pencil-beam system implemented as a phased array, and a set of multiple, fixed fan-beam antennas. A summary of the performance and implementation trade-offs associated with these antenna options for the above described example are shown in Table 3-2. Areas colored *green* indicate that all performance requirements will be met or that the

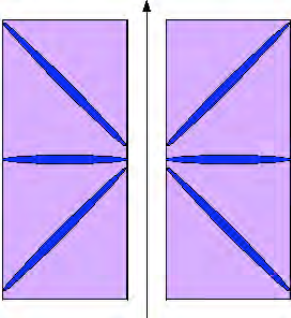
implementation is relatively straightforward. Areas colored *yellow* indicate that performance or implementation requirements may be more challenging to meet. Areas colored *orange* indicate that performance requirements may be very difficult to meet, or that implementation will likewise be quite difficult. Areas in *red* are where performance cannot be met or where implementation costs or risks may be prohibitive.

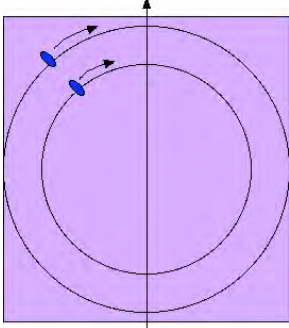
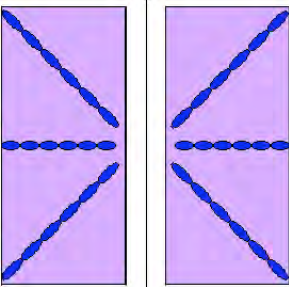
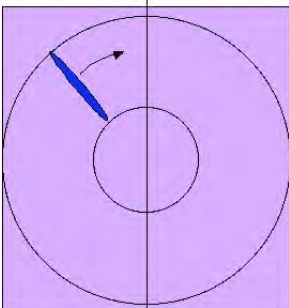
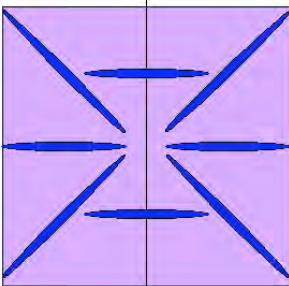
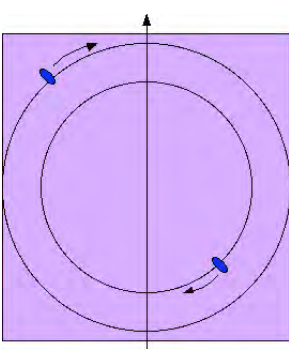
Examining Table 3-2, we see that the red areas only occur for the fan-beam antenna architecture. Because the antenna beams are extremely broad in the elevation dimension (100's of kilometers), they cannot be used for a radiometer where the resolution is determined by the size of the real-aperture footprint. Because the total area of the antenna is also quite small (in order that the pattern may be broad in the elevation dimension), the antenna gain does not adequately compensate for the increased altitude (relative to SeaWinds), and a peak transmit power of up to 800 Watts may be required. Because current Ku-Band transmit power technology is limited to a peak power of about 200 W, this may be prohibitive and is indicated by red as well.

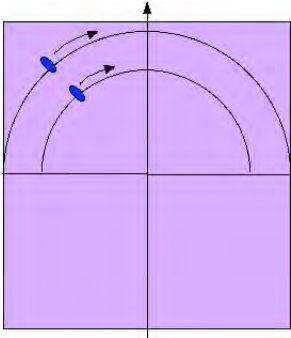
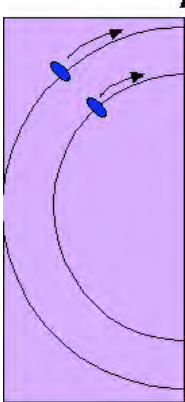
The phased array architecture forms a pencil-beam, but the radiometer requirements may still be quite difficult to meet, and are consequently designated as orange. The radiometer function requires an additional frequency other than Ku-Band, as well as a very low-loss antenna, both of which are difficult with a phased-array approach. The multiple frequencies, multiple polarizations, large size, and thousands of phase-shifters required for such an array lead to an electrical complexity also indicated as orange.

The conically scanning reflector is anticipated to meet all the performance requirements. The primary implementation difficulties are associated with spinning a 4.5-m antenna. Because of the ability to simultaneously achieve a wide swath, high resolution, multiple polarizations, as well as complimentary radiometer measurements, the conically scanning pencil-beam scan architecture is selected as the baseline approach for much of the Phase-1 study, and will consequently be the focus of the remainder of this report.

**Table 3-1: Scatterometer beam architectures.**

	<p>Scan Concept: "Fixed fan-beam." Three fixed fan beams covering swath on either side of S/C illuminating range of incidence angles.</p> <p>Heritage: Extensive. Slotted waveguide Ku-Band systems flown on Seasat (SASS) and ADEOS (NSCAT). Waveguide array C-Band systems on ERS-1 and ERS-2.</p>	<p>Advantages:</p> <ul style="list-style-type: none"> <li>• Fixed, non-moving antennas.</li> <li>• Optimal azimuth angles for wind retrieval.</li> </ul>	<p>Disadvantages:</p> <ul style="list-style-type: none"> <li>• Low incidence angle nadir-gap where wind can not be retrieved.</li> <li>• Radiometer measurement not possible.</li> <li>• More transmit power may be required for SNR.</li> <li>• Other polarizations, polarimetric more difficult.</li> <li>• Ambiguities may preclude use of Doppler sharpening (SAR)</li> </ul>
---	--	--	---

	<p>Scan Concept: "Conically scanning pencil-beam." Two conically scanning spot beams.</p> <p>Heritage: Extensive. Two-beam, 1 m rotating reflector Ku-Band SeaWinds instrument flown on QuikSCAT and ADEOS-2.</p>	<p>Advantages:</p> <ul style="list-style-type: none"> <li>Higher SNR.</li> <li>Radiometer measurement possible.</li> <li>Constant "usable" incidence angle.</li> <li>Multiple polarizations, polarimetric, different frequencies relatively easy to accommodate if reflector.</li> <li>SAR possible.</li> </ul>	<p>Disadvantages:</p> <ul style="list-style-type: none"> <li>Azimuth angle mix of measurements not optimal for wind retrieval over the entire swath.</li> <li>Rapidly moving antenna.</li> <li>Scanning loss and along-track continuity may require complex feed system.</li> </ul>
	<p>Scan Concept: Pencil-beam electrically scanned in optimal "X" pattern on the ground.</p> <p>Heritage: Considered for SeaWinds (implemented as phased array or Lunenburg lense), but rejected due to antenna complexity.</p>	<p>Advantages:</p> <ul style="list-style-type: none"> <li>Higher SNR.</li> <li>Optimal azimuth geometry.</li> <li>Radiometer more difficult.</li> <li>SAR possible.</li> </ul>	<p>Disadvantages</p> <ul style="list-style-type: none"> <li>Antenna complexity.</li> <li>Multiple polarizations, polarimetric, difficult.</li> </ul>
	<p>Scan Concept: Circular scan of broad fan-beam.</p> <p>Heritage: Proposed by ESA study.</p>	<p>Advantages:</p> <ul style="list-style-type: none"> <li>Slower scan rate, no scanning loss.</li> <li>Simple antenna to build and spin.</li> <li>More azimuth diversity going into wind retrieval.</li> </ul>	<p>Disadvantages:</p> <ul style="list-style-type: none"> <li>Antenna rotates.</li> <li>Lower SNR.</li> <li>Radiometer resolution poor.</li> <li>Ambiguities may preclude use of Doppler sharpening (SAR).</li> <li>Polarimetric more difficult.</li> </ul>
	<p>Scan Concept: Fan-beam system adjusted or augmented to eliminate nadir gap.</p> <p>Heritage: Proposed but not implemented.</p>	<p>Advantages:</p> <ul style="list-style-type: none"> <li>Fixed, non-moving antennas.</li> <li>Optimal azimuth angles for wind retrieval.</li> <li>No nadir gap.</li> </ul>	<p>Disadvantages:</p> <ul style="list-style-type: none"> <li>Radiometer measurement not possible.</li> <li>More transmit power may be required for SNR.</li> <li>Other polarizations, polarimetric harder.</li> <li>Ambiguities may preclude the use of Doppler sharpening (SAR).</li> </ul>
	<p>Scan Concept: Conically scanning pencil-beam with opposing inner and outer beams.</p> <p>Heritage: Proposed for SCANSAT.</p>	<p>Advantages:</p> <ul style="list-style-type: none"> <li>Higher SNR.</li> <li>Radiometer measurement possible.</li> <li>Constant "usable" incidence angle.</li> <li>Multiple polarizations, polarimetric, different frequencies rel. easy to accommodate if reflector.</li> <li>SAR possible.</li> <li>Potentially easier antenna implementation.</li> </ul>	<p>Disadvantages:</p> <ul style="list-style-type: none"> <li>Azimuth angle mix of measurements not optimal for wind retrieval over the entire swath.</li> <li>Rapidly moving antenna.</li> <li>Scanning loss and along-track continuity may require complex feed system.</li> </ul>

	<p>Scan Concept: Conically scanned pencil-beams. Rotating, but collecting data only over the forward half of the scan.</p> <p>Heritage: Similar scan to operational microwave radiometers.</p>	<p>Advantages:</p> <ul style="list-style-type: none"> <li>• Easier antenna accommodation on S/C.</li> <li>• Shorter time between fore/aft azimuth looks.</li> <li>• Radiometer measurement possible.</li> <li>• Constant "usable" incidence angle.</li> <li>• Multiple polarizations, polarimetric, different frequencies relatively easy to accommodate if reflector.</li> <li>• SAR possible.</li> </ul>	<p>Disadvantages:</p> <ul style="list-style-type: none"> <li>• Insufficient number of azimuth looks unless polarimetric is used.</li> <li>• Azimuth angle mix of measurements not optimal for wind retrieval over the entire swath.</li> <li>• Rapidly moving antenna.</li> <li>• Scanning loss and along-track continuity may require complex feed system.</li> </ul>
	<p>Scan Concept: Conically scanned pencil-beams. Rotating, but only collecting data over the side half of the scan.</p> <p>Heritage: Similar scan to operational microwave radiometers.</p>	<p>Advantages:</p> <ul style="list-style-type: none"> <li>• Easier antenna accommodation on S/C.</li> <li>• Radiometer measurement possible.</li> <li>• Constant "usable" incidence angle.</li> <li>• Multiple polarizations, polarimetric, different frequencies relatively easy to accommodate if reflector.</li> <li>• SAR possible.</li> </ul>	<p>Disadvantages:</p> <ul style="list-style-type: none"> <li>• Only half of swath coverage.</li> <li>• Azimuth angle mix of measurements not optimal for wind retrieval over the entire swath.</li> <li>• Rapidly moving antenna.</li> <li>• Scanning loss and along-track continuity may require complex feed system.</li> </ul>

**Table 3-2: Example antenna design trade-off matrix for 1500 km altitude, 10 km resolution concept with radiometer capability. *Green* indicates areas where the antenna will be completely suitable, *yellow* indicates areas where requirements will be more challenging to meet, *orange* indicates where requirements are difficult to meet, and *red* requirements cannot be met.**

<u>Antenna Architecture</u>	Performance Compliance				
	G = Meets, Y = More difficult to meet, O = Difficult to meet, R = Will not meet				
	Resolution	Polarization	Swath	Calibration	Radiometer
Scanning Reflector	Met with 4.5-m diameter	Multiple polarization feeds	Fixed 45° look angle (max)	Calibration independent of azimuth	Low-loss, low cross-pol antenna
Phased Array	Met with 6.4 x 6.4-m array.	Dual-Pol array with polarization synthesis	± 45° 2-D scanning	Different calibration for each beam position, polarization synthesis	Higher loss antenna, different frequency
Fan Beam	Met with 5-m long "sticks"	Separate H and V "sticks"	6 fixed "sticks"	Calibration of each stick pattern	Footprint too long
<u>Antenna Architecture</u>	Implementation Difficulty				
	G = Straightforward/high heritage, Y = More difficult/medium heritage, O = Difficult/low heritage, R = Most difficult/lowest heritage				
	Mech. Complexity	Elec. Complexity	S/C Accom.	Mass	Req. Tx Power
Scanning Reflector	Deployed reflector, spinning	Simple reflector/horn design	4.5-m spinning antenna	< 200 kg	100-W peak required
Phased Array	Large deployed structure (6.4 x 6.4 m)	Dual pol, 2-D steerable design	6.4 x 6.4 m array antenna	< 200 kg	More loss with array antenna
Fan Beam	Multiple (6) deployed "sticks"	Slotted waveguide antennas	6.5-m long antenna "sticks"	< 200 kg	> 500 W required to compensate for higher orbit

## 4. Orbit Trade-Offs

### 4.1 Overview

In this section, a generalized orbit trade-off study is performed for wind scatterometers, with the overall goal of identifying candidate orbits that optimize Earth coverage and revisit characteristics. Making the assumption that the extent of the scatterometer swath is limited by the maximum incidence angle allowable (discussed in Section 2.6), this study will apply equally to most of the instrument architectures described in Section 3.

The specific issues treated in this section are:

*Single OVWM Scatterometer:* A thorough study of the revisit characteristics of a single scatterometer as a function of orbit altitude is performed. The revisit statistics for a generic scatterometer operating at orbits between 800 km and higher are examined.

*Single OVWM Scatterometer Plus ASCAT:* The ability of the European ASCAT scatterometer to augment the coverage of a single NASA scatterometer is examined. Combined OVWM/ASCAT revisit statistics for selected OVWM orbits are presented.

*Multiple OVWM Scatterometers (i.e., OVWM Constellations):* An initial assessment of the potential for constellations of OVWM satellites (as opposed to a single satellite) to meet revisit needs is presented. Promising orbital altitudes/inclinations for such constellations are described.

*Radiation Environment:* An initial assessment of the radiation environment for higher orbits, and the likely impact on mission cost and risk, is provided.

### 4.2 Single Satellite Orbit Trade-Offs

The primary reason for considering different, higher orbits than those employed by previous scatterometers is to improve the sensor revisit and coverage performance. As discussed in Section 1, the *revisit time* is the interval between consecutive measurements of the wind at a given point on the Earth's surface. This parameter is important because the more frequent the measurements, the more capable the sensor is of detecting and tracking meteorological phenomena that change over time. The revisit time is not necessarily a single value, but may vary over time. For instance, a point may be measured twice within a 2-hour period, but not again for 12 hours. Useful metrics which give some overall insight into the revisit time characteristics include the average revisit time and maximum revisit time for points within a given latitude band. (The *refresh time* discussed in the IORD-II document is defined as the maximum value from the set of average revisit times for all points over the entire Earth).

The geographic *coverage* characteristics of a given orbit are related to how much of the Earth's surface is actually measured by the sensor. For example, a sensor flying in an equatorial orbit may yield excellent revisit times at tropical latitudes, but still have poor coverage because higher latitudes are systematically excluded. A commonly used coverage metric is the percentage of the area within a given latitude band measured as a function of time. Clearly, the concepts of coverage and revisit are linked. A point on the surface for which the revisit time goes to infinity is a point that is never covered by the sensor.

In this subsection, a survey of the orbital coverage and revisit properties of a single scatterometer operating in the MEO range above 800 km (the current LEO altitude used by SeaWinds and ASCAT is performed). First, a variety of terms are defined and the orbit analysis methodology is described. Next, results are presented for a range of orbit parameter values within the MEO range. Finally, these results are interpreted in light of the revisit requirements of the operational and science community.

#### **4.2.1 Orbit Analysis Methodology**

The key factor in determining Earth coverage and revisit characteristics is the scatterometer *swath width*. For a conically scanning scatterometer, the half swath width is defined by the length along the surface from the nadir point to the point on the surface where the measurement is made (see Figure 4-1). Because the antenna is conically scanned, the full swath width is twice this distance. Note that the two parameters that determine the swath width are the assumed incidence angle of the measurement and the orbital height. The higher the incidence angle or the orbital height, the wider the swath width. In Figure 4-2, for example, the wider swath width obtained by flying at a 1500 km orbit with a 60° incidence angle is compared with the swath obtained by flying at 800 km with a 54° incidence angle (the SeaWinds case). Note that whereas the 800 km, 54° case leaves gaps between successive swaths, the 1500 km, 60° case gives contiguous coverage between successive swaths.



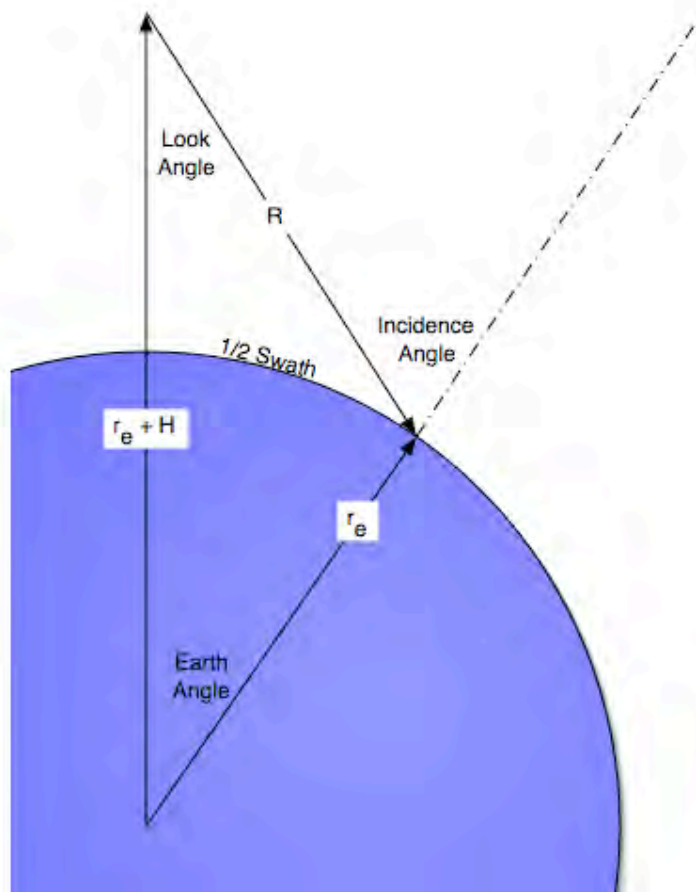
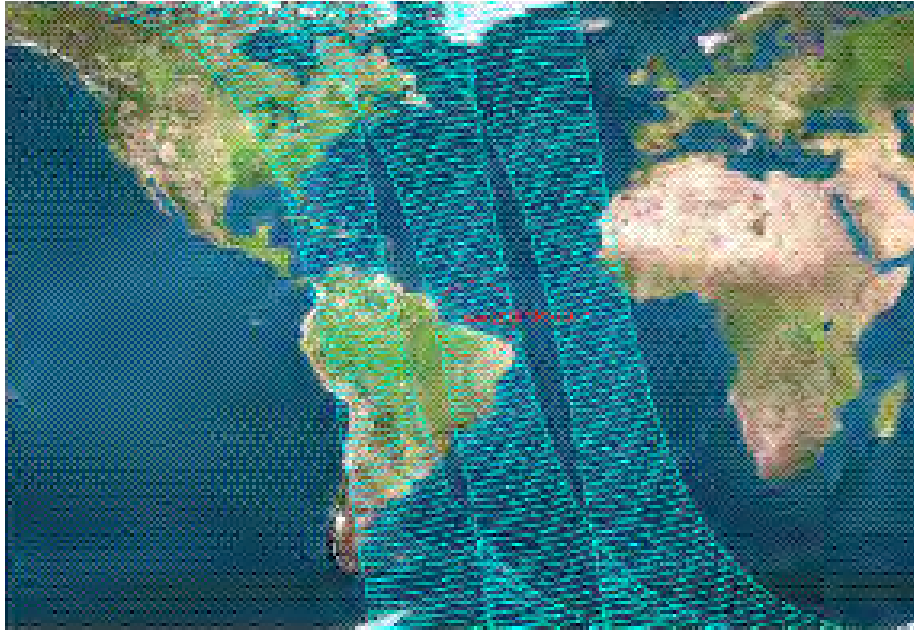
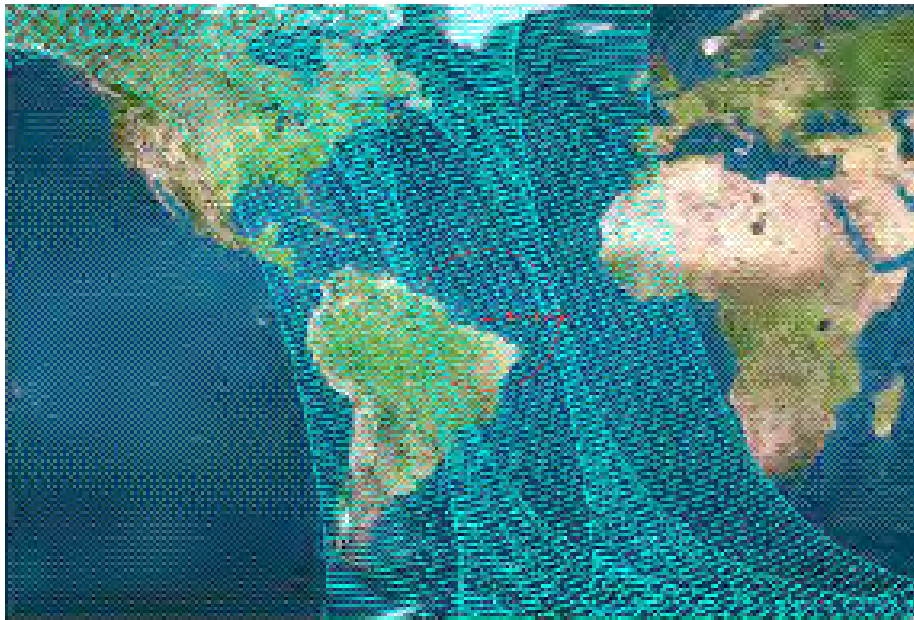


**Figure 4-1: Geometry showing the swath width as a function of spacecraft altitude (H). The 1/2 swath width along the surface is calculated from the altitude, the incidence angle, and local Earth radius ( $r_e$ ).**



a.



b.

**Figure 4-2: Example of three consecutive ascending swaths for: a) SeaWinds case (800 km altitude, 98 deg inclination, 54 deg incidence angle), and b) a MEO orbit at 1500 km, 98 deg inclination, and 60 deg incidence angle. Note that the combination of higher orbit and higher incidence angle produces successive swaths with no gap in between.**

In Figure 4-3, swath width is plotted vs. orbital height for various incidence angles. As described in Section 2.6, the highest allowable incidence angle, and therefore the

incidence angle that yields the widest swath width at a given altitude, is assumed to be 60°. Results at other incidence angles are also produced for two reasons. First, spacecraft accommodation constraints may dictate that the incidence angle be other than the desired value. Secondly, as described in Section 3, wind performance at the extreme edges of a conical swath may not be acceptable for some operational or research needs. Lower incidence angles may therefore be used to establish a smaller effective swath width where wind performance meets a more stringent set of requirements.

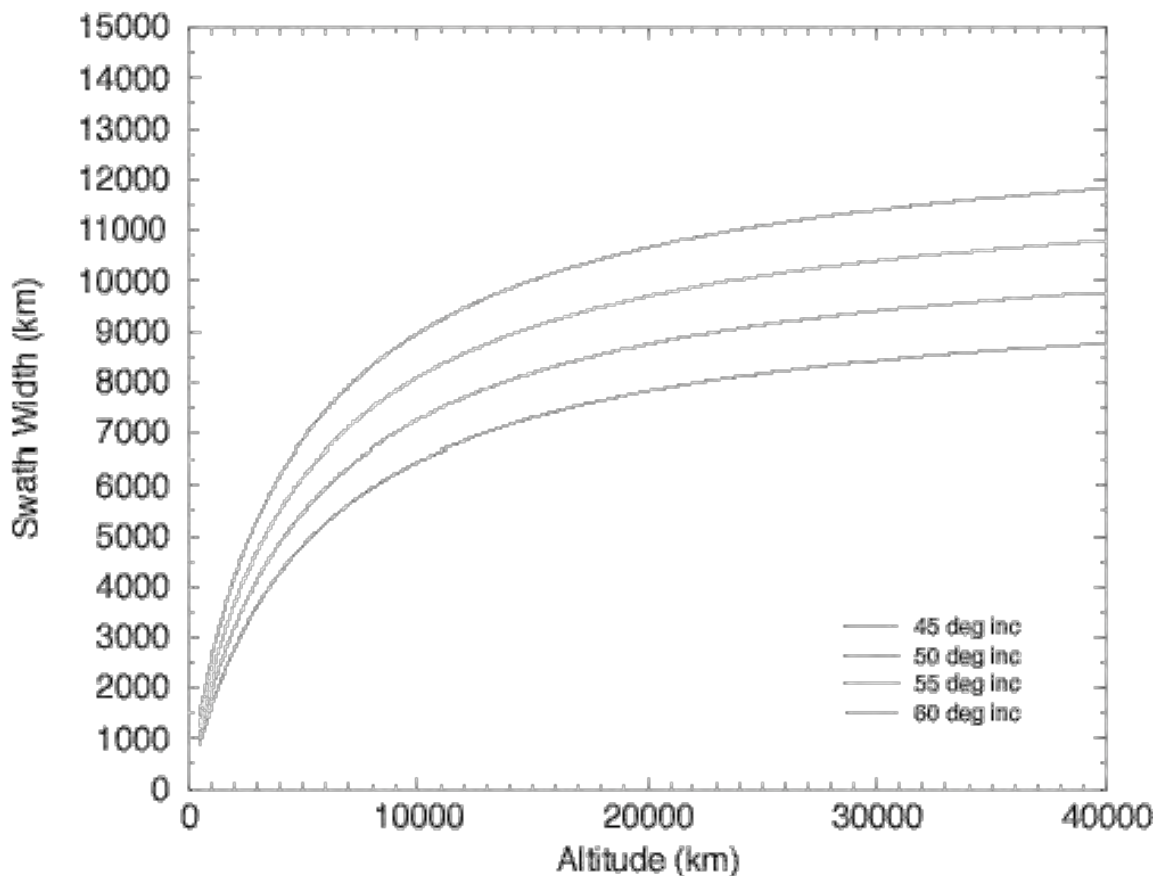


**Figure 4-3: Plot of swath width as a function of altitude for four different values of the incidence angle.**

As the orbit altitude increases in Figure 4-3, this has the effect of increasing the swath width, and consequently improving the coverage and revisit statistics. As the orbit altitude gets higher, however, the orbit period increases, and slows down the speed at which the swath moves over the Earth. The orbit period as a function of altitude is plotted in Figure 4-4. The increase in orbital period has the effect of reducing that rate at which points on the Earth are covered or revisited.

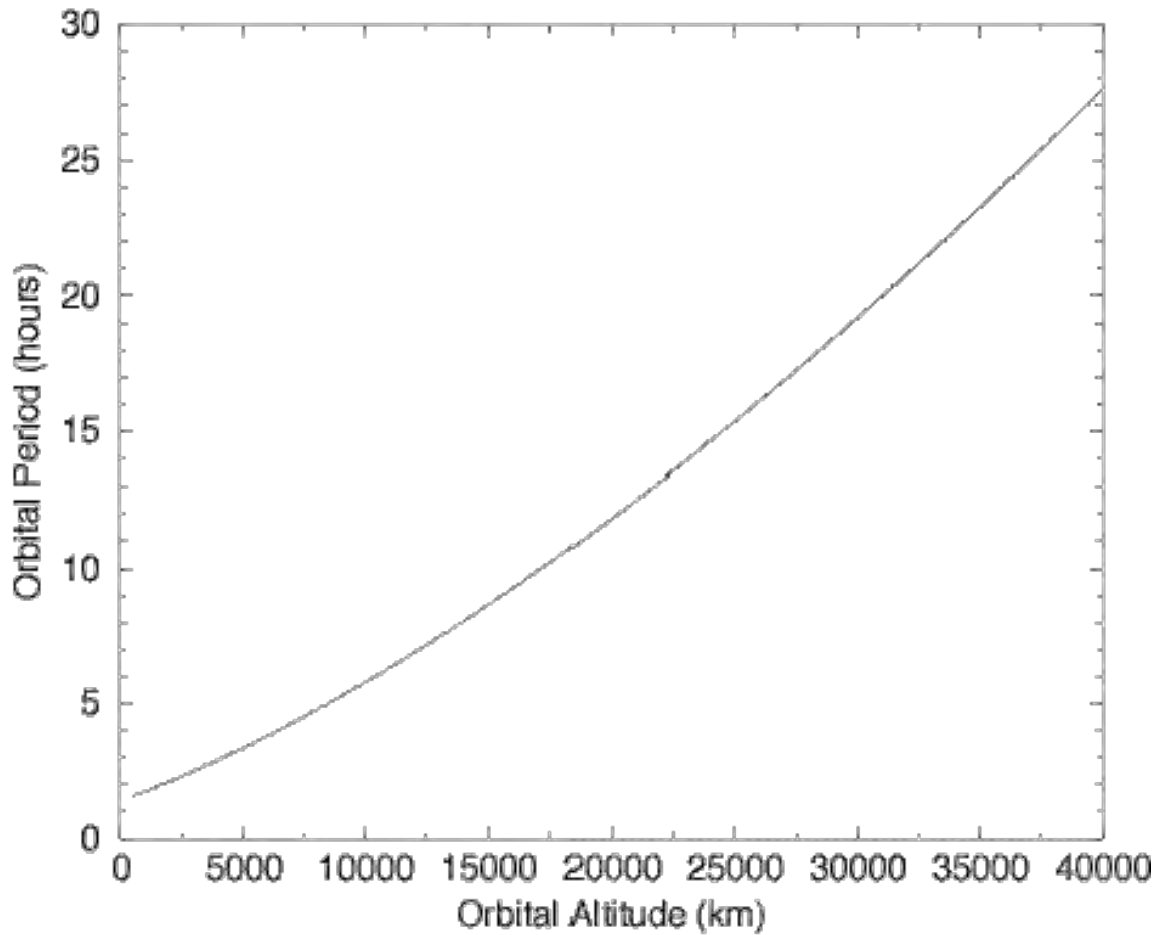


**Figure 4-4: Plot of orbital period vs. orbital altitude for circular orbits.**

A metric that combines the competing effects of increasing swath width and decreasing ground speed versus altitude is the so-called *swath coverage rate*. The coverage rate is defined as the product of the swath width and the satellite ground speed, and represents that rate at which Earth area is covered. In Figure 4-5 the coverage rate is plotted for a  $60^\circ$  incidence angle swath as a function of orbit height. Note that the rate increases rapidly as a function of height to a spacecraft altitude of 1500 km, flattens out to a peak around 3000 km, then decreases for higher altitudes. Based on this plot alone, it appears that there should be a fairly dramatic improvement in scatterometer revisit performance as altitudes are increased from the current 800 km up towards 3000 km, with limited improvement thereafter.

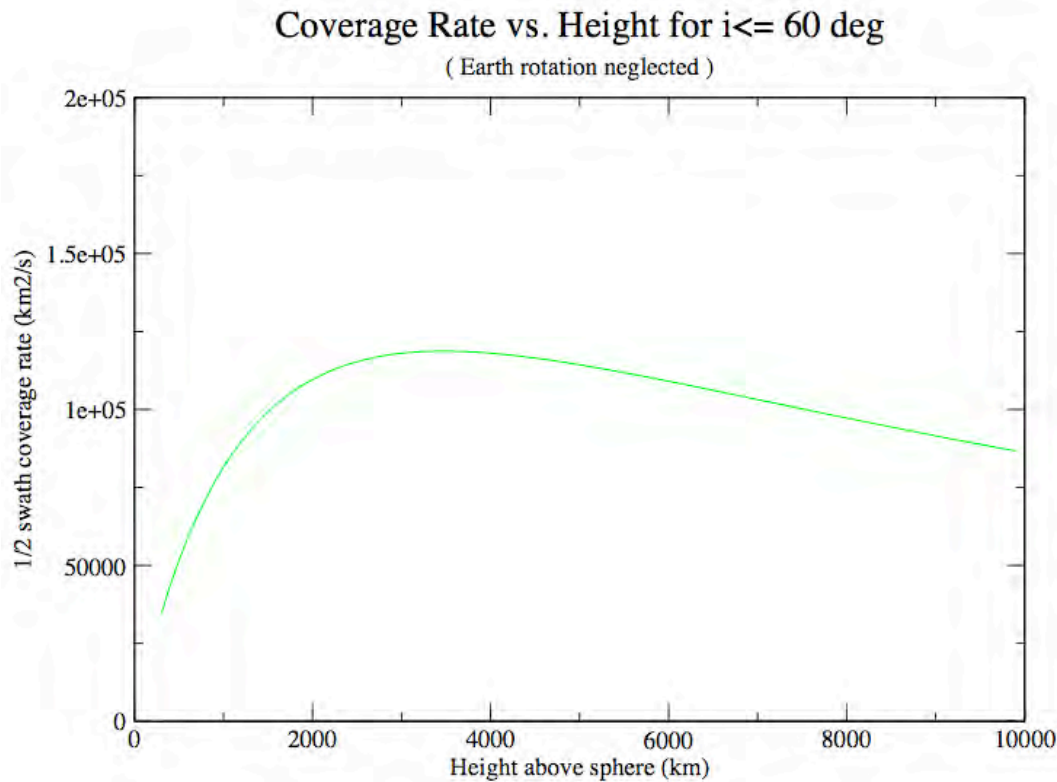


**Figure 4-5: Plot of coverage rate (orbital ground speed times swath width) as a function of orbital altitude.**

Of course the issues of orbital coverage and revisit are much more complicated than a simple consideration of the coverage rate. The complex interaction between orbit inclination, Earth rotation, and coverage at various latitudes requires a tool capable of simulating the spacecraft in orbit, and calculating the resultant coverage and revisit statistics. For these simulations, we employ two tools: 1) The Satellite Orbit Analysis Program (SOAP), developed by The Aerospace Corporation and widely used for orbit analysis at JPL, and 2) a tool modified from the JPL scatterometer performance analysis software.

Given a set of orbital elements and swath characteristics, SOAP accurately models the position of a platform and the Earth field of view of an instrument as a function of time. The program records when a specified point on the ground is in the field of view of the instrument. By utilizing a set of points on the ground covering a range of latitudes and longitudes, the resulting SOAP outputs can be used to generate the desired revisit statistics. A variety of point distributions were experimented with in order to determine the optimal set for computing representative revisit characteristics.

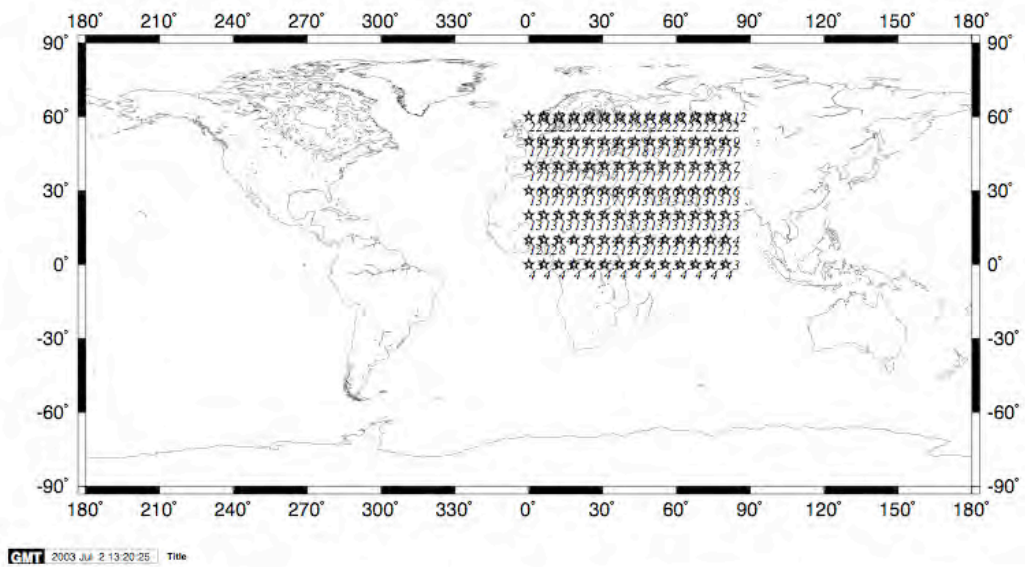


**Figure 4-6: Grid of test points on Earth for calculating revisit statistics with SOAP program.**

A regular grid of points uniformly distributed between  $0^{\circ}$  and  $60^{\circ}$  N latitude and  $0^{\circ}$  to  $80^{\circ}$  E longitude was found to be sufficiently extensive to accurately represent all regions of interest (see Figure 4-6). Because the swath is assumed to be symmetric about the spacecraft ground track, statistics for positive and negative latitudes are identical. Two sets of grid densities are used: 100 points spaced at  $10^{\circ}$  in latitude and  $5^{\circ}$  in longitude, and 1200 points spaced at  $2^{\circ}$  in latitude and  $2^{\circ}$  in longitude. The coarse grid case is used to save computation time and to perform a gross search over the revisit characteristics of a wide range of orbits (see Figure 4-7). The fine grid case is used to verify the accuracy of the tool and to yield more detailed results for selected orbits of interest (see Figure 4-8). For either the coarse grid or fine grid case, a variety of outputs can be generated including: a time history of revisit events for each test location in the grid, longitudinally averaged revisit time as a function of latitude, median revisit time as a function of latitude, maximum revisit time for set of points at a given latitude, etc. As a verification step, fine grid SOAP results computed for the SeaWinds orbit and swath were compared to previously published results from (Milliff et al. 2001), with good agreement being found.

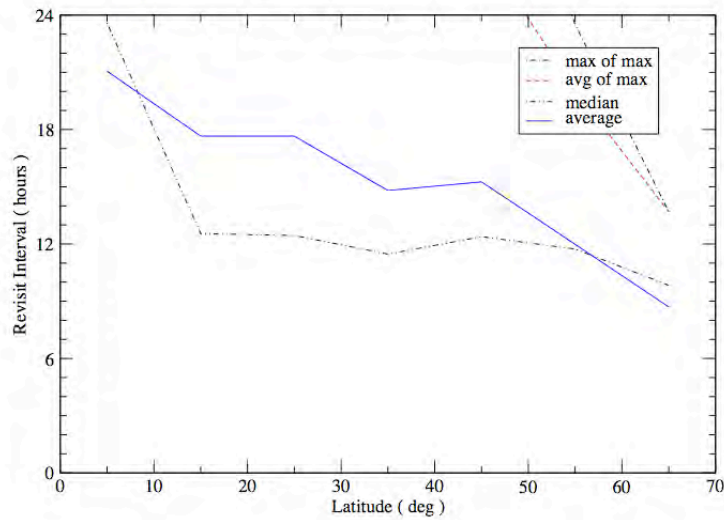


**Figure 4-7: SOAP plots of revisit statistics for coarse grid.**

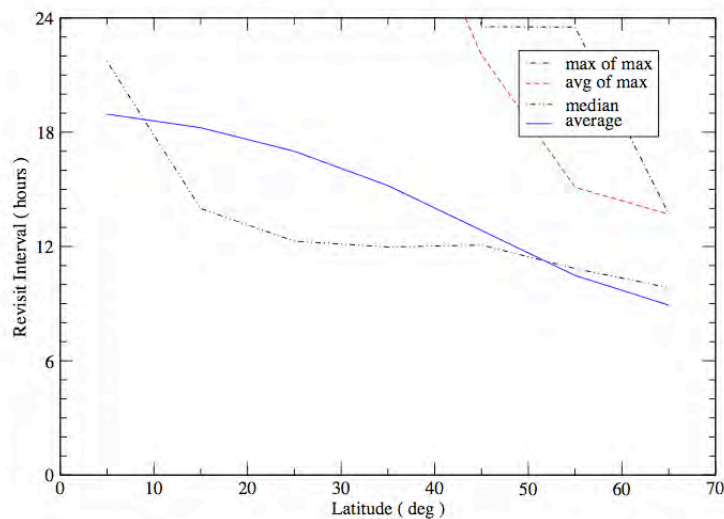


**Figure 4-8: SOAP plots of revisit statistics for fine grid.**

Rather than calculate statistics for a specific point on the surface (as SOAP does), the JPL scatterometer orbit analysis tool flies a simulated scatterometer over the surface of the Earth and records the positions of each wind measurement. This approach generally leads to a much faster collection of statistics from which to compute revisit time statistics, but does not directly generate the time series for each individual location on the Earth. The two tools are therefore used to generate complementary information. Head-

to-head comparisons of the output of the two tools were performed, and the results were found to be in good agreement.

#### 4.2.2 Single Spacecraft Analysis Results

Utilizing the software tools described in the previous sub-section, the revisit and coverage characteristics of a single spacecraft were systematically evaluated for a range of orbit altitudes and inclinations. In Figures 4-9 through 4-17, plots for the average and mean revisit time are presented for prograde orbit inclinations from  $0^\circ$  to  $80^\circ$ . In each plot, the y-axis shows how the revisit time varies as a function of altitude, and the x-axis shows how the revisit time varies as a function of Earth latitude. Black areas indicate latitude regions where no coverage is achieved.

The case of  $0^\circ$  inclination (Figure 4-9), in some sense, is a trivial case. The sensor sees a constant range of latitudes on either side of the equator, where the maximum latitude is a function of the swath width. The average and maximum revisit times are the same, and, for the  $0^\circ$  prograde case, are just a little greater than the orbital period due to the rotation of the Earth. The advantage of purely equatorial orbits is that they allow regular sampling at relatively frequent revisit intervals. As indicated in Figure 4-4, orbits below 10000 km yield regular revisit times of less than 6 hours. The disadvantage of these purely equatorial orbits is that they generally require a very high altitude in order to see a worthwhile portion of the globe. For instance, if we consider the latitude band between  $\pm 35^\circ$  latitude – a latitude band that would capture the tropics, as well as tropical storm events up to Cape Hatteras or Tokyo (see Figure 4-25) – then an orbital altitude of 6000 km would be required. As described in Section 2.9, this altitude will yield measurement durations inconsistent with resolutions better than about 20 km, and may be of limited utility for fast moving systems. Also, the highest latitudes will be at the very extremes of the swath. For a conically scanning system, these will then be latitudes where the measurements are of a quality that is consistently inferior to that of the rest of the swath.

At the other extreme we consider the case of a near-polar orbit at  $80^\circ$  inclination. Examining Figure 4-17, we see that there are no blackened areas, and thus this orbit covers all regions of interest – both high and low latitudes. Also, note how performance improves rapidly moving from 800 km (the current SeaWinds orbit) to about 1500 km, then levels out somewhat at higher latitudes. The reason for this can be observed readily from an examination of Figure 4-2. Here, we observe that at around 1500 km, successive swaths for a near-polar orbit begin to touch each other, leaving no gap in between. In addition to bringing about improved statistics, this characteristic has been identified as a highly desirable one in the IORD-II document.

Another way to see this swath contiguity effect is in the so-called “hit” plots in Figures 4-22 and 4-23. Here, the x-axis represents the time in days, and the lines on the y-axis represent each point in the SOAP “coarse grid” of 100 points described above. Points with different latitude and longitude are represented on the plot. For instance, all the lines between  $0^\circ$  and  $10^\circ$  on the y-axis represent points at latitude  $0^\circ$  but covering a



variety of longitudes between  $0^{\circ}$  E and  $80^{\circ}$  E. Each star indicates the time at which that grid point was measured or “hit” by the sensor. Note that for the 800 km case in Figure 4-22, points on the equator are irregularly sampled. Most of the time the sampling interval is 12 hours, corresponding to the half rotational period of the Earth as points are alternatively hit by ascending and then descending passes, but occasionally a period of 24 hours transpires between samples, corresponding to the gaps between the swaths. For the same latitude in Figure 4-23, however, regular sampling of 12 hours is achieved. Occasionally, the sample period is as small as 2 hours, corresponding to the orbital period, because there is a small overlapping region shared by successive swath passes. These appear as paired “doublets” of hits.

To summarize, therefore, the advantages of high inclination orbits is that they 1) cover the entire Earth region of interest, and 2) achieve maximum effectiveness at a relatively low altitude of 1500 km. The primary disadvantage is that the desired 6-hour revisit time cannot be achieved with a single satellite.

Orbits with *medium* inclinations, between either purely equatorial or purely polar inclinations, hold out the promise of perhaps combining some of the advantages of both extremes. Results for these orbits are plotted in Figures 4-10 to 4-16. As an example, consider Figure 4-13. Here, coverage up to  $50^{\circ}$  latitude (and above) is obtained. Note also that between the altitudes of about 1500 and 4000 km there are large “lobes” covering tropical latitudes, where an average revisit time of 6 hours is achieved. An examination of the maximum revisit time plot for this case, however, indicates that maximum revisit values in these lobe areas exceed 12 hours, and can even approach 24 hours. More detailed insight is given by examining the “hit” plot for this case presented in Figure 4-24. Here, we see that for points at  $30^{\circ}$  latitude, there is alternatively a “burst” of revisits at an interval of the orbital period of 2 hours, followed by a “lull” of 16 hours where no hits are obtained. This irregular sampling yields an average revisit of less than 6 hours, but may not be more desirable than the regular 12-hour sampling obtained with the polar inclinations.

The plots in Figures 4-9 through 4-17 have covered a range of prograde inclinations. Selected examples for retrograde inclinations are given in Figures 4-18 through 4-20. Retrograde orbits yield slightly better revisit statistics because the longitudinal component of the spacecraft ground track is moving in the opposite direction of the rotation of the Earth, therefore yielding a faster effective ground track speed. In general, the qualitative features of retrograde orbits with equatorial, medium, and polar inclinations are similar to their prograde counterparts. Overall revisit times are on an order of an hour faster, however, and therefore features such as the “lobe” of good revisit discussed for  $40^{\circ}$  inclination is somewhat larger for  $140^{\circ}$  inclination.

A special case of retrograde orbits is the sun-synchronous case shown in Figure 4-21. Sun-synchronous orbits are advantageous from the perspective of spacecraft design because the sun is in the same general direction relative to the orbit plane throughout the year. To maintain a sun-synchronous orbit, there is a specific inclination that is required as a function of altitude (see Figure 4-26). For relatively low orbits, the sun-synchronous

inclination is nearly polar, and performance is quite similar for that described for polar orbits above. As the altitude approaches 6000 km, however, the inclination required “keels over,” and the orbit, as well as the revisit statistics, approach that for a retrograde equatorial orbit.

#### **4.2.3 Summary of Single Satellite Revisit and Coverage Characteristics**

Based on the analysis of a single satellite in a MEO orbit, we conclude that:

1. A single satellite cannot simultaneously obtain *regular* 6-hour revisit sampling and full coverage over the desired ocean region between 60° S and 60° N latitude.
2. With a single satellite flying in an equatorial orbit, regular 6-hour revisit of tropical regions can be achieved, but at the expense of lost coverage at mid-latitudes, as well as some significant issues concerning the relatively long azimuth measurement durations associated with high altitudes.
3. Satellites flying in near-polar MEO orbits (including sun-synchronous) obtain good global coverage, produce contiguous swaths at the equator, and can achieve results comparable to the QuikSCAT/Midori tandem mission at a relatively low altitude of 1500 km.
4. MEO orbits with medium inclinations achieve large areas where the average revisit is better than 6 hours. The sampling, however, is not regular, but is characterized by “bursts” and “lulls” in revisit intervals.
5. For the purposes of further system studies, several altitudes have been identified as “knees in the curve” relative to revisit performance: 1500 km, where consecutive swaths are contiguous, 3000 km, where coverage rate is at a maximum, and 6000 km, the maximum altitude that meets the measurement duration constraints described in Section 2.9 and the altitude at which equatorial orbits reach up to a latitude of 35°.

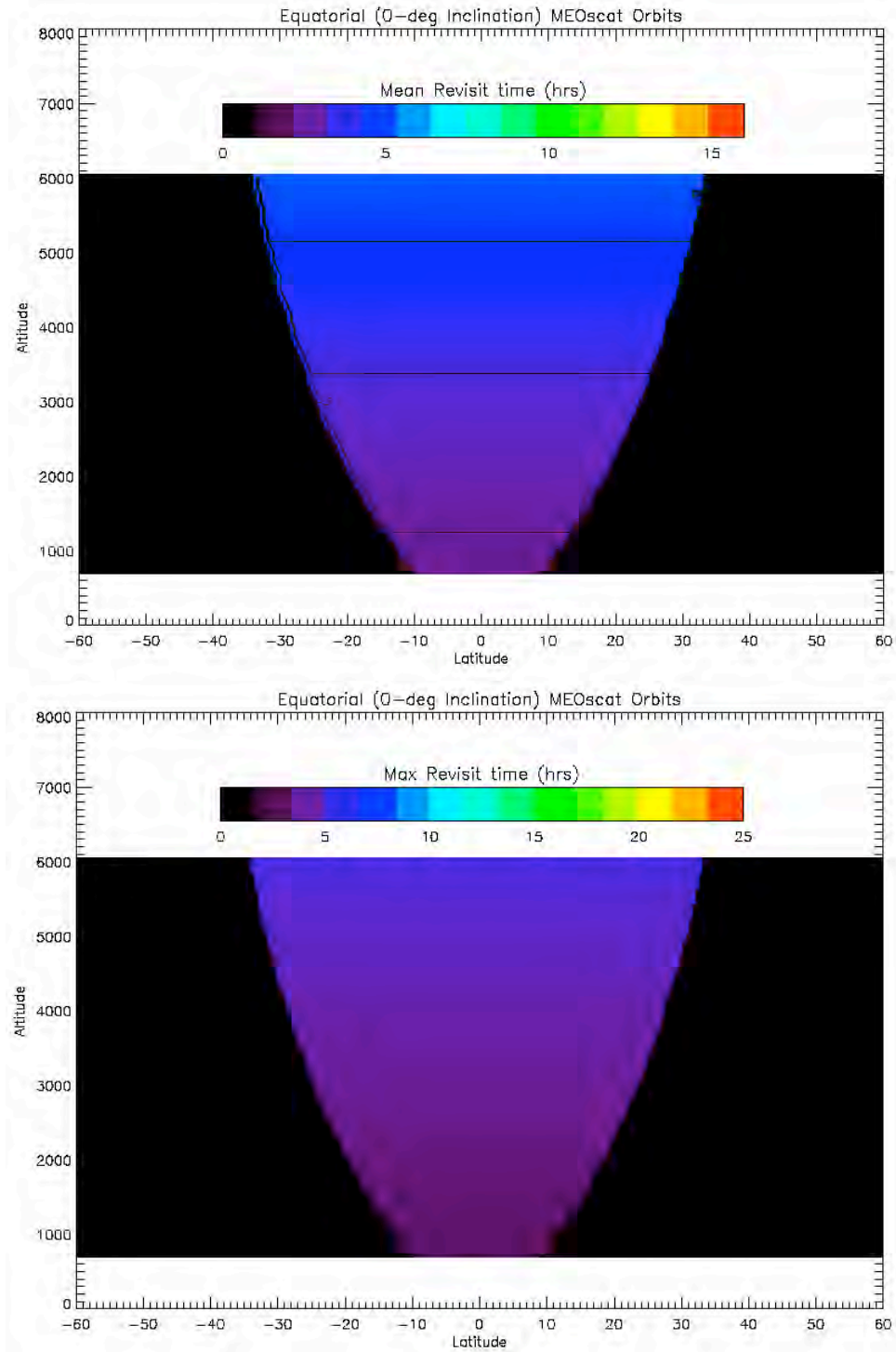


**Figure 4-9: Mean (top) and maximum (bottom) revisit times as a function of altitude (y-axis) and Earth latitude (x-axis) calculated for a single satellite in a circular, 0 deg inclination orbit.**

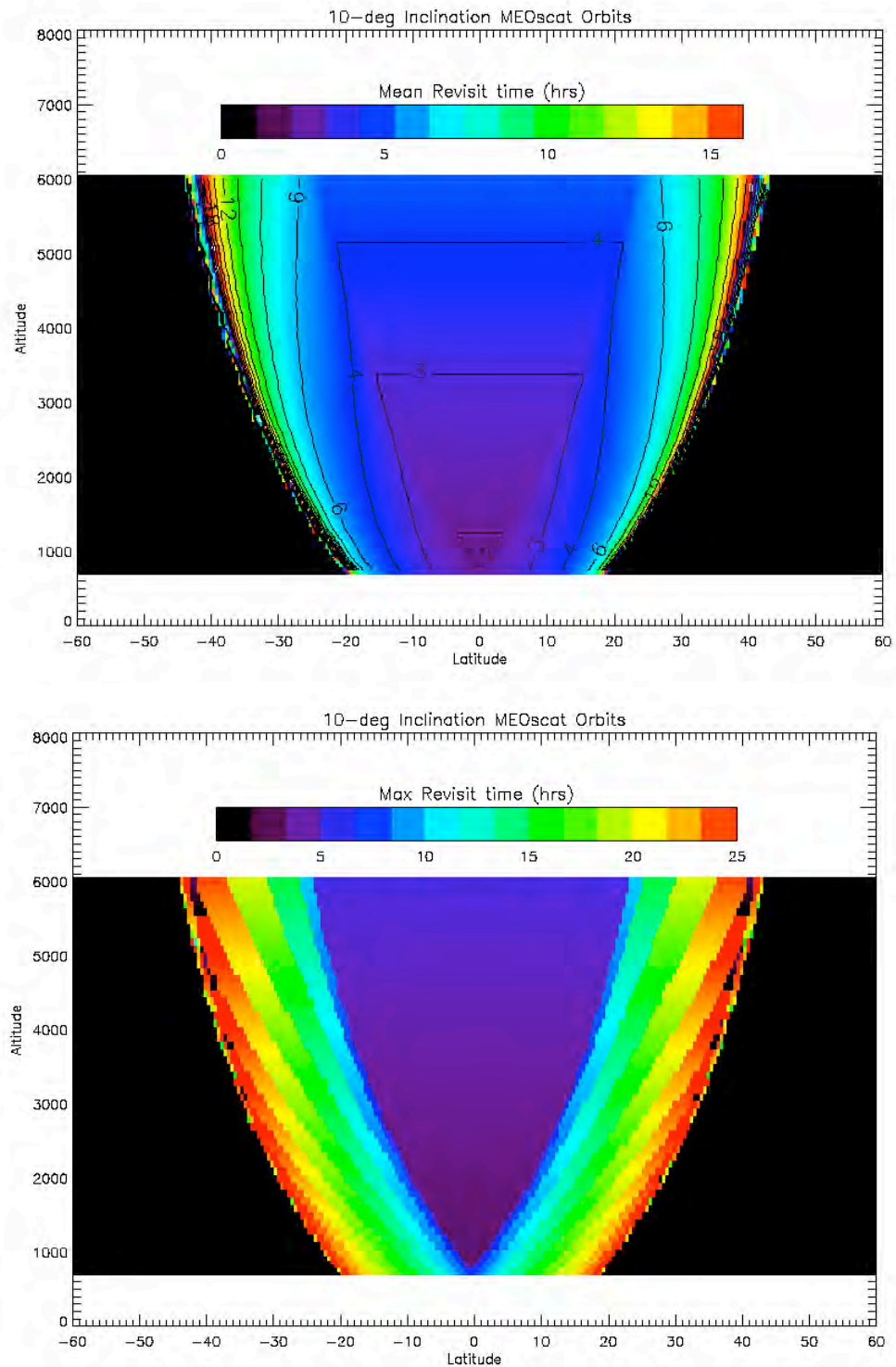


**Figure 4-10: Mean (top) and maximum (bottom) revisit times as a function of altitude (y-axis) and Earth latitude (x-axis) calculated for a single satellite in a circular, 10 deg inclination orbit.**

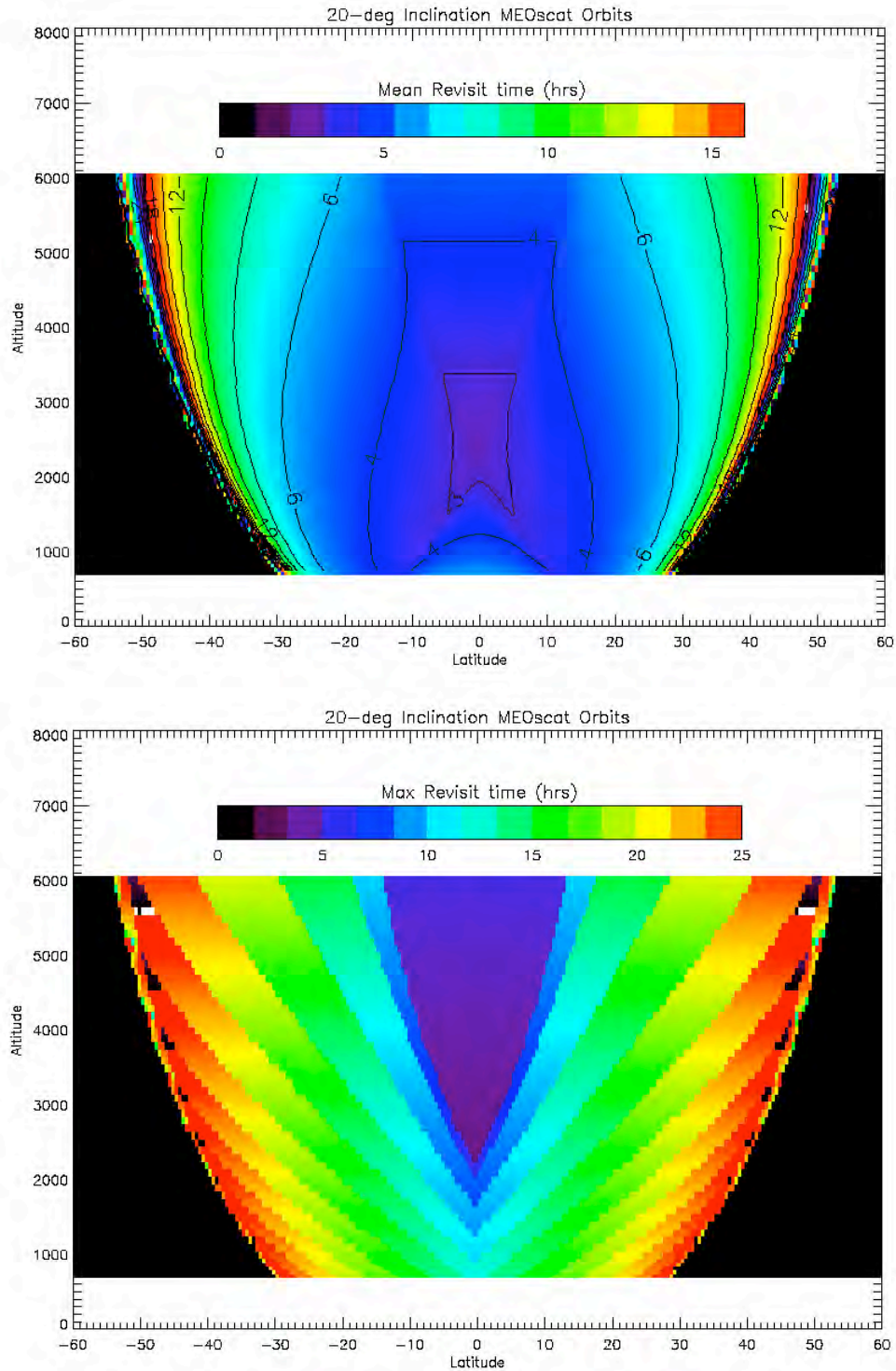


**Figure 4-11: Mean (top) and maximum (bottom) revisit times as a function of altitude (y-axis) and Earth latitude (x-axis) calculated for a single satellite in a circular, 20 deg inclination orbit.**

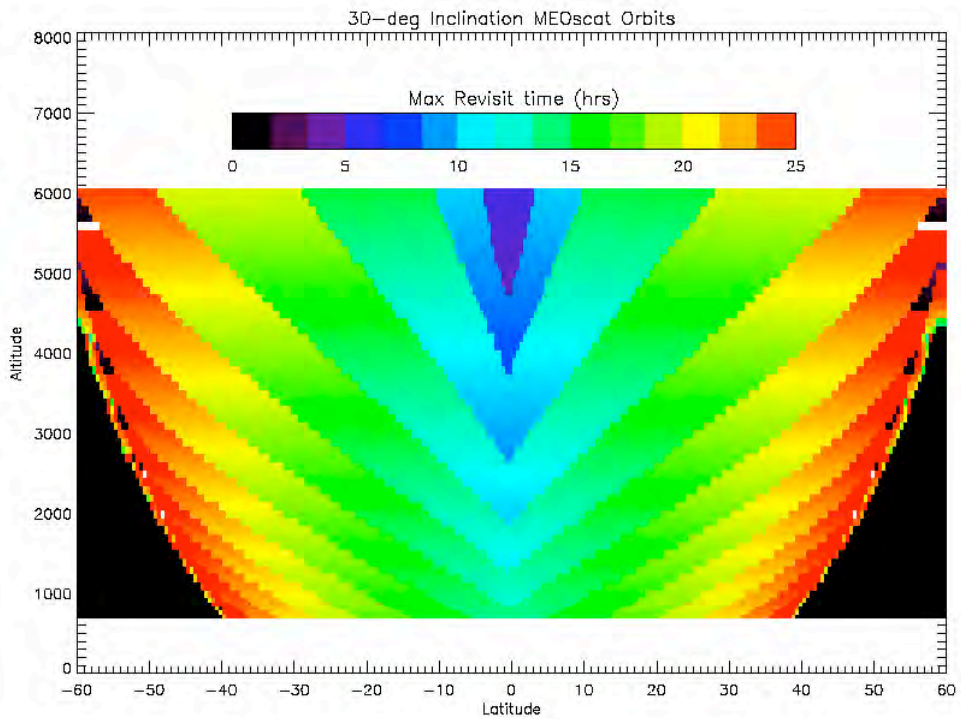
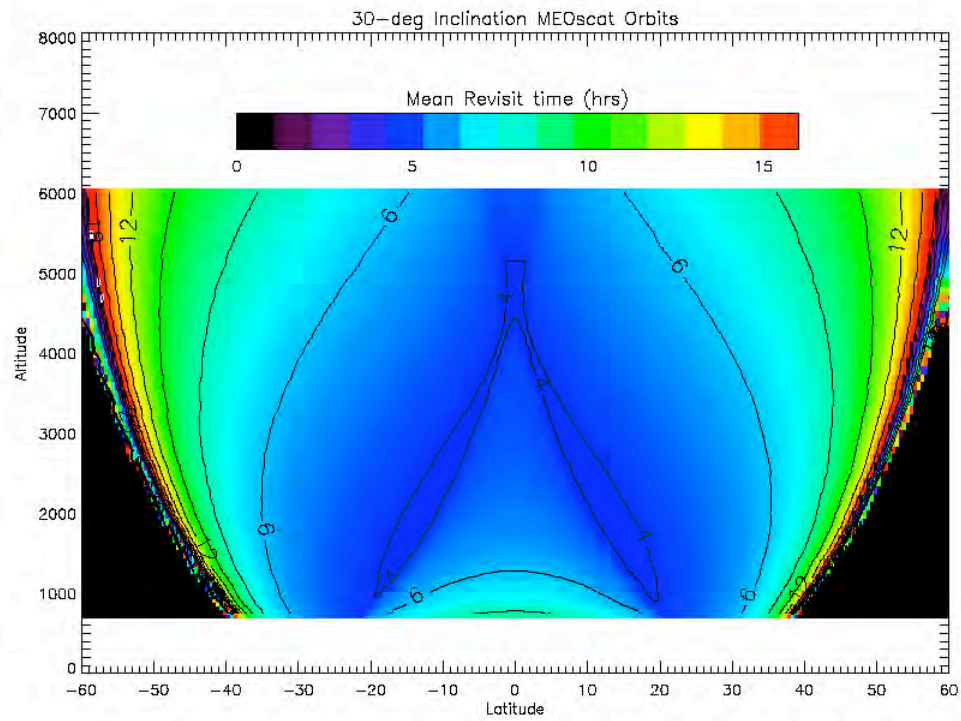


**Figure 4-12: Mean (top) and maximum (bottom) revisit times as a function of altitude (y-axis) and Earth latitude (x-axis) calculated for a single satellite in a circular, 30 deg inclination orbit.**



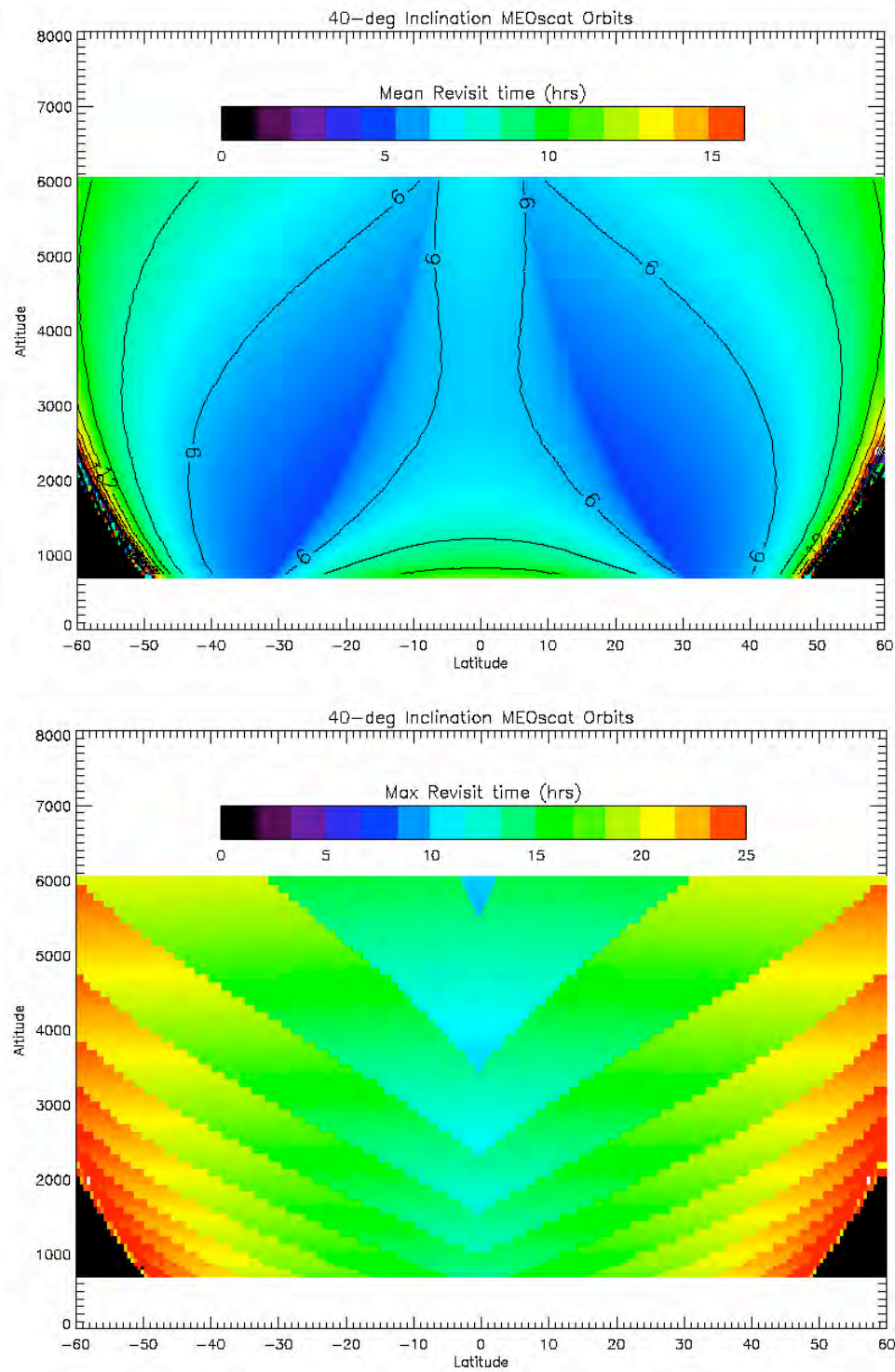


**Figure 4-13: Mean (top) and maximum (bottom) revisit times as a function of altitude (y-axis) and Earth latitude (x-axis) calculated for a single satellite in a circular, 40 deg inclination orbit.**

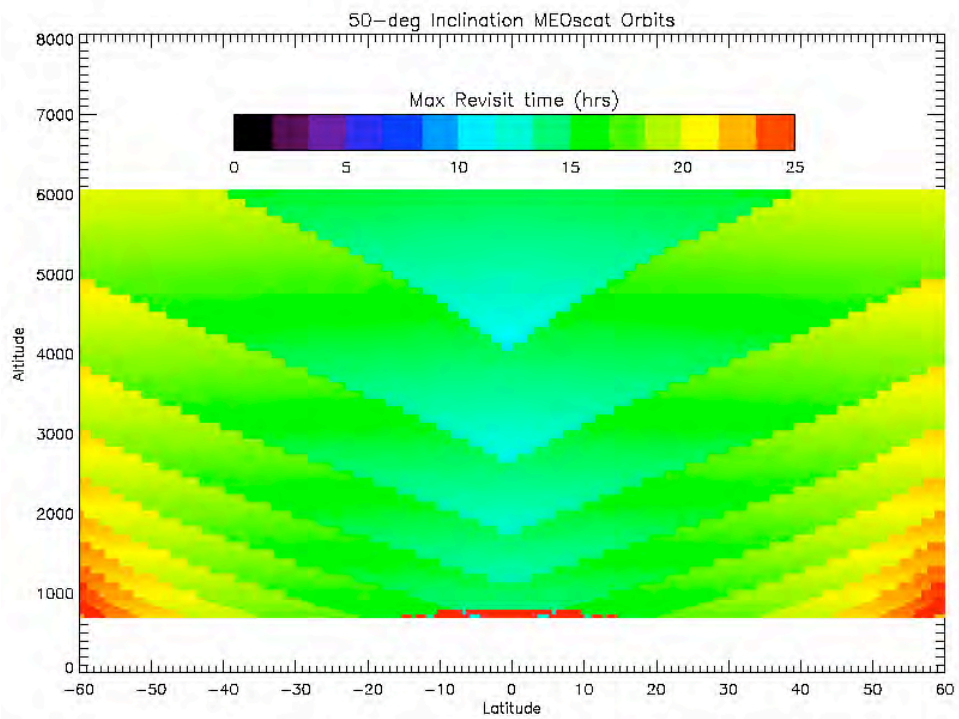
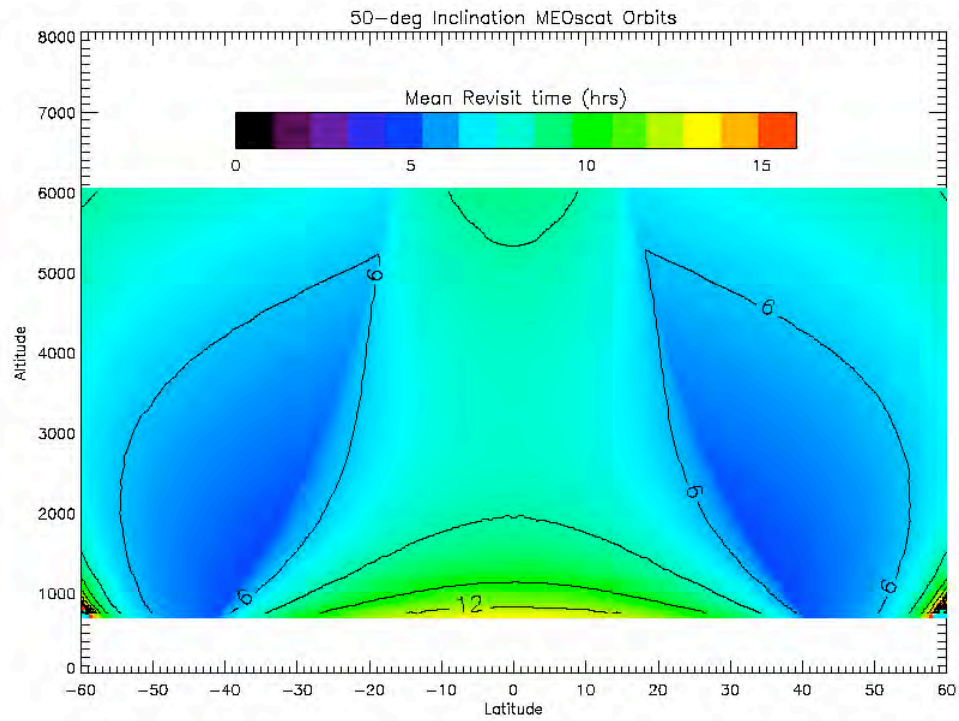


**Figure 4-14: Mean (top) and maximum (bottom) revisit times as a function of altitude (y-axis) and Earth latitude (x-axis) calculated for a single satellite in a circular, 50 deg inclination orbit.**



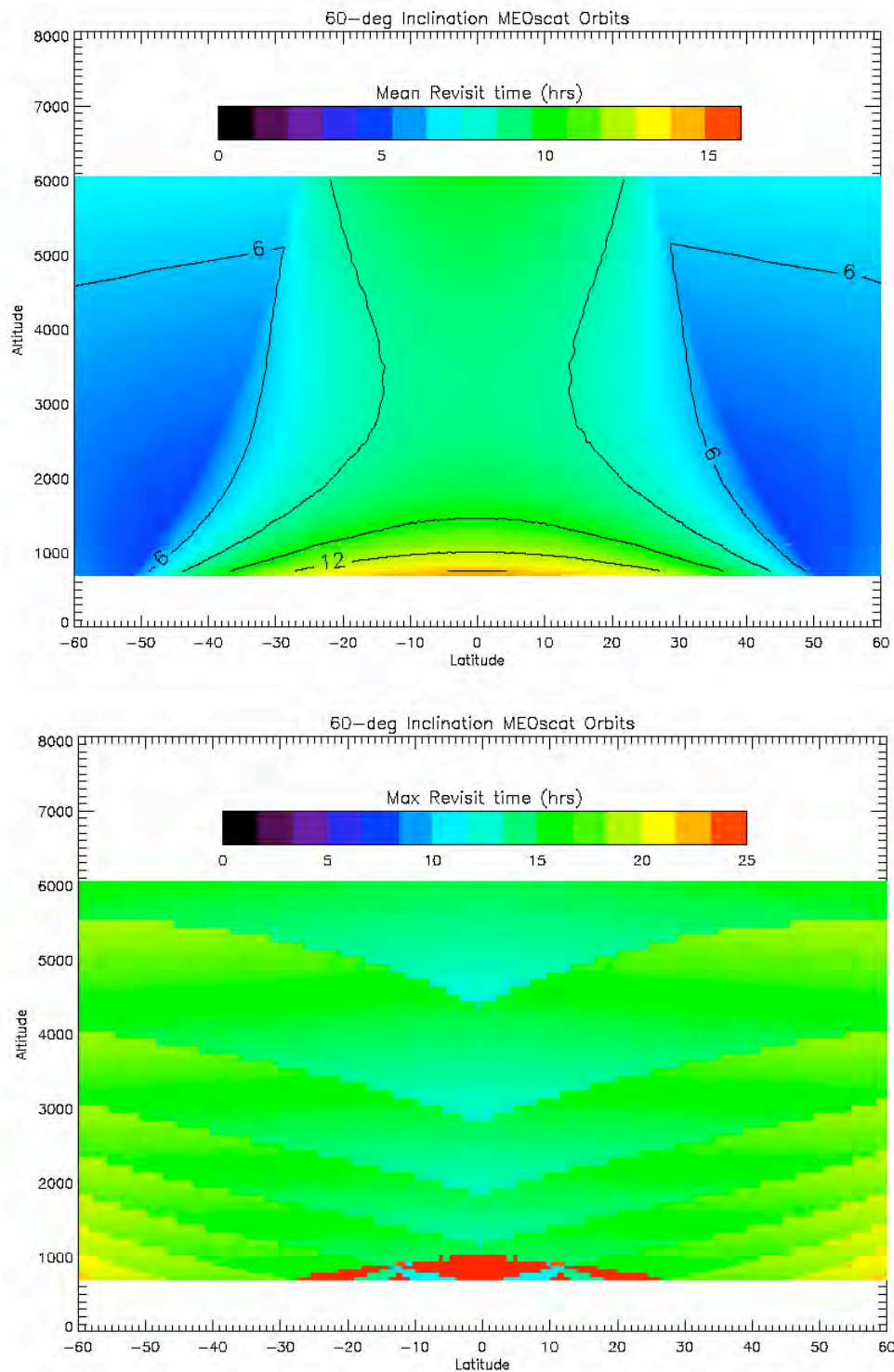


**Figure 4-15: Mean (top) and maximum (bottom) revisit times as a function of altitude (y-axis) and Earth latitude (x-axis) calculated for a single satellite in a circular, 60 deg inclination orbit.**

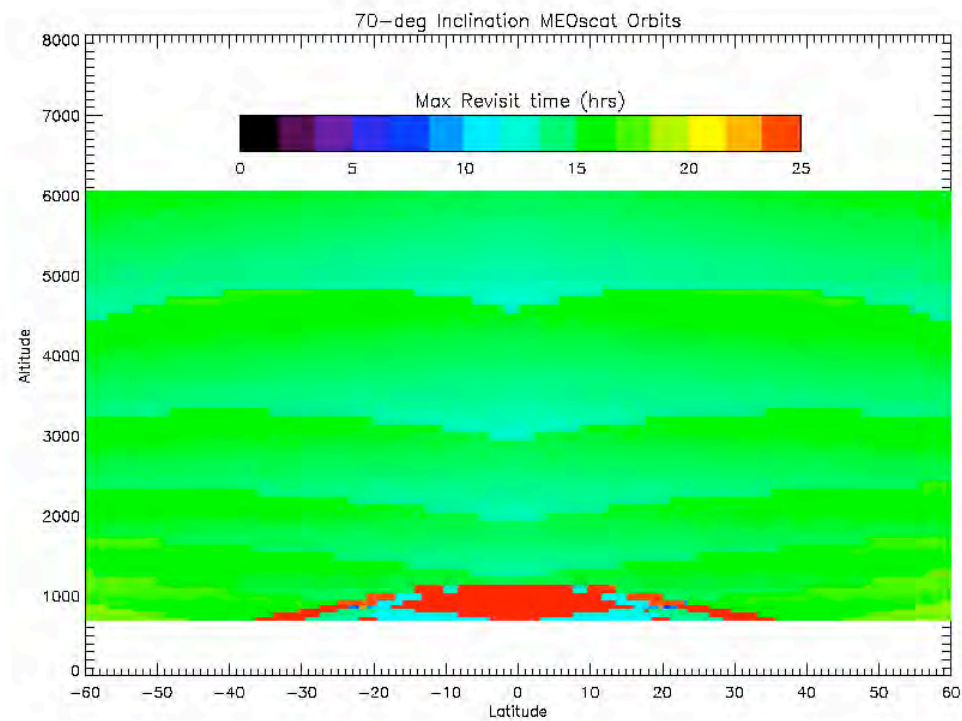
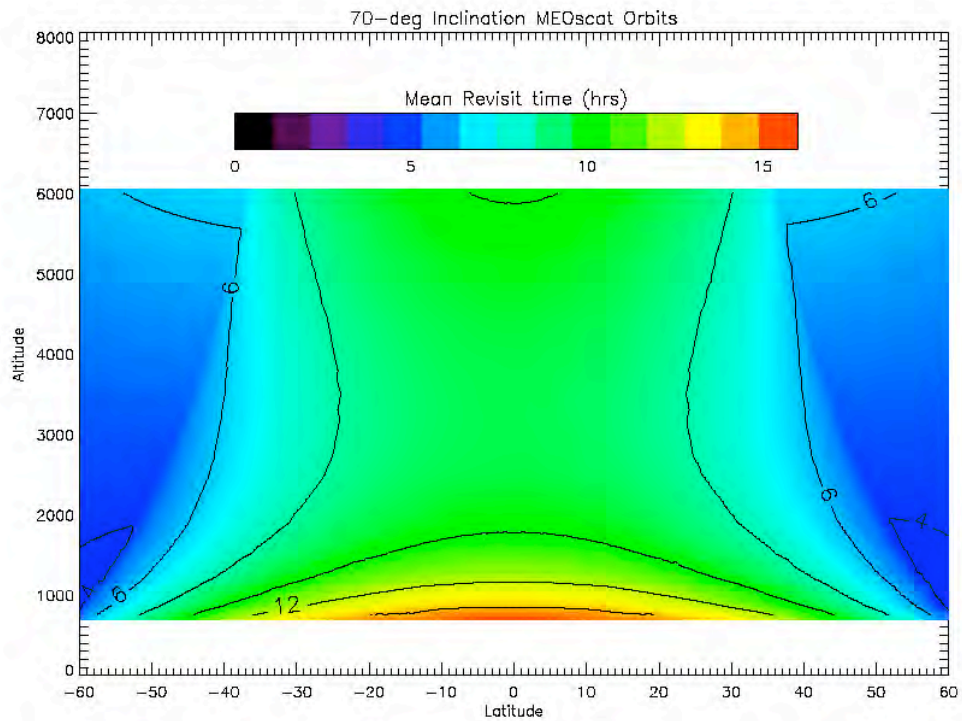


**Figure 4-16: Mean (top) and maximum (bottom) revisit times as a function of altitude (y-axis) and Earth latitude (x-axis) calculated for a single satellite in a circular, 70 deg inclination orbit.**

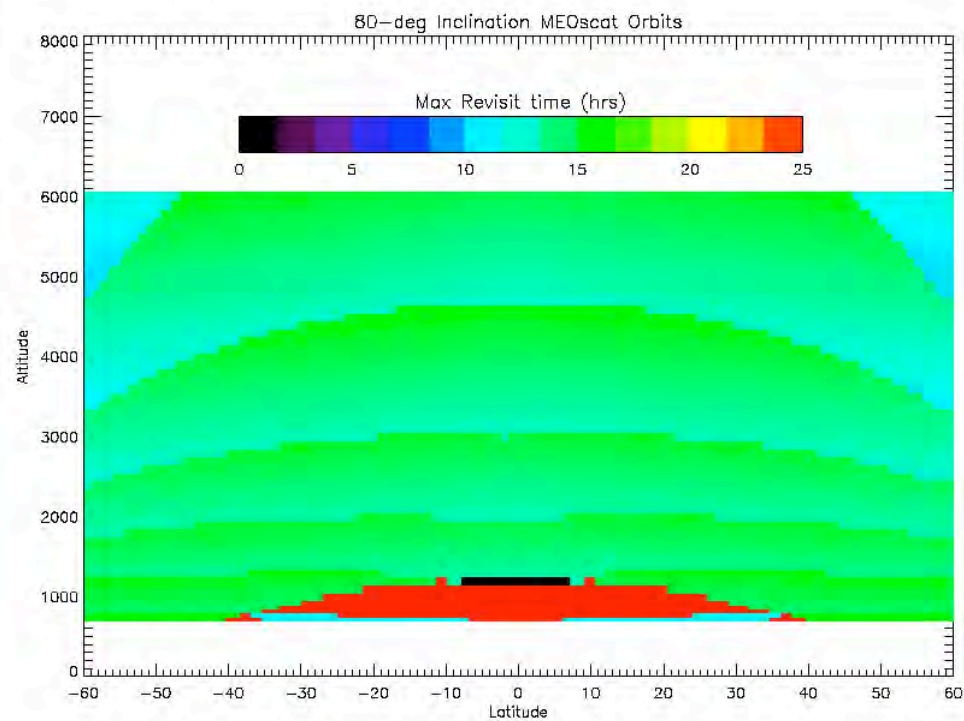
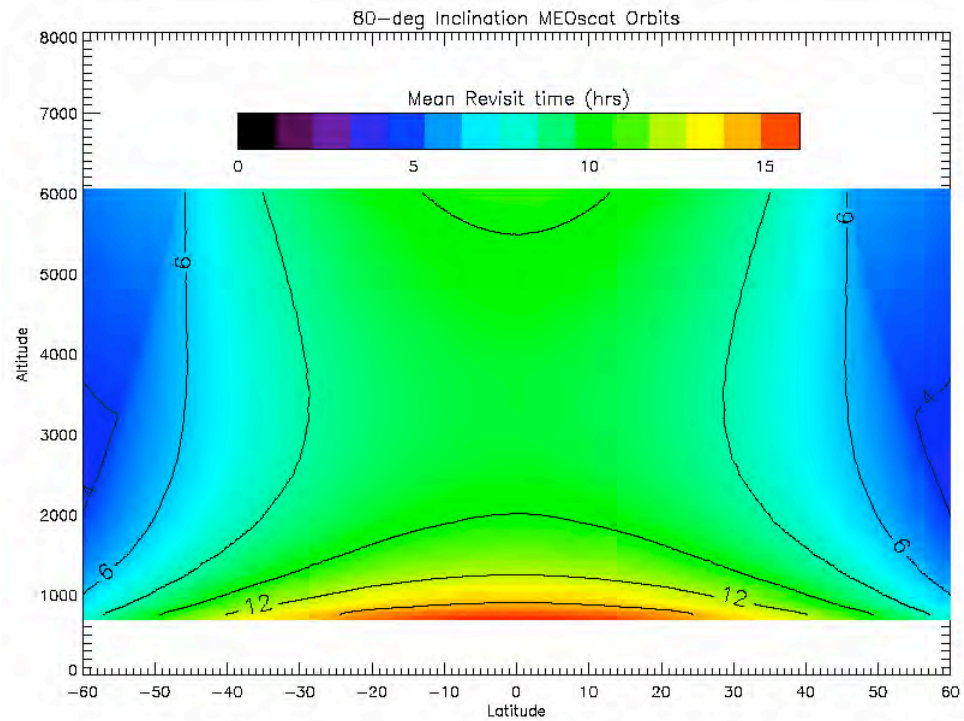


**Figure 4-17: Mean (top) and maximum (bottom) revisit times as a function of altitude (y-axis) and Earth latitude (x-axis) calculated for a single satellite in a circular, 80 deg inclination orbit.**

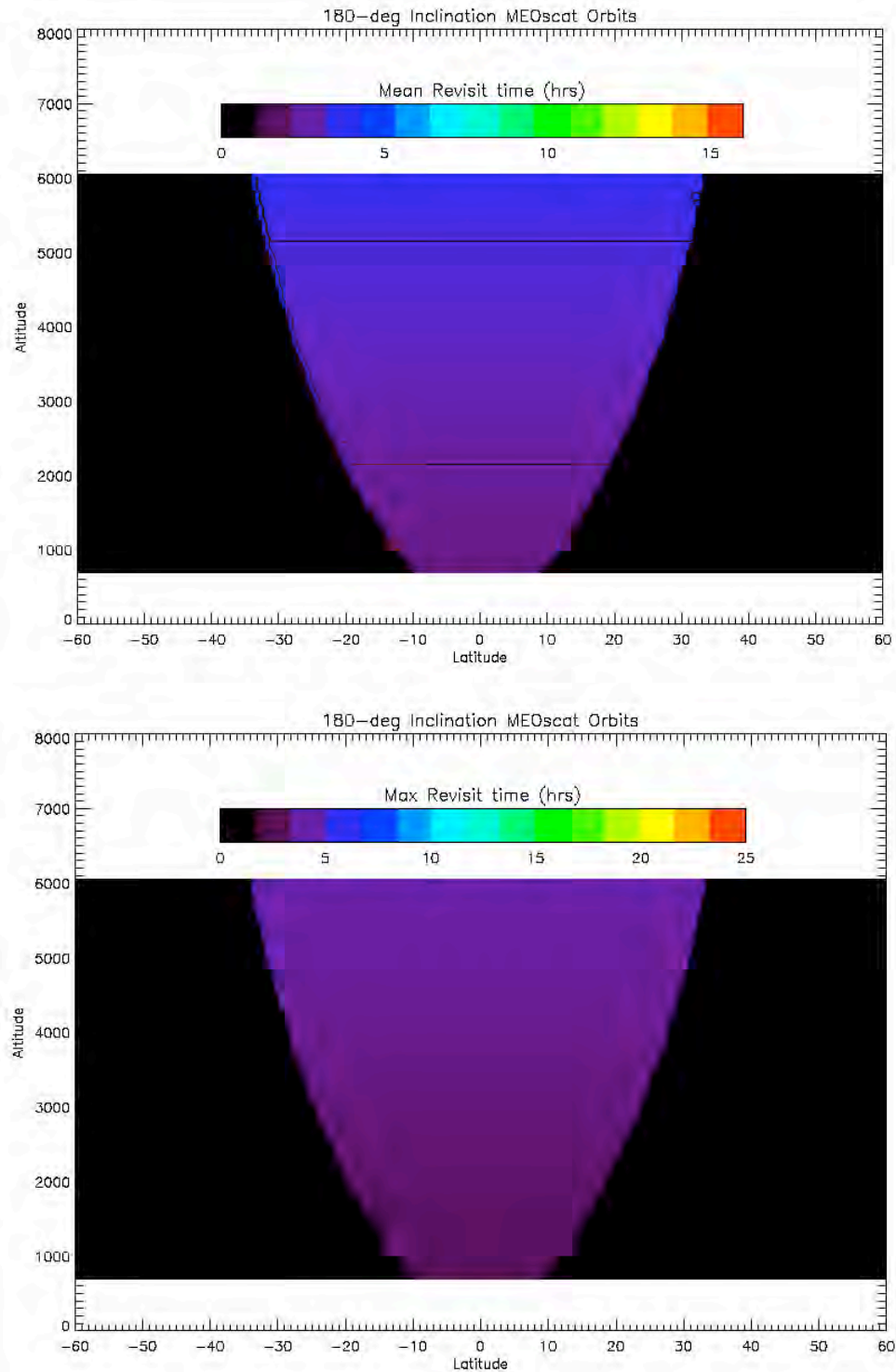


**Figure 4-18: Mean (top) and maximum (bottom) revisit times as a function of altitude (y-axis) and Earth latitude (x-axis) calculated for a single satellite in a circular, retrograde 180 deg inclination orbit.**



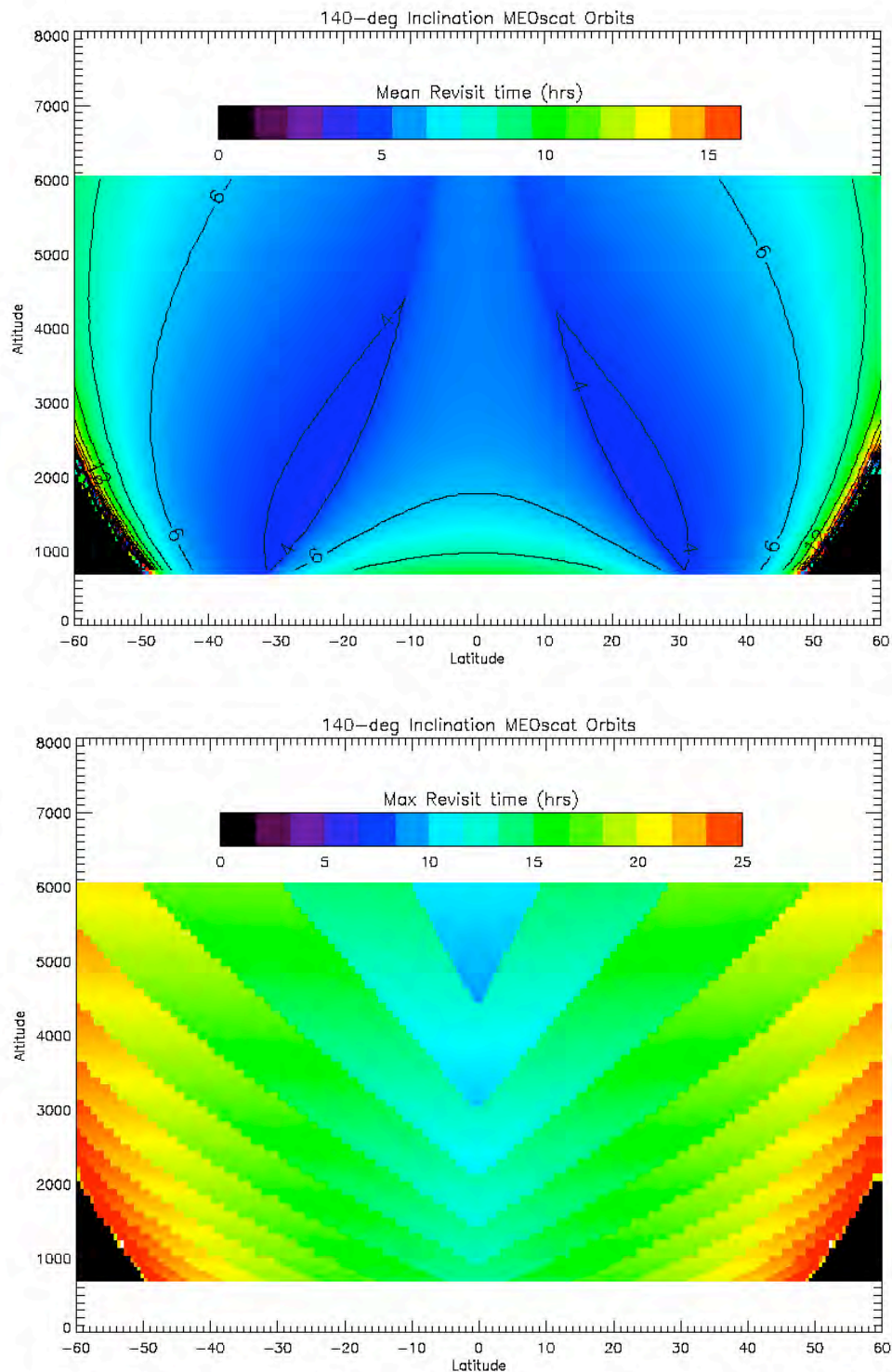


**Figure 4-19: Mean (top) and maximum (bottom) revisit times as a function of altitude (y-axis) and Earth latitude (x-axis) calculated for a single satellite in a circular, retrograde 140 deg inclination orbit.**

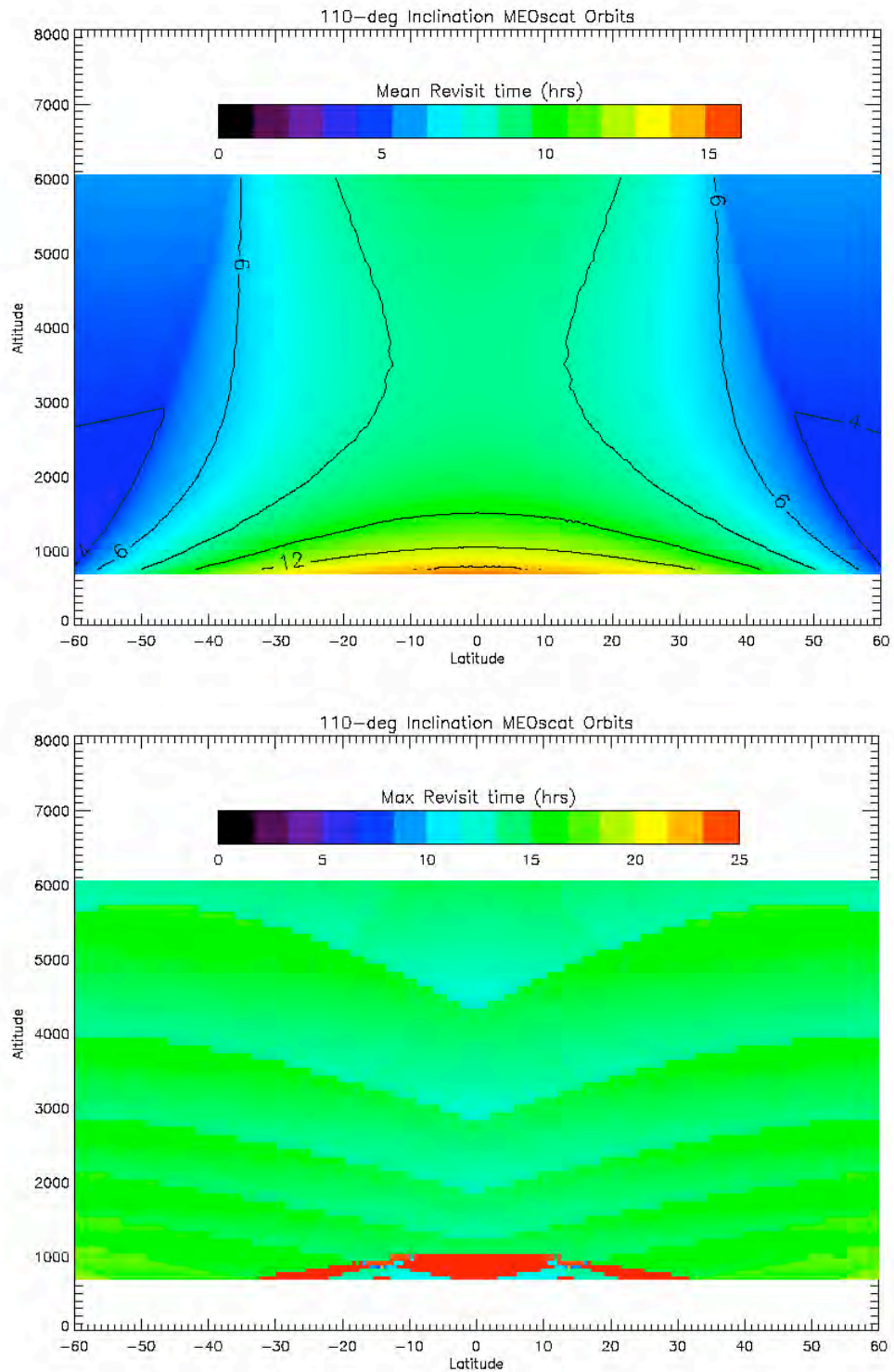


**Figure 4-20: Mean (top) and maximum (bottom) revisit times as a function of altitude (y-axis) and Earth latitude (x-axis) calculated for a single satellite in a circular, retrograde 110 deg inclination orbit.**

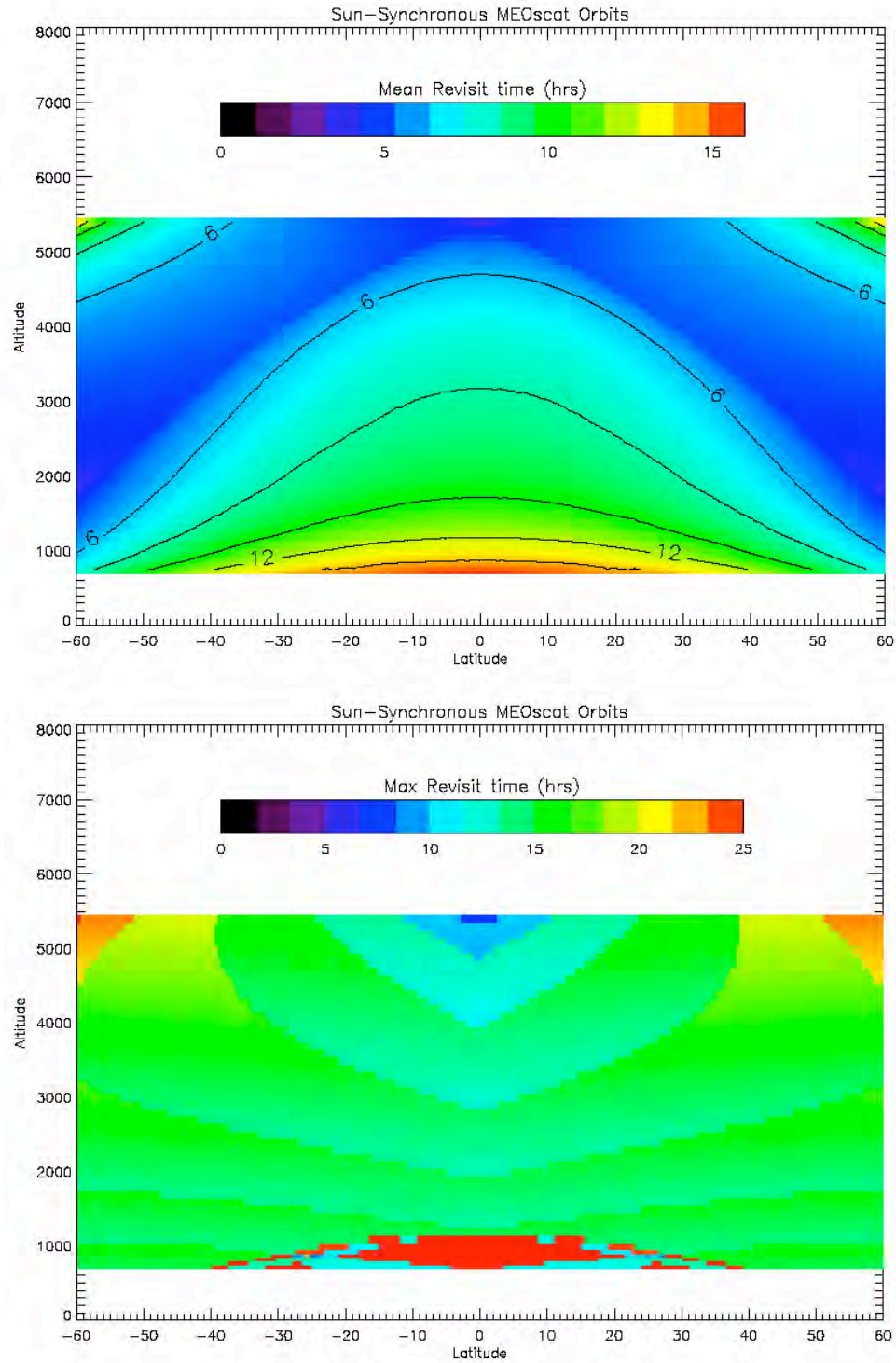


**Figure 4-21: Mean (top) and maximum (bottom) revisit times as a function of altitude (y-axis) and Earth latitude (x-axis) calculated for a single satellite in a near circular, sun-synchronous orbit.**



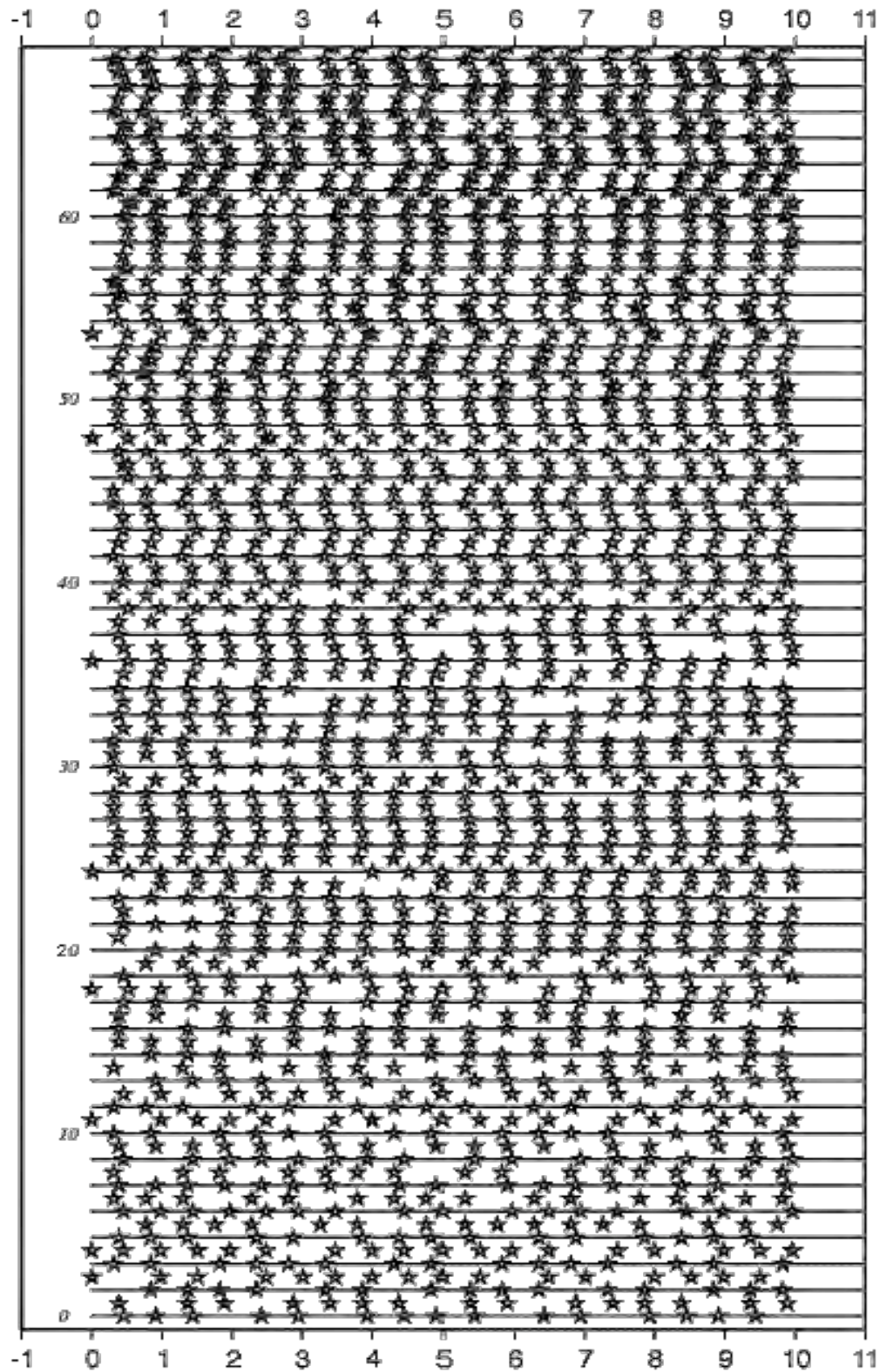


Figure 4-22: Time series of “hits” for 800 km, sun-synchronous orbit. Horizontal axis is in days. Each line on vertical axis represents a point in the SOAP grid with latitude shown. Stars represent times at which a given test point is imaged.



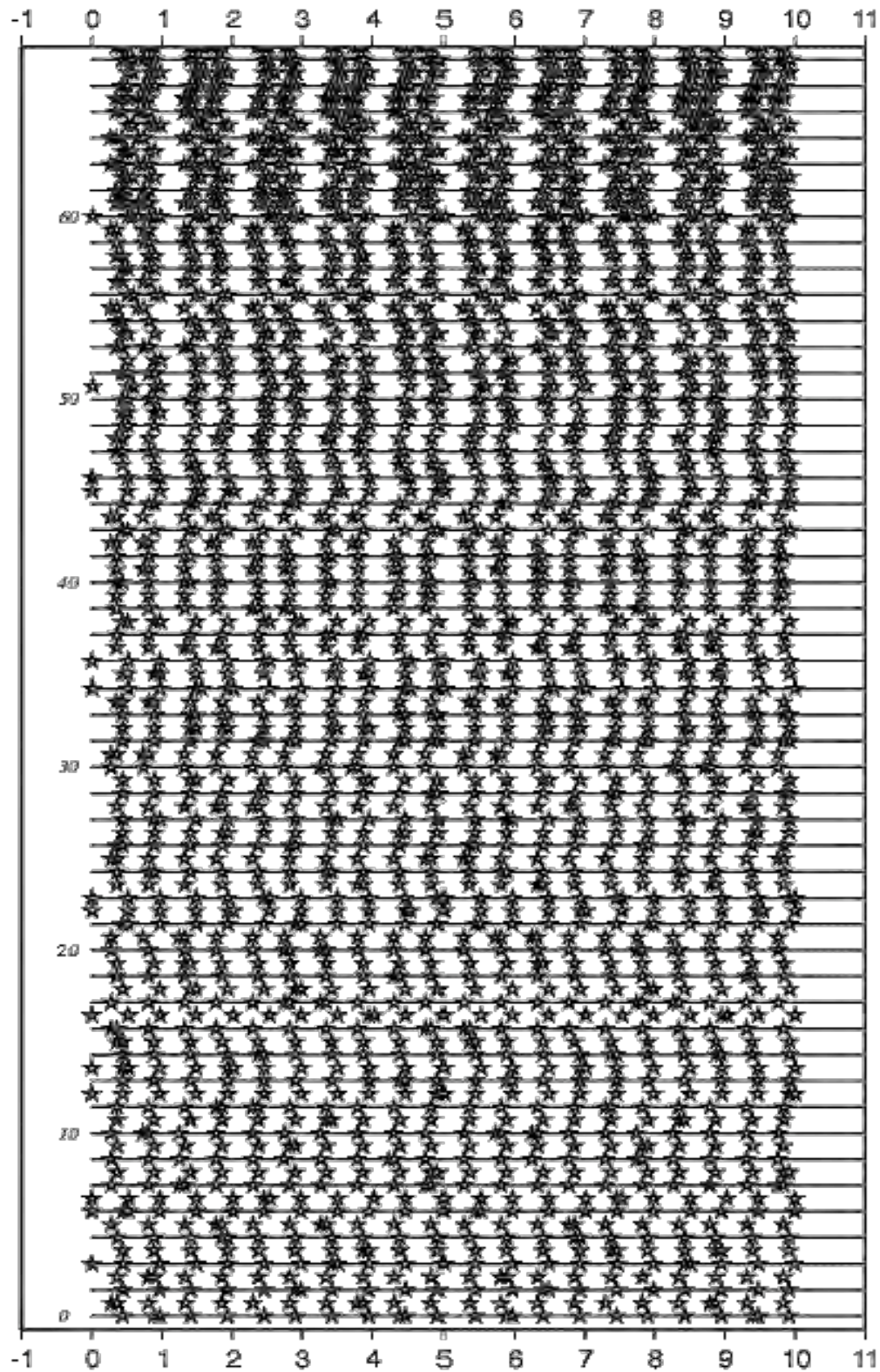


Figure 4-23: Time series of “hits” for 1500 km, sun-synchronous orbit. Horizontal axis is in days. Each line on vertical axis represents a point in the SOAP grid with latitude shown. Stars represent times at which a given test point is imaged.

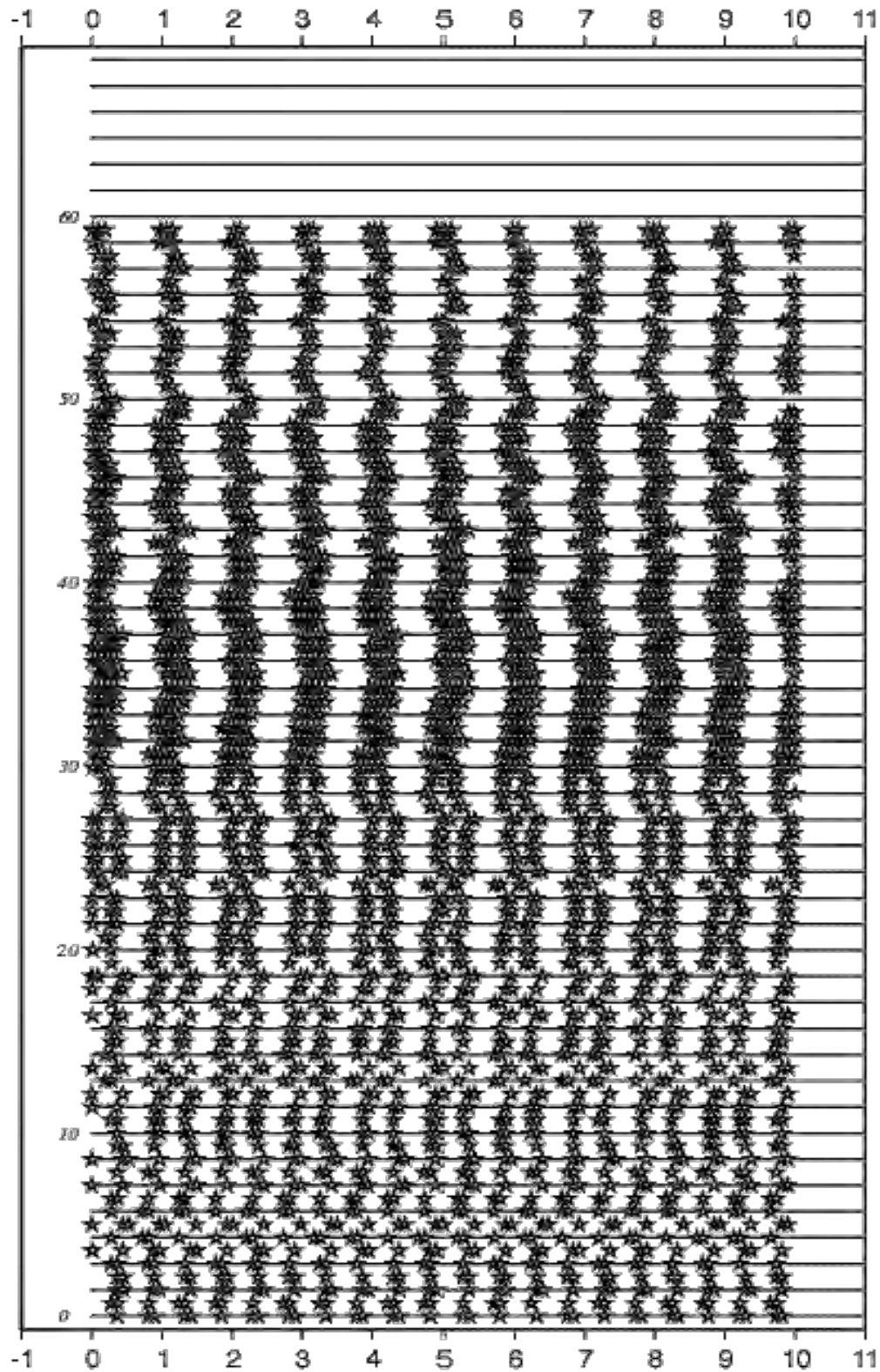
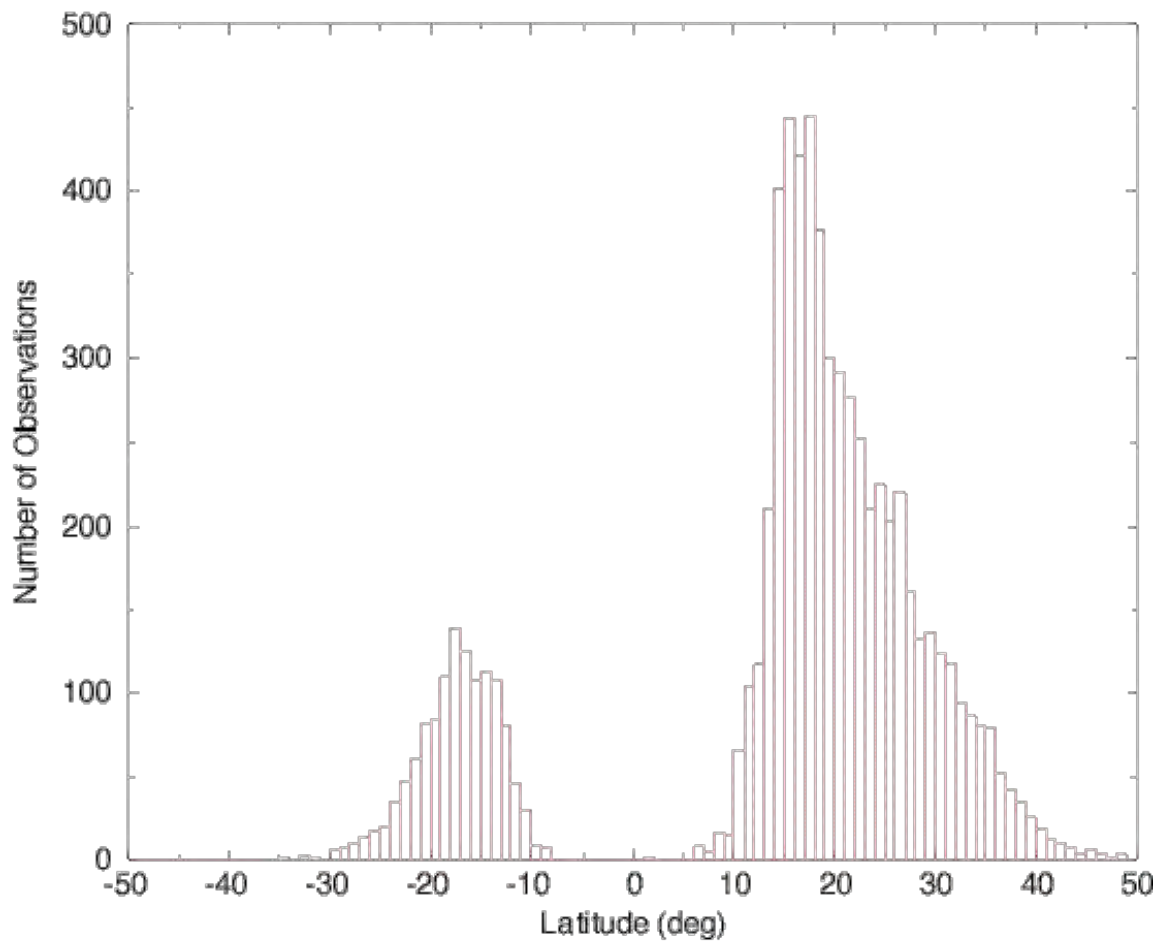
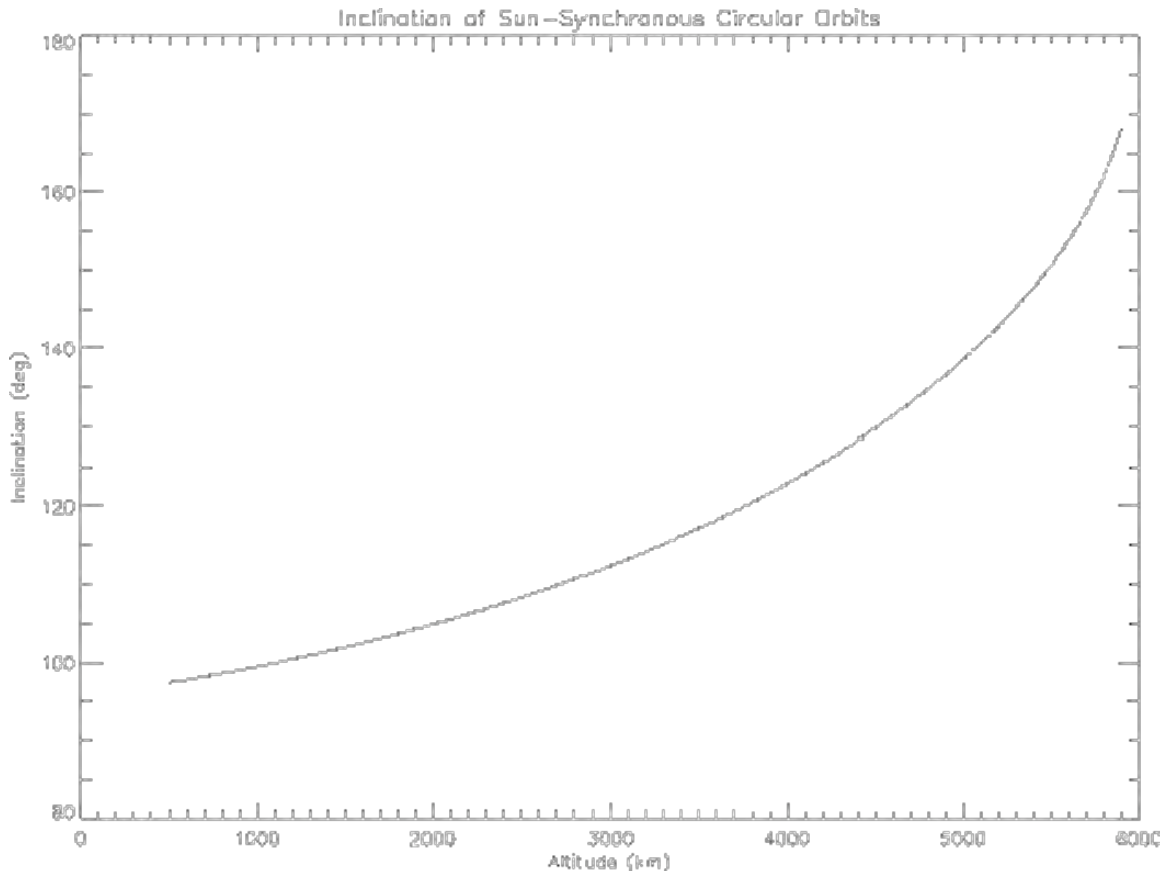


Figure 4-24: Time series of “hits” for 1500 km, 40 deg inclination orbit. Horizontal axis is in days. Each line on vertical axis represents a point in the SOAP grid with latitude shown. Stars represent times at which a given test point is imaged.

Hurricane Force Wind Observations vs. Latitude Over Last Five Years



**Figure 4-25: Histogram of latitude location of tropical storms with hurricane force winds for the years 1998-2003.**



**Figure 4-26: Sun-synchronous inclination as a function of orbit altitude.**

### **4.3 Multiple Spacecraft (Constellation) Coverage Results**

In addition to the single spacecraft case, it is also valuable to examine briefly the potential contributions to the revisit statistics if multiple spacecraft are considered. Two types of scatterometer constellations are considered: 1) Constellations that utilize a single MEOScat spacecraft and a single European ASCAT on a METOP spacecraft (anticipated to be operating during the same timeframe), and 2) Constellations that involve multiple MEOScat spacecraft.

#### **4.3.1 Single MEOScat Spacecraft Plus Single ASCAT on METOP**

The METOP spacecraft is planned to fly in an approximately 800-km sun-synchronous orbit, with an equator crossing time at 9:30 a.m. The ASCAT instrument is a fan-beam scatterometer that sweeps out two swaths on either side of the spacecraft ground track, with a “nadir gap” region in between where no wind measurements are made. The two swaths are each 550 km wide, and the nadir gap is 660 km wide.



In Figure 4-27, the SOAP tool has been used to plot the average revisit time as a function of latitude for three cases: 1) a single ASCAT only, 2) a single MEOScat system operating in a sun-synchronous orbit at 1500 km, and 3) the combination of these two systems. Note that the average revisit time of ASCAT is approximately three times greater than that of MEOScat. This is due to the fact that the total ASCAT swath (1100 km) is approximately a factor of three less than the MEOScat swath (3400 km). Note that when the ASCAT coverage is included, there is more than a three-hour improvement in the average revisit time at the equator, improving the MEOScat-only statistics from 10 hours to 8 hours. The additional ASCAT samples, however, occur randomly, so the maximum revisit time is unchanged from that described in Section 4.2. Another issue that may diminish the usefulness of the additional ASCAT data is the fact that “merging” data from the two different sensors may prove difficult.

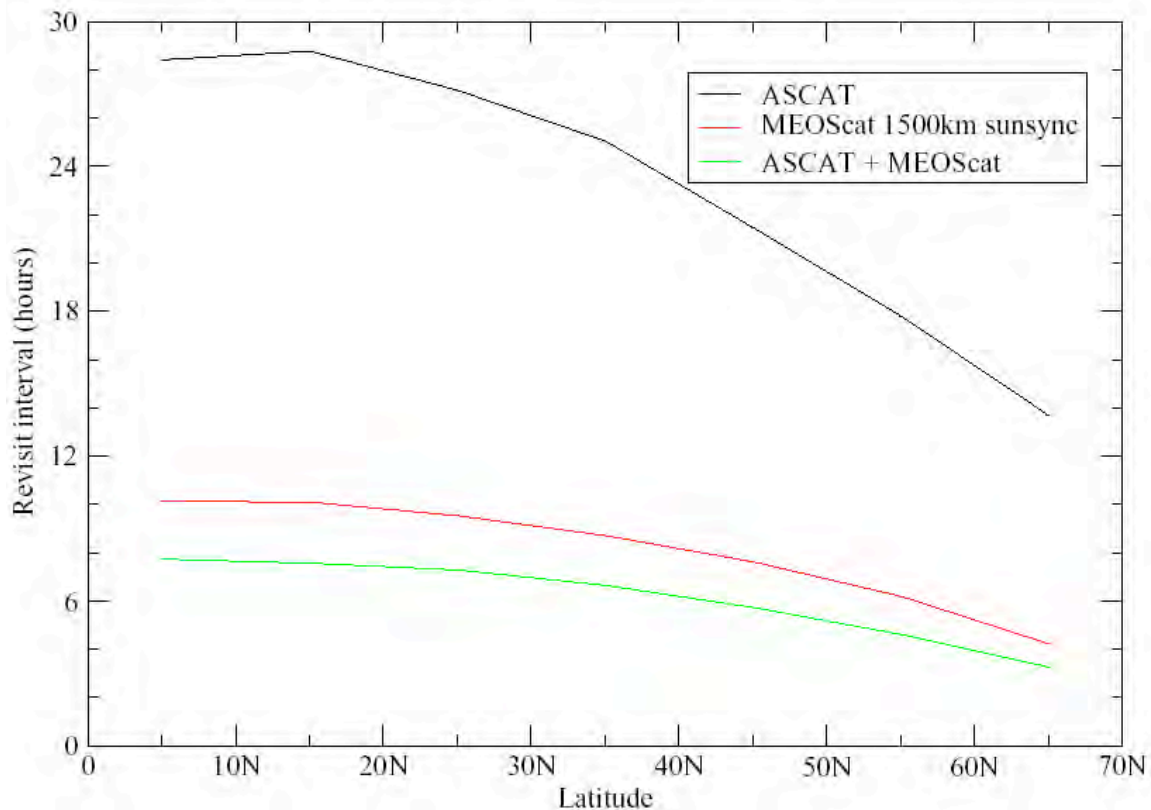


**Figure 4-27: Average revisit time vs. latitude for ASCAT only, a conically scanning MEOScat in a 1500-km sun-synchronous orbit, and the combined statistics of the two sensors.**

### 4.3.2 Multiple MEO Sensors

As discussed in Section 1, in order to consistently and completely resolve the diurnal cycle, a regular revisit time of 6 hours is desired. As concluded in Section 4.2.3, such regular 6-hour sampling cannot be achieved globally with a single spacecraft, and

therefore a constellation must be employed. An exhaustive analysis of constellation options is beyond the scope of the present analysis. The previous single satellite analysis, however, does suggest some promising constellation concepts. Because orbits at 1500 km leave no gaps between successive swaths, a single satellite is guaranteed to have a maximum revisit time of approximately 12 hours or less. This suggests that a constellation of two satellites at 1500 km could achieve regular revisit times of 6 hours or less. In Figure 4-28, the coverage statistics for a two-satellite, 1500 km sun-synchronous constellation is shown. The orbit planes of the two satellites are placed  $90^\circ$  apart in longitude. Note that, as expected, the maximum revisit time is between 6 and 8 hours globally, ensuring regular sampling near the desired 6 hours. In Figure 4-29, the combined “hit plot” exhibiting the approximately 6 hourly sampling for this case is shown.

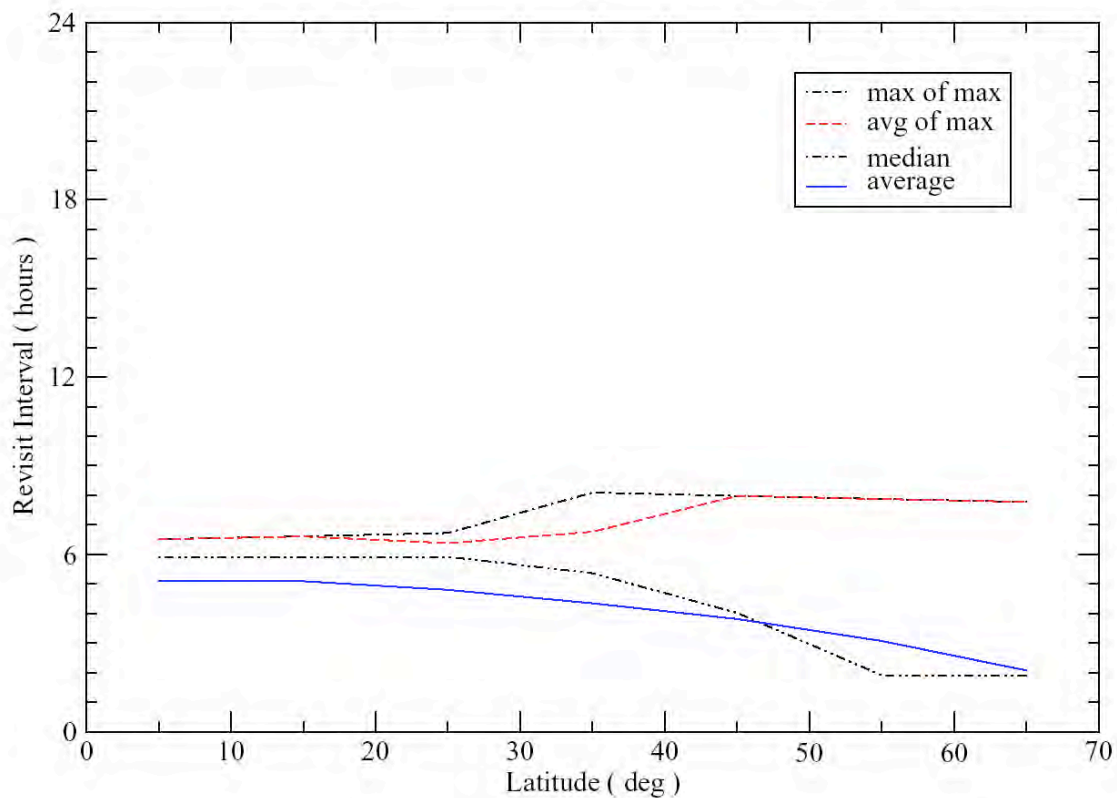


**Figure 4-28: Revisit statistics for a constellation of two scatterometers in 1500 km sun-synchronous orbits. The satellites planes are positioned  $90^\circ$  apart.**

The “burst” revisit statistics exhibited by sensors placed in a medium inclination orbit (i.e.,  $40^\circ$ – $50^\circ$  inclination) suggest an interesting possibility for a MEOScat constellation. If the orbits of the sensors can be placed in such a fashion that the bursts from two platforms form a continuous series, then the revisit time could improve significantly beyond even 3 hours. In Figures 4-30 and 4-31, such a constellation is considered. In Figure 4-30, the hit plot for two sensors placed in 1500 km,  $40^\circ$  inclination orbits is shown. In this case, the orbital planes of the two satellites are placed  $90^\circ$  apart in

longitude. Here, for clarity, the hits associated with the second sensor have been colored red. Note that at low latitudes, the revisit intervals are somewhat less than the sun-synchronous case, with the maximum revisit time still approximately 6 hours. At mid-latitudes, however, the desired effect has not been achieved. Here the bursts from the individual sensors overlap, and large (nearly 12-hour) gaps occur. On the whole, this constellation is not significantly better than the sun-synchronous case at low latitudes, and perhaps somewhat worse at mid and high latitudes.

In Figure 4-31, the satellites are instead phased  $180^\circ$  apart in longitude. In this case, the desired effect is achieved at mid-latitudes, with very dense collections of revisit events occurring. Here, points between  $30^\circ$  and  $50^\circ$  latitude are revisited regularly at the orbital period (roughly every 2 hours), with occasional approximately 6-hour gaps. Regular sampling at lower latitudes, however, is a rather consistent 12 hours. This constellation would be a useful one to emphasize mid-latitudes, at the expense of revisit time at low latitudes and coverage at high latitudes (relative to the sun-synchronous case).



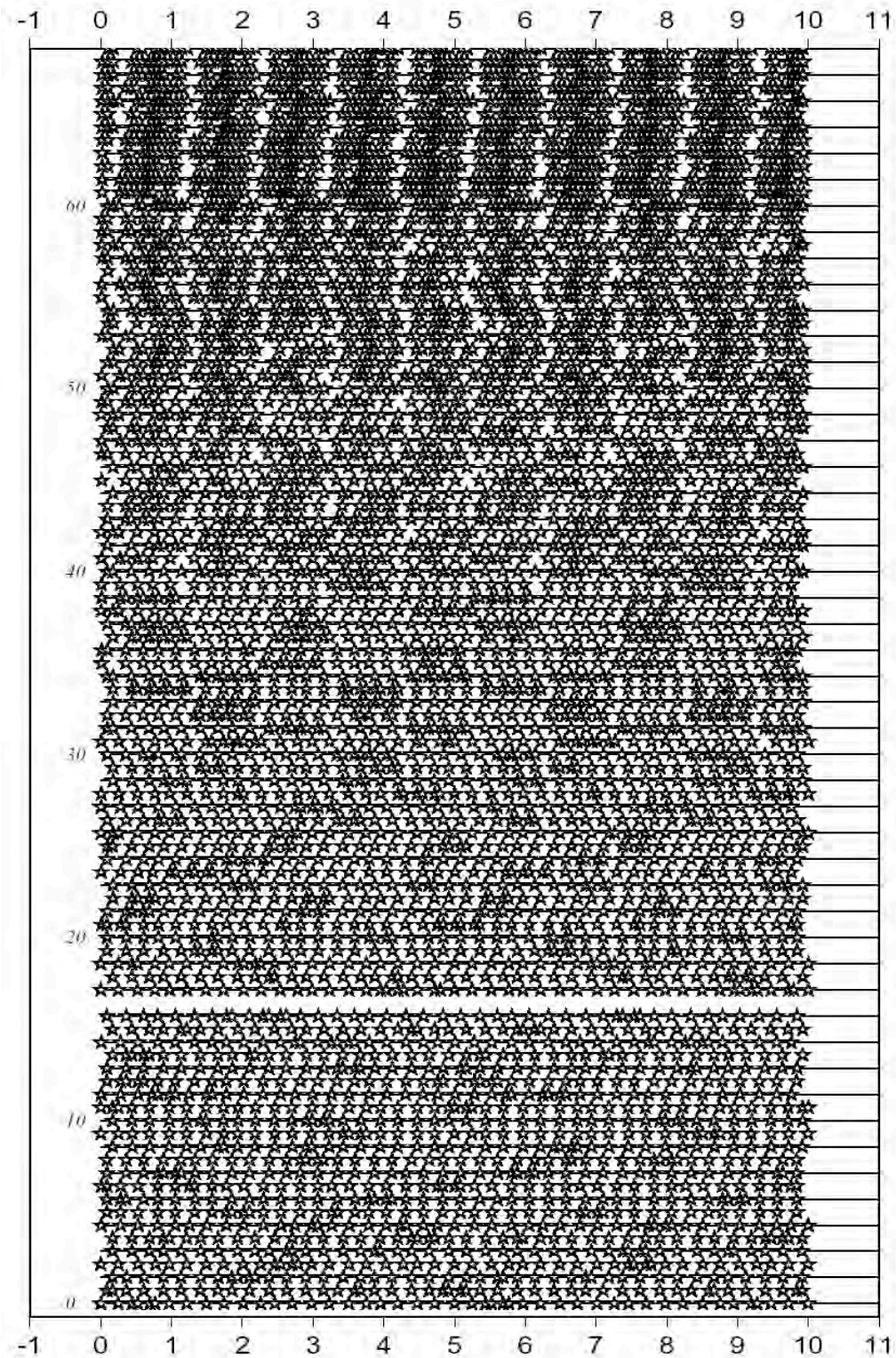


**Figure 4-29: Time series of "hits" plot for a constellation of two scatterometers in 1500 km sun-synchronous orbits. The satellites' planes are positioned 90° apart. Horizontal axis is in days. Each line on vertical axis represents a point in the SOAP "coarse grid," with latitude also indicated.**



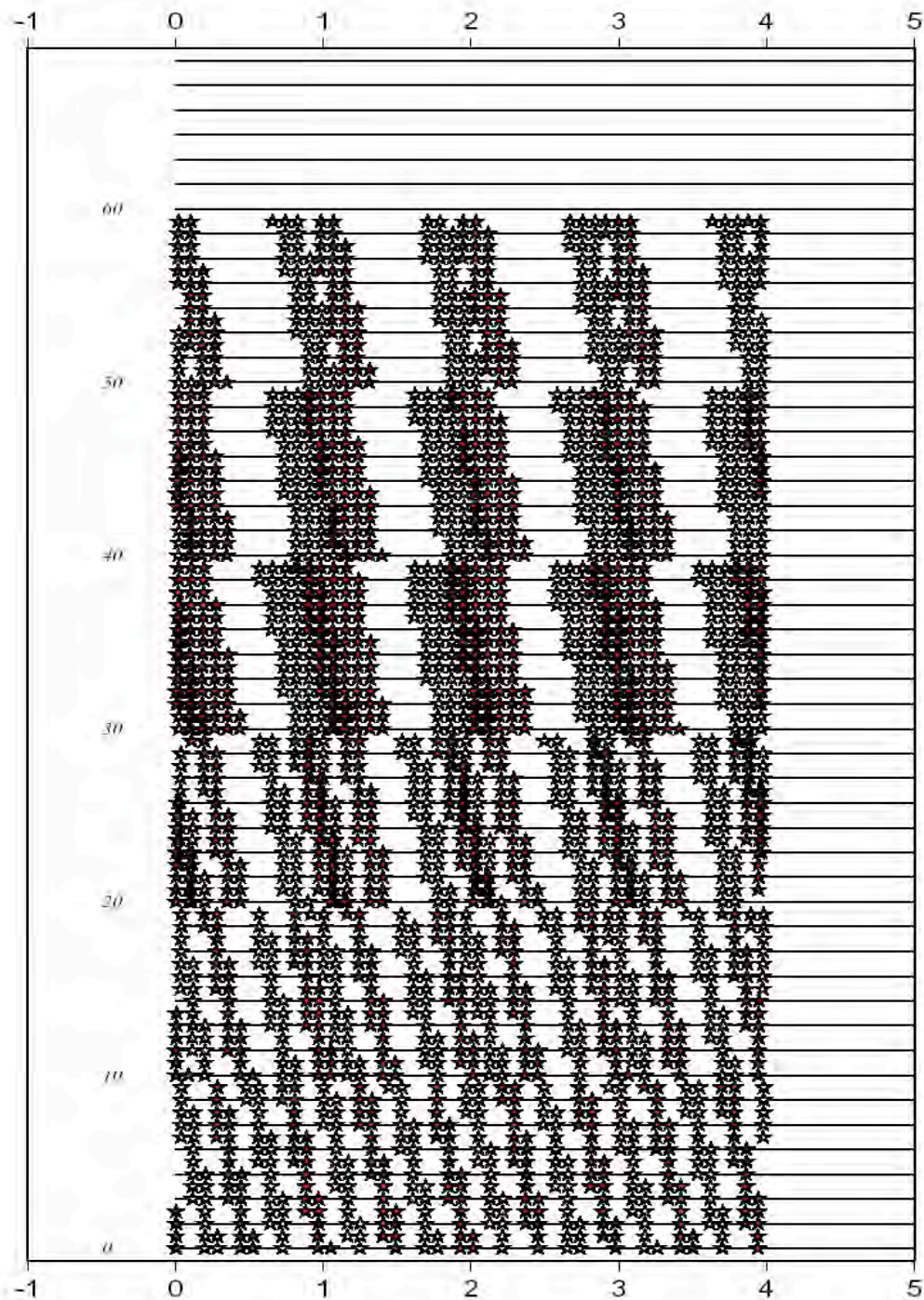


Figure 4-30: Time series of “hits” plot for a constellation of two scatterometers in 1500 km 40° inclination orbits with the satellites’ planes positioned 90° apart. In this case, the “hits” from the second satellite are shown in red. Horizontal axis is in days. Each line on vertical axis represents a point in the SOAP “coarse grid,” with latitude also indicated.

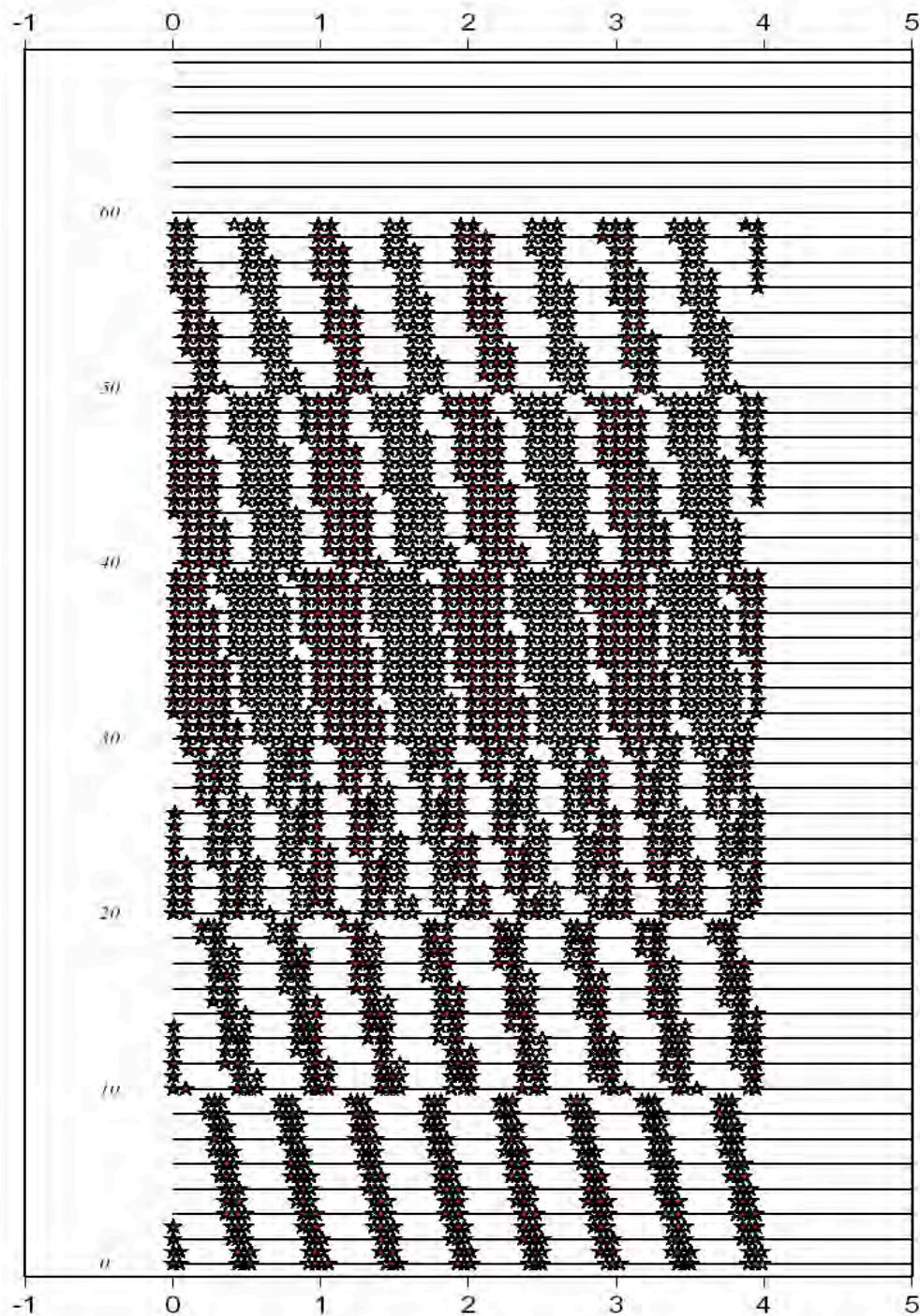


Figure 4-31: Time series of “hits” plot for a constellation of two scatterometers in 1500 km 40° inclination orbits with the satellites’ planes positioned 180° apart. In this case, the “hits” from the second satellite are shown in red. Horizontal axis is in days. Each line on vertical axis represents a point in the SOAP “coarse grid,” with latitude also indicated.

#### **4.4 Radiation Considerations**

A final, but important, consideration in evaluating the orbit trade-offs is the radiation environment encountered. The definition of “Medium Earth Orbits” or “MEO” is a subjective one. In a very broad sense, MEO can be considered to be all altitudes from 1000 km to 40000 km. This range encompasses a wide range of different radiation environments – some comparable to that encountered in LEO, and some dramatically more severe. In this section a survey of the radiation environments in the 1000 – 10000 km altitude range (the MEO range likely to be utilized by a future scatterometer) is performed. General conclusions about the difficulty of flying a scatterometer in these different environments are briefly discussed.

Figure 4-32 shows the yearly Total Ionizing Dose (TID) at the center of a 5 mm radius, solid aluminum spherical shield for one year. The Log10 of the TID in rads is plotted. As suggested by the jaggedness of some of the contour lines, the resolution is only sufficient to convey gross features. The radiation estimates were derived from environment models and shielding transport code that are implemented on the ESA-funded website <http://www.spennis.oma.be/spennis/>. The trapped radiation environment is estimated from the AP8 and AE8 models (J. I. Vette, NASA GSFC), which provide the flux along a satellite trajectory as averaged over six months or more. The models each provide an estimate for a time period during solar sunspot maximum conditions, and for a time period during solar sunspot minimum conditions. The conditions used for this estimate, sunspot maximum for electrons (AE8max) and sunspot minimum for protons (AP8min), were chosen to give the largest contribution from each. This is ostensibly a non-physical condition, but provides an upper bound on actual radiation as estimated by the models, regardless of solar cycle phase.



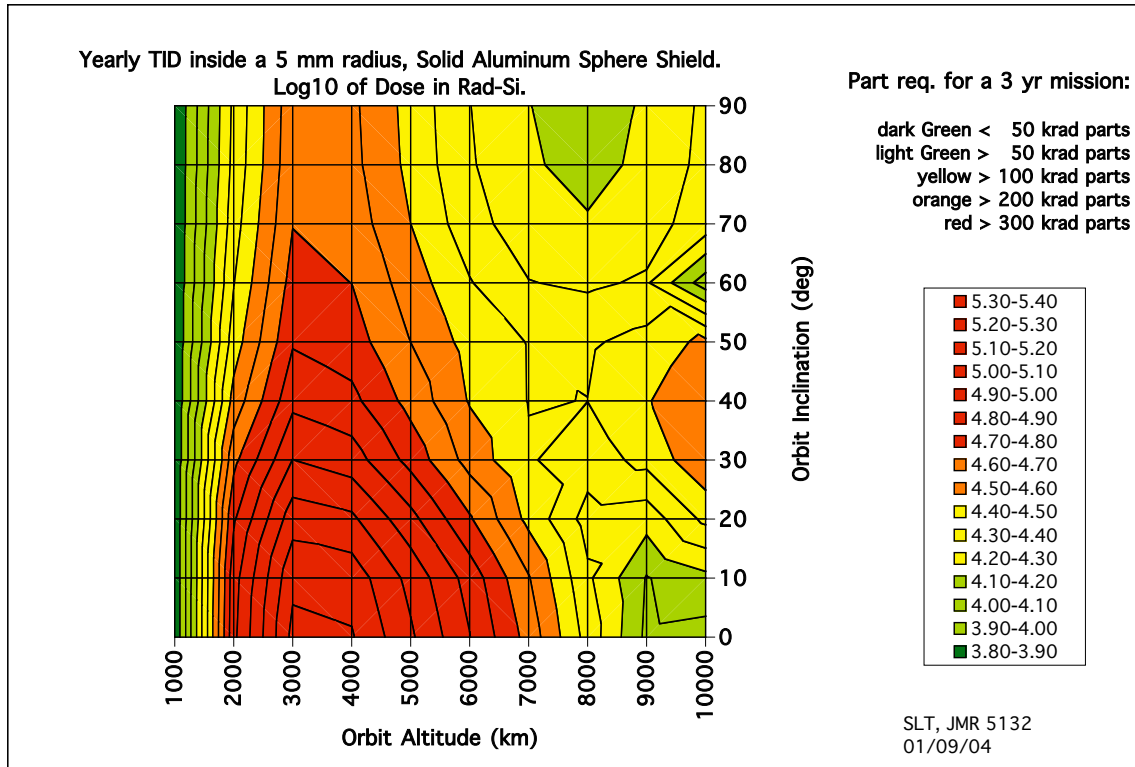


**Figure 4-32: Summary of radiation environment as a function of altitude and inclination. Contour plot on the left indicates log<sub>10</sub> TID per year through 5mm of Al for different orbits. Color codes indicate total TID tolerance required for parts assuming a 3-year mission and RDF = 2.**

The TID estimate considers only Earth's trapped electron and trapped proton radiation, which are the only significant contributors to the cumulative radiation exposure. The largest of the other contributing radiation environments is solar energetic protons, but they provide about 6 krad-Si to the orbits having the highest altitude and inclination, and only about 0.4 krad-Si to a 1000 km, polar orbit (which is about 25% of the TID from trapped radiation in that orbit).

The radiation transport calculation uses the "Shieldose2" code (S. M. Seltzer, NIST). The chosen shield geometry, a solid sphere, provides an upper bound estimate for any shield geometry having a uniform shield thickness. No radiation design factor (RDF) has been applied to the radiation environment. An RDF (i.e., a multiplicative factor greater than unity) is typically applied to the environment to derive the radiation requirement for the radiation tolerance of electronics parts. This will be discussed below.

The dose levels are plotted as a simple color contour plot consisting of green, yellow, orange, and red levels. The color boundaries are set by the radiation-tolerance requirement for parts, for a 3-year mission. It is assumed that electronic parts are required to tolerate at least twice the design environment, i.e. that the Radiation Design Factor

equal two ( $RDF = 2$ ). Four levels of part tolerance are shown: 50, 100, 200, and 300 krad. These are typical levels at which guaranteed radiation-tolerant parts can be acquired. Again, the color contours show the orbit regions that require a given part tolerance for a 3-year mission.

The color scheme is chosen in order to convey the relative degree of severity of these environments. These level designations were developed to guide the high-level MEOScat trade-off studies in which different altitudes are being considered. In a subjective, qualitative sense, the colors represent the extent to which radiation will be a technological and/or budgetary challenge to a new mission. “Green” is intended to represent a level that is most straightforward to handle, with parts that are fairly easy and inexpensive to acquire, and which require only moderate amounts of shielding. Light green, shading to yellow and then orange, indicates missions that require progressively more detailed and potentially costly part selection and radiation analysis, with the possibility that subsystem performance will be compromised by the unavailability of radiation-tolerant versions of necessary part types (or the inability to provide sufficient shield mass to protect them). “Red” suggests a regime in which the radiation environment is a major obstacle to achieving a satellite design that will attain mission goals.

## 5. MEOScat System Design Parameter Trade-Offs

### 5.1 Antenna/Altitude Trade-off Study

Perhaps the most important variable influencing radar design and performance is the altitude chosen for the scatterometer orbit. In this section, we examine many of the scatterometer radar characteristics as a function of altitude. Although we perform this system trade-off study for a conically scanning, pencil-beam scatterometer, much of this analysis is applicable to other scatterometer architectures.

Most of the following analysis is based on the study of (Spencer, et al. 2003) and the equations contained therein. Henceforth, we refer to this key reference as Sp03.

#### 5.1.1 System Geometry and Real-Aperture Resolution

The independent variables that we assume in this study include the spacecraft altitude,  $h$ , the radar wavelength,  $\lambda$ , and the desired incidence angle of the radar beam at the Earth's surface,  $\theta_i$ . Also independent are either the approximate desired footprint size in elevation (i.e., radially from subsatellite point),  $f_{el}$ , and azimuth (direction orthogonal to the radius vector),  $f_{az}$ , or the approximate desired antenna width in elevation,  $d_{el}$ , and azimuth,  $d_{az}$ . Given a desired footprint size, the antenna width (in azimuth) is approximately

$$d_{az} = \xi_{az} \lambda / \beta_{az} = \xi_{az} \lambda / (f_{az} / \rho) = \xi_{az} \lambda \rho / f_{az} \quad (5.1)$$

where  $\beta_{az}$  is the 3 dB *two-way* beam width, and  $\xi_{az}$  is an aperture scaling factor (we use a value appropriate for a circular aperture and a round trip 3-dB beam,  $\xi_{az} = 1.2/\sqrt{2}$ ). The look angle,  $\theta_l$ , and slant range,  $\rho$ , are computed by

$$\sin(\theta_l) = \frac{R}{R+h} \sin(\theta_i), \quad \rho = (R+h) \cos(\theta_l) - R \cos(\theta_i) \quad (5.2)$$

where  $R$  is the radius of the Earth (we assume a spherical Earth). (Refer to Figure 5-1 for an illustration of many of the parameters.)

Figures 5-2, *a* and *b*, show the approximate antenna width required to generate a footprint size of either 25 km or 10 km. The former footprint corresponds to the ground resolution of existing, real-aperture, scatterometer systems, while the latter represents a significant improvement over existing systems. In both cases, ground resolution is directly proportional and approximately equal to footprint size. A range of altitudes from 500 km to more than 6000 km is examined, and two end-member ground incidence angles, 45° and 60°, are studied. Note that existing scatterometer systems orbit below 1000 km. Results are shown for two frequencies, Ku-band (14 GHz, 2 cm wavelength), and C-band (5.3 GHz, 6 cm wavelength), for which existing scatterometers have successfully determined ocean wind vectors and appropriate model functions. Since antenna width varies linearly with wavelength, results for X-band (9.6 GHz, 3 cm wavelength) would lie between the two cases shown.

For Ku-band, 1–3 m diameter antennas for low-Earth orbits (<1000 km) quickly grow to more than 10 m diameter for MEO (medium Earth orbits) and a 10 km footprint. Note that a larger antenna is needed for the outer beam if both inner and outer beams are to have the same ground footprint width or, alternatively, given the same antenna dimensions, ground resolution is slightly better for the inner beam than the outer, since the inner beam has a closer “target.”

For a C-band system, the antenna is about 3 times larger for the same altitude and footprint size, resulting in LEO antennas 2–8 m in diameter, and MEO antennas up to 40 m in size.

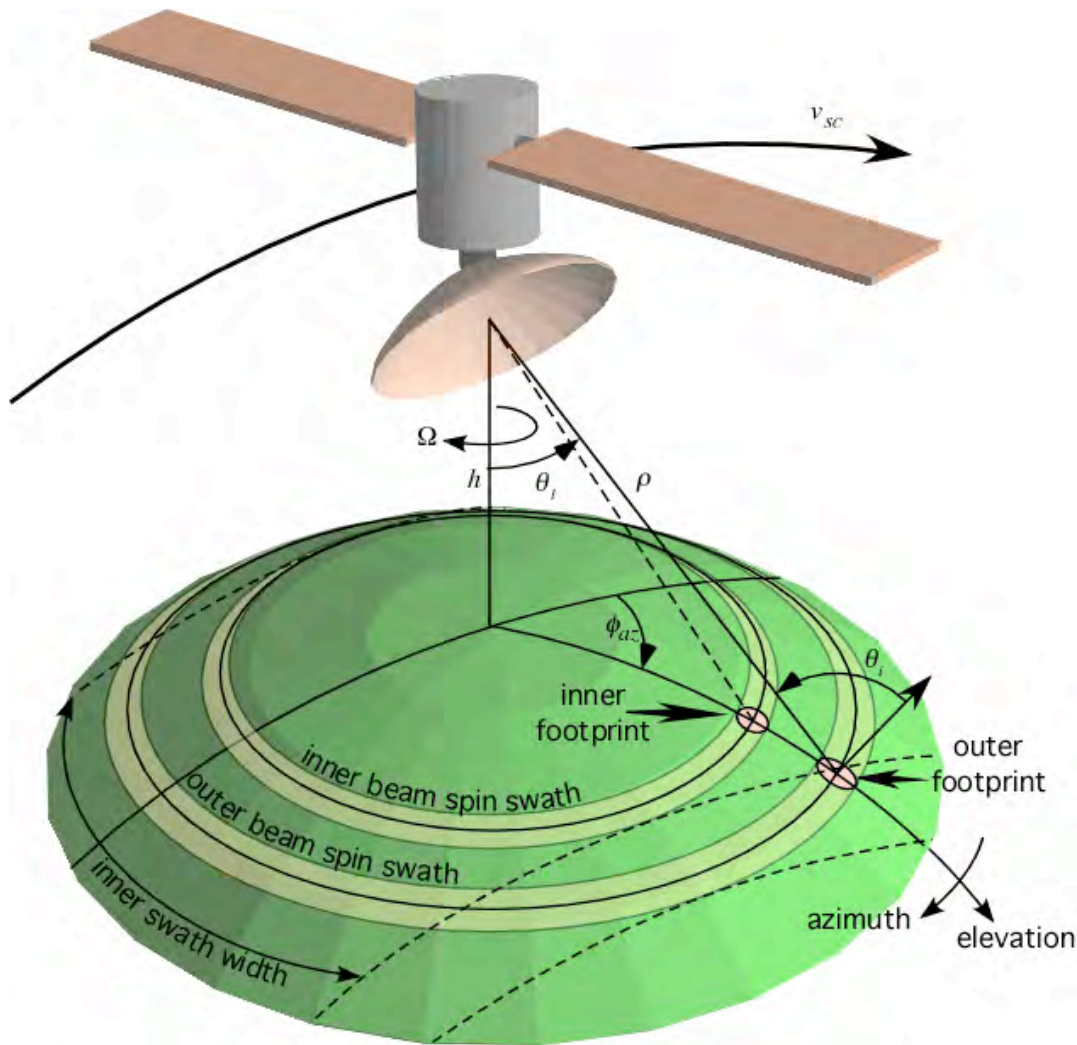


**Figure 5-1: Illustration of flight geometry and parameter definitions for a rotating pencil-beam configuration.**

For a circular beam, in the elevation or range direction the footprint size is elongated relative to the azimuth footprint size by a factor of  $1/\cos(\theta_i)$ . Since range resolution is

not limited by the geometry but rather by bandwidth and signal processing, the size of the elevation footprint is most relevant for antenna rotation, discussed below.

The results shown in Figure 5-2 apply as well for the azimuth component of the footprint of alternative scatterometer architectures. For example, the figure indicates the approximate length required for a real-aperture stick scatterometer antenna.

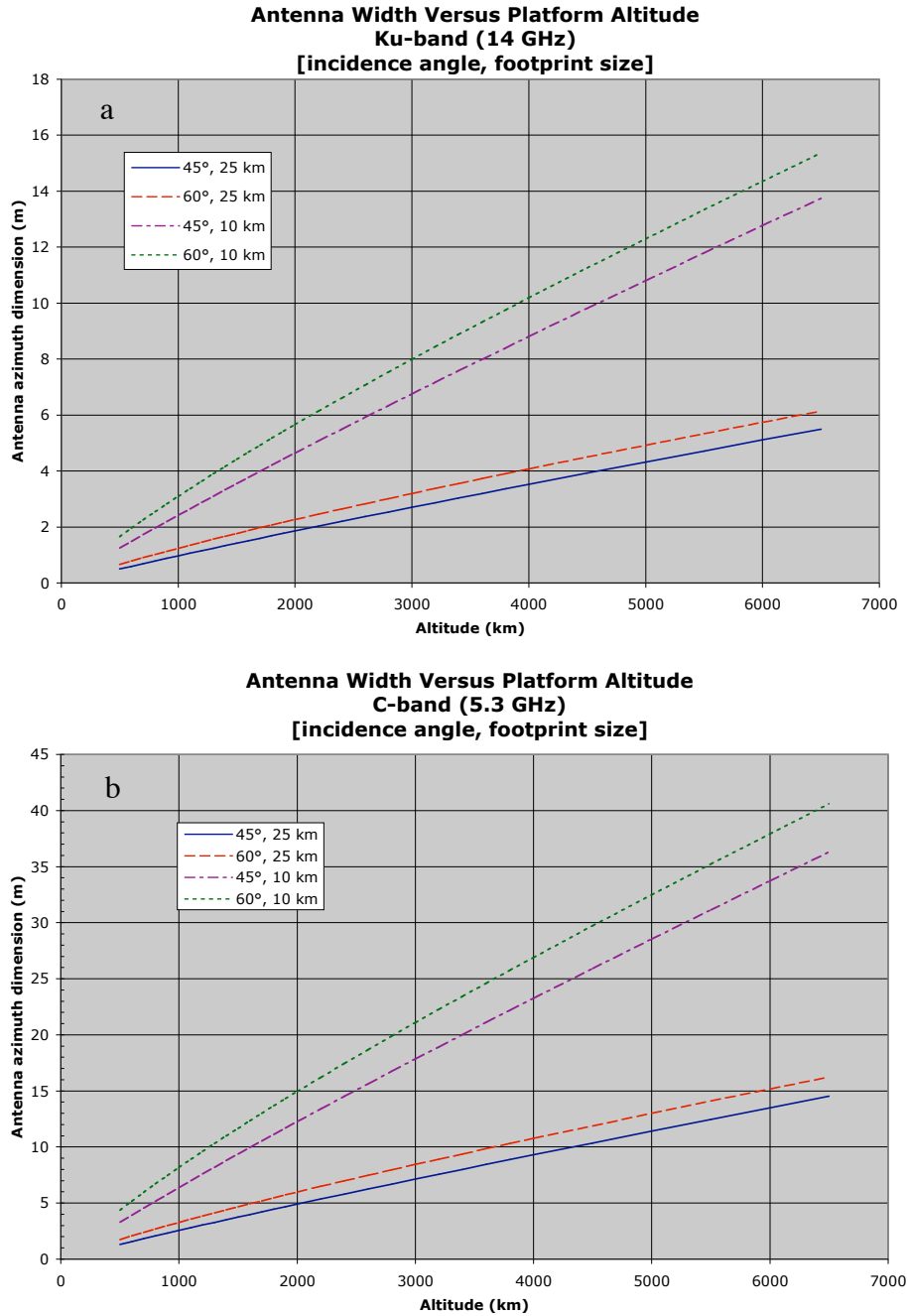


**Figure 5-2a and b. Antenna width versus platform height for real-aperture, Ku- and C-band scatterometer systems. Results are shown for two azimuth footprint sizes, and two ground incidence angles.**



### 5.1.2 Ambiguity Constraints and SAR Processing

Given a rotating, pencil-beam antenna configuration, Doppler-range processing can yield higher effective ground resolutions during a large portion of the circular scan. The scatterometer becomes essentially a low-resolution, unfocussed synthetic aperture radar (SAR) sensor with a continually varying squint angle. To perform SAR processing, both range and azimuth ambiguities must be avoided, as described more fully in Sp03.

To avoid range ambiguities while using the entire elevation footprint, the pulse repetition interval (PRI) must be greater than the elevation footprint, converted to two-way time delay. To avoid Doppler ambiguities while using the entire azimuth footprint, the pulse repetition frequency (PRF) must be greater than the spread in Doppler frequency over the azimuth footprint. These constraints are represented by

$$\begin{aligned} a\chi_{\text{delay}} &= 2af_{\text{el}} \sin\theta_i / c \leq \text{PRI} = 1/\text{PRF} \\ b\chi_{\text{Dopp}} &= 2bf_{\text{az}} v_{\text{sc}} \sin\phi / \rho\lambda \leq \text{PRF} \end{aligned} \quad (5.3)$$

where  $a$  and  $b$  represent ratios of footprint buffer to footprint sizes (defined fully in Sp03),  $v_{\text{sc}}$  is the spacecraft platform velocity, and  $c$  is the velocity of light. (Earth rotation is ignored in Eq. 5.3.) Combining these two equations, and inserting expressions for  $f_{\text{az}}$  and  $f_{\text{el}}$  as functions of antenna width, a restriction on the antenna dimensions necessary for SAR processing arises:

$$d_{\text{az}} d_{\text{el}} \geq 4ab\lambda\rho v_{\text{sc}} \tan\theta_i (\mu\xi)_{\text{az}} (\mu\xi)_{\text{el}} / c \quad (5.4)$$

where the  $\mu$  parameters indicate the portion of the beam-width illuminated region usable for range and Doppler footprints (we assume them to be unity in this study). If the antenna is circular, the two antenna dimensions are equal, and the above equation yields a single minimum antenna diameter needed for SAR processing.

This minimum antenna size is shown in Figures 5-3 and 5-4 for Ku- and C-band, respectively. Values of  $a$  and  $b$  of 1 and 2 are shown, along with a value of 1.75 preferred by Sp03. Although the antenna size required increases as the altitude increases, the SAR increase is much less than that of the real-aperture case, due primarily to the effect of the square root of the range in Eq. 5.4 versus the linear relationship with range in Eq. 5.1.

SAR-enabled systems require larger antennas than traditional resolution, real-aperture systems at lower altitudes (although the SAR resolution is an order of magnitude better than the traditional system). At higher altitudes, SAR processing is highly desirable, as much smaller antennas are needed than for even the worst acceptable non-SAR resolution. At LEO to MEO altitudes, SAR processing requires antenna sizes of at least 2–3 m diameter, but no more than 7–12 m, depending on frequency.

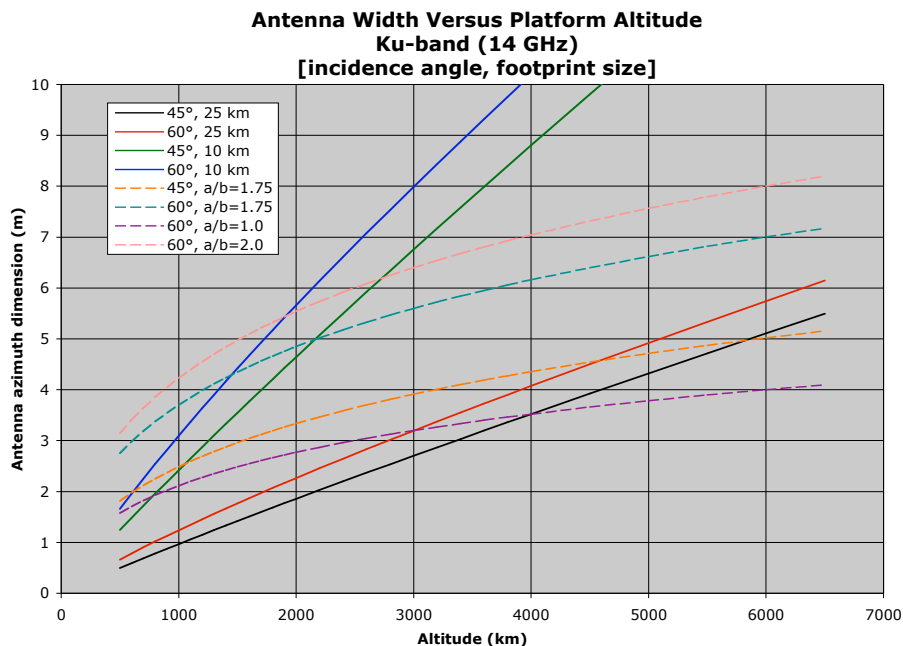


**Figure 5-3: Minimum antenna width to permit SAR processing (dashed lines), compared to size needed to achieve real-aperture resolution (solid lines), for Ku-band system.**

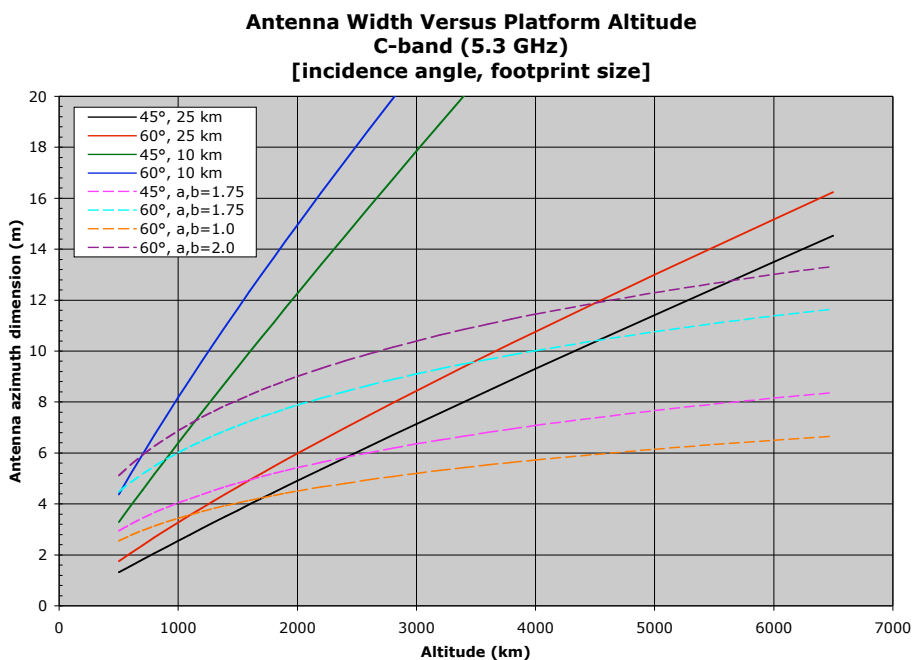


**Figure 5-4: Minimum antenna width to permit SAR processing (dashed lines), compared to size needed to achieve real-aperture resolution (solid lines), for C-band system.**

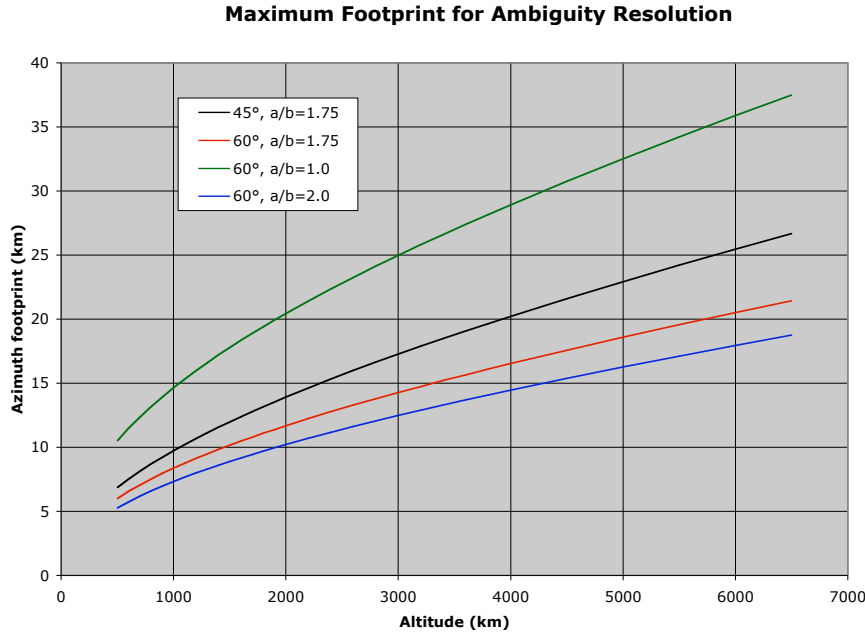


**Figure 5-5: Approximate azimuth footprint size corresponding to minimum antenna dimension required for ambiguity resolution, for Ku-band system.**

Figure 5-5 illustrates the approximate footprint size generated by an antenna with a minimum antenna width needed to resolve range and Doppler ambiguities for a Ku-band system. Thus, given the smallest antenna for “full-footprint” SAR processing, ground resolution without SAR, or in the part of the swath where SAR processing is impossible (at azimuths close to 0° and 180°), is approximately as shown in this figure. For most altitudes under study, ground resolutions can be 25 km or better. At C-band, resolutions are worse by about 50%.

Due to the rotation of the pencil-beam antenna (see Section 5.1.3), limits on the antenna dwell time differ from those of traditional SAR systems (Sp03). This affects the Doppler resolution, hence the SAR azimuth resolution, of the system. A best, theoretical, broadside (i.e.,  $\phi_{az}=90^\circ$ ), SAR azimuth resolution, given spin and ambiguity constraints, is given by

$$\Delta x_{az} = \frac{4\pi ab\rho v_{gr} \sin\theta_i \sin\theta_l}{cN_b} \quad (5.5)$$

where  $v_{gr}$  is the apparent speed of the spacecraft along the sub-satellite ground track,  $v_{gr} = \left(\frac{R}{R+h}\right)v_{sc}$ , and  $N_b$  is the number of adjacent radar beams in the elevation direction (reducing the necessary spin rate of the spacecraft). Note that this resolution is wavelength independent, and the only physical parameters affecting this “best” resolution are altitude, incidence angle, and number of elevation beams.

Figure 5-6 illustrates this resolution for a single elevation beam system. Two beams would increase the resolution, i.e., decrease the resolution cell size shown, by a factor of

two. Note that resolution worsens with increasing altitude at LEO, due to the increase in slant range, but improves at MEO due to the reduction in apparent spacecraft ground velocity. For any altitude, resolution is worse at larger incidence angles.

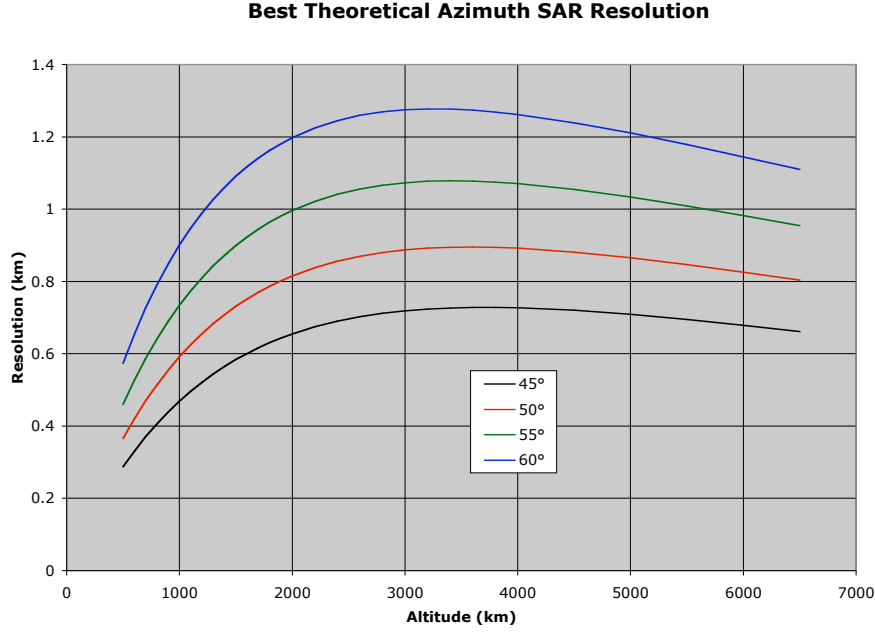


**Figure 5-6: Best SAR resolution in azimuth, computed at broadside, for system with single elevation beam.**

### 5.1.3 Antenna Rotation Rate Issues

For a pencil-beam scatterometer system, the rotation or spin rate of the antenna must be sufficient to ensure that the target footprints overlap in the elevation direction along the sub-satellite ground path. For a given beam width in elevation, smaller incidence angles require faster spinning, as the elevation footprint is less elongated. Alternatively, for the same spin rate, smaller incidence angles require larger beamwidths to prevent along-track gaps. A lower, more quickly moving satellite or a smaller footprint size (larger antenna) dictates a faster spin rate. A faster rotation rate may be harder to implement technologically due to hardware and angular momentum considerations. The spin rate can always be reduced, however, by employing multiple adjacent beams in elevation, thus effectively increasing the footprint elevation size.

The required minimum rotation rate is given by

$$\Omega = \frac{2\pi v_{gr}}{\eta f_{el} N_b} = \frac{2\pi v_{gr} \cos \theta_i}{\eta \rho \beta_{el} \mu_{el} N_b} \quad (5.6)$$

where  $\eta$  is the ratio of non-overlapping footprint size in elevation between adjacent spin swaths (a value of one indicates no overlap, while a value less than one indicates some

overlap, hence faster spinning). The rotation rate as a function of altitude is shown in Figure 5-7 for  $\eta=1$ .

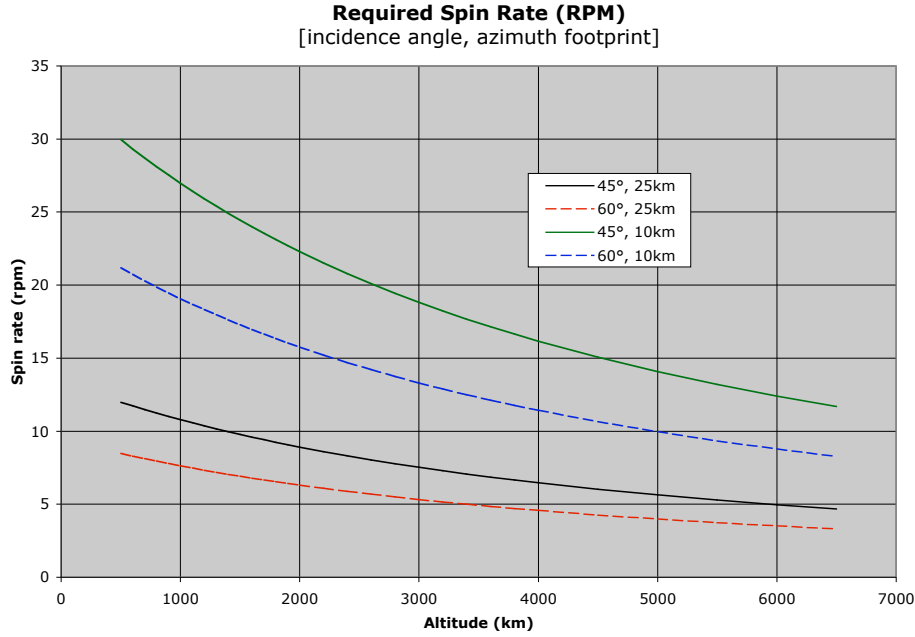


**Figure 5-7: Minimum spin rate needed to remove along-track imaging gaps in the sub-satellite ground track, assuming one elevation beam. Faster spin rates would overlap footprints between rotating scans.**

Although spin rates of 10-20 rpm, or even 30 rpm, are technically feasible, there are other reasons for attempting to slow the rotation. One primary consideration is that target dwell time, hence Doppler azimuth resolution, is inversely proportional to rotation rate. This is shown by

$$\Delta x_{az} = \rho \sin \theta_l \Delta \phi_{az} = \frac{\lambda \rho \Delta F_{Dop}}{2v_{sc} \sin \phi} = \frac{\lambda \rho}{2v_{sc} \sin \phi} \left( \frac{\Omega \sin \theta_l}{\mu_{az} \beta_{az}} \right) \quad (5.7)$$

where  $\Delta \phi_{az}$  is the azimuth angular resolution and  $\Delta F_{Dop}$  is the Doppler frequency resolution. Since the smallest  $\Delta x_{az}$  corresponds to the best resolution, the smallest spin rate  $\Omega$  is desired. If two elevation beams are used, for example, the rotation rate is cut in half, thus doubling the potential SAR azimuth resolution.

Given the small beam width of the scatterometer antenna, a rapid spin rate also has the unfortunate consequence of moving the antenna pointing significantly between transmit and receive events. The number of two-way beam widths, or azimuth footprints, through which the antenna moves between transmit and receive epochs is given by

$$\kappa \equiv \Delta_{az} / f_{az} = \left( \Omega \rho \sin \theta_l \right) \left( \frac{2\rho}{c} \right) / f_{az} \quad (5.8)$$

where  $\Delta_{az}$  is the motion of the antenna footprint during the round-trip propagation time. This value is shown, as a function of altitude, incidence angle, and footprint size, in

Figure 5-8. Since values greater than about 0.5 footprint widths reduce the return signal excessively, separate transmit and receive feeds will be needed for all except the lowest LEO scatterometers and the largest footprint sizes. The ground displacement ratio also indicates the number of two-way beam widths in azimuth by which the transmit and receive feeds must be separated at the antenna.

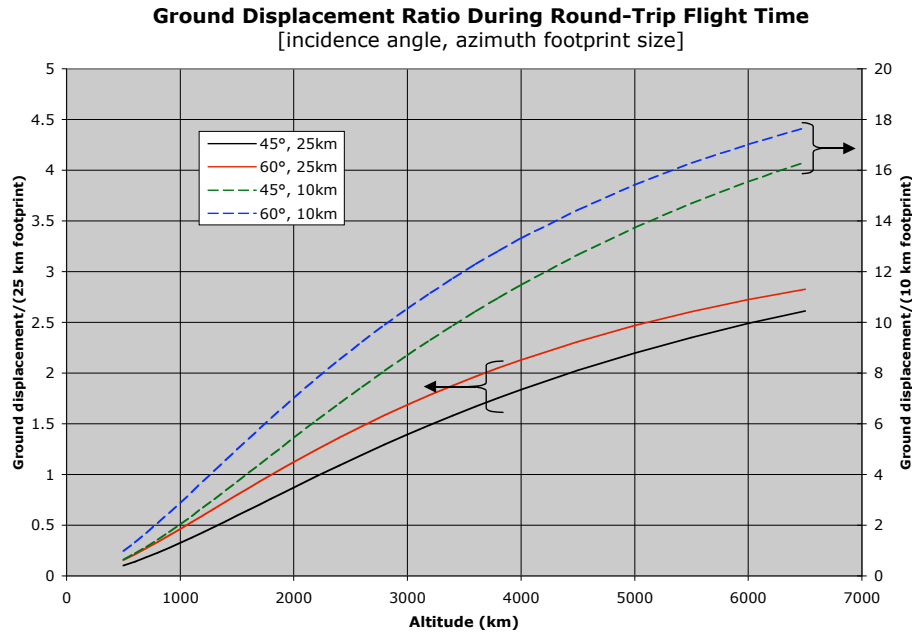


**Figure 5-8: Ground motion of the antenna footprint during round-trip signal propagation, given as number of azimuth footprint widths.**

#### 5.1.4 Imaging Times and Measurement Duration

An additional altitude-related consideration deals with the swath width. Although the surface coverage of the pencil beam increases as the altitude increases, the time between imaging a given ground location when the beam points forward and when the beam points aft, essential for scatterometer recovery, also increases as a function of altitude, as shown in Figure 5-9. If the time interval is too large, the wind may change excessively between images, degrading the scatterometer recovery. The smaller the resolution cell on the ground, the shorter this time interval should be. Although not a major problem for a 25 km footprint spot, for a ~1 km SAR azimuth and range resolution cell, the time intervals shown in the figure for MEO may be excessive.

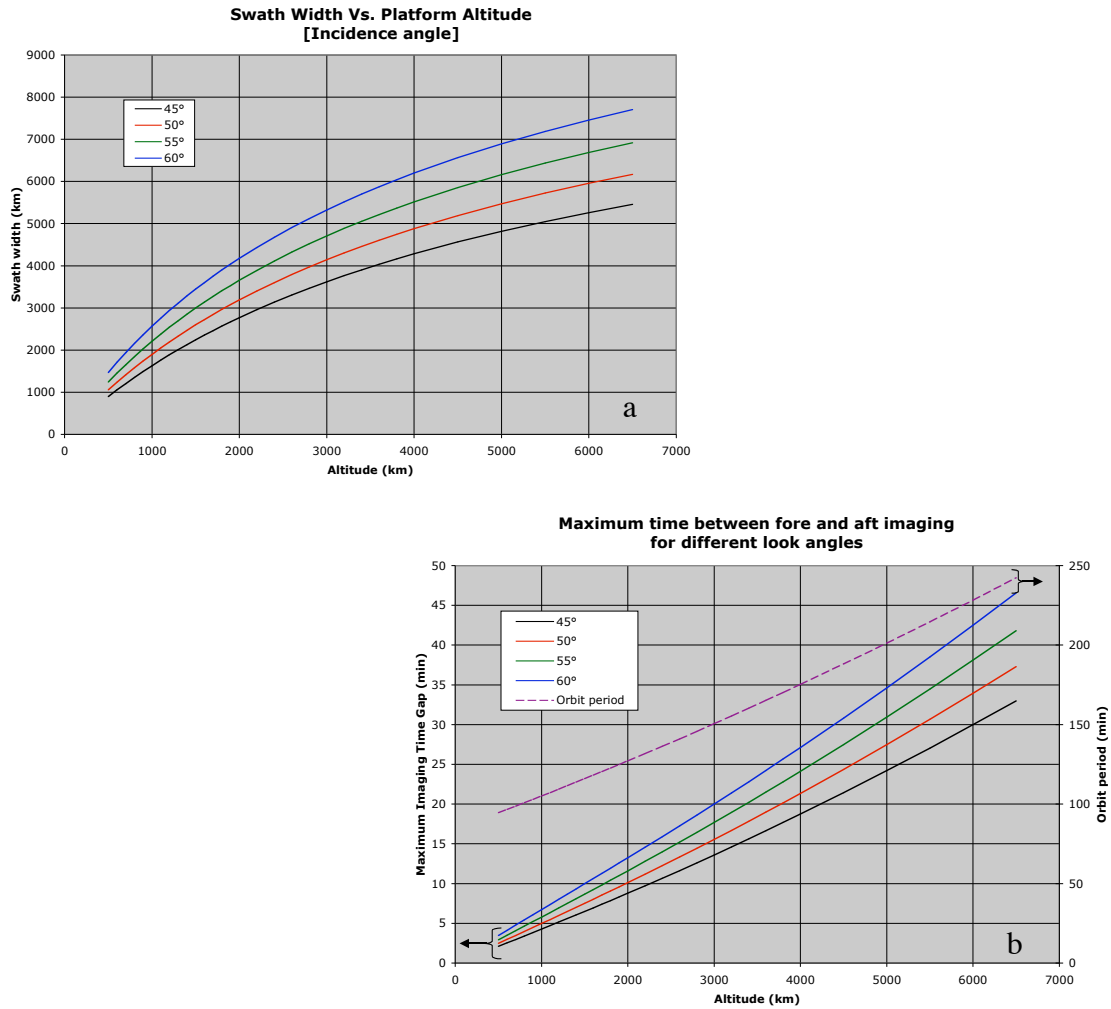


**Figure 5-9: (a) Total swath width covered by scatterometer, and (b) orbit period and time interval between fore and aft looks of scatterometer at points along the sub-satellite track.**

## 5.2 Strawman Antenna Design Examples

As an illustration of how the preceding analysis can be used to create an antenna design, an initial set of radar parameter and design requirements was developed based on a “strawman” scatterometer operating at 1500 km altitude. This scatterometer has two beam or feed clusters generating observations at two incidence angles, 60° and 50°, allowing reasonable recovery of the ocean wind state from the known model functions (See Figure 5-10). These incidence angles create an inner swath whose width is about 75% of the outer swath width. The primary frequency, used for SAR processing, is at Ku-band. We propose an optional, second frequency system at C-band utilizing the same reflector antenna as the primary system (assuming a dish-type reflecting antenna), operating in a non-SAR, real-aperture mode.

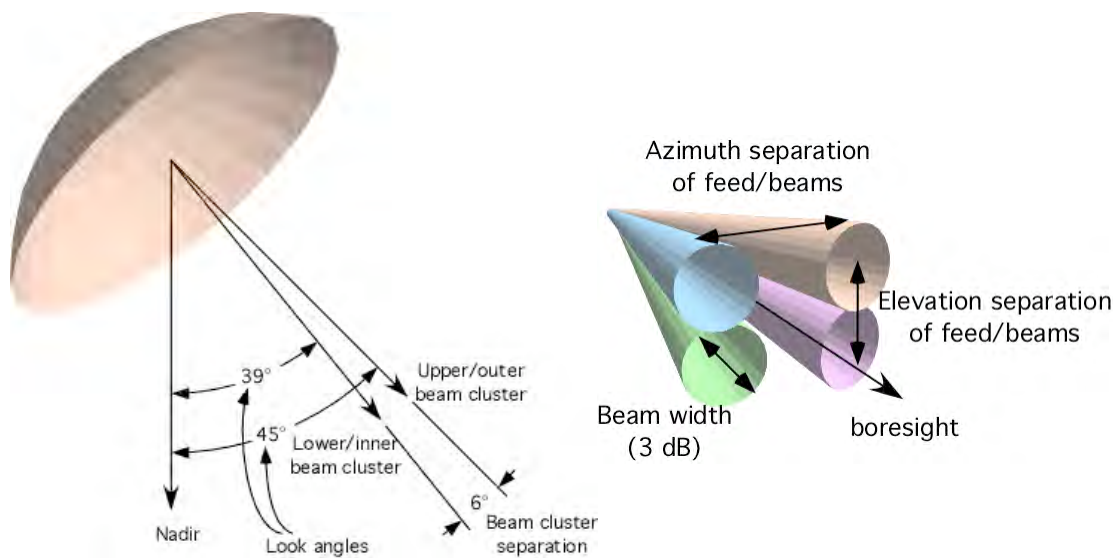


**Figure 5-10: Configuration of proposed strawman scatterometer.**

We look at two possible platform rotation schemes. A fast spin strategy allows the use of only one beam in elevation for both the outer and inner beam cluster, but reduces the spot dwell time and thus increases the potential best resolution cell size. It also requires that the inner beam use less aperture in order to yield a larger beam width. A slow spin strategy allows both beams to have the same width, but requires multiple beams in elevation, two for the outer cluster, three for the inner cluster. This strategy does allow dwell time, hence Doppler ground resolution, to increase by a factor of two or more. This increased dwell time may prove helpful if other factors, such as transmit/receive pulse interleaving or burst mode processing, effectively reduce the dwell time even further. Variations on these two schemes are possible and may be examined more closely, depending on antenna design issues currently under study.

Table 5-1 describes some general orbit and system parameters for the strawman design. Table 5-2 includes information about ground surface coverage and system geometry that differ for the outer and inner footprints and swaths. Table 5-3 describes the antenna design parameters calculated for the strawman scatterometer system. Note that beam widths listed in the table are one-way 3-dB widths (equivalent to two-way 6-dB widths), while two-way 3-dB widths were used to generate footprint sizes.

**Table 5-1: General system parameters.**

Parameter	Units	Value
Altitude	km	1500
Platform orbital speed	km/s	7.1
Platform speed projected on ground	km/s	5.8
Ku-band frequency	GHz	14
C-band frequency	GHz	5.3



**Table 5-2: Surface coverage information for strawman system, for outer and inner swaths, for fast and slow spin rates, and for both frequencies ( $\kappa$  refers to equation 5.8).**

Parameter		Units	Outer footprint	Inner footprint
Incidence angle		<i>deg</i>	60	50
Swath width		<i>km</i>	3450	2600
Slant range (center of footprint)		<i>km</i>	2430	2080
Minimum antenna diameter for SAR		<i>m</i>	4.3	3.3
<b>Ku-band</b>				
<b>Fast spin</b>				
Rotation rate		<i>rpm</i>	21	21
Approx. antenna diameter		<i>m</i>	4.5	3.5
Azimuth footprint width		<i>km</i>	9.8	10.8
Elevation footprint width		<i>km</i>	19.6	16.8
Number of pulses within footprint			13	24
Value of $\kappa$			6.2	3.6
Azimuth SAR resolution		<i>km</i>	1.4	0.8
<b>Slow spin</b>				
Rotation rate		<i>rpm</i>	9	9
Approx. antenna diameter		<i>m</i>	4.5	4.5
Azimuth footprint width		<i>km</i>	9.8	8.4
Elevation footprint width		<i>km</i>	19.6	13.1
Number of pulses within footprint			30	47
Value of $\kappa$			2.6	2.0
Azimuth SAR resolution		<i>km</i>	0.6	0.4
<b>C-band</b>				
<b>Fast spin</b>				
Azimuth footprint width		<i>km</i>	25.9	28.5
Elevation footprint width		<i>km</i>	51.8	44.3
Number of pulses within footprint			13	25
Value of $\kappa$			2.3	1.4
<b>Slow spin</b>				
Azimuth footprint width		<i>km</i>	25.9	22.2
Elevation footprint width		<i>km</i>	51.8	34.5
Number of pulses within footprint			31	60
Value of $\kappa$			1.0	0.7

**Table 5-3: Antenna design parameters for strawman system, for outer and inner swaths, for fast and slow spin rates, and for both frequencies.**

Parameter		Units	Upper cluster	Lower cluster
Look angle		<i>deg</i>	44.5	38.3
<b>Ku-band</b>				
<b>Fast spin</b>				
Number of elevation feeds			1	1
Feed separation in az		<i>deg</i>	NA	NA
Feed separation in el		<i>deg</i>	NA	NA
Beam widths (3 dB)		<i>deg</i>	0.33	0.42
Number of azimuth (T/R) feeds			2	2
Feed separation in az		<i>deg</i>	1.43	1.08
Feed separation in el		<i>deg</i>	<0.1	<0.1
Beam widths (3 dB)		<i>deg</i>	0.33	0.42
PRF		<i>Hz</i>	4900	6300
<b>Slow spin</b>				
Number of elevation feeds			2	3
Feed separation in az		<i>deg</i>	no requirement	no requirement
Feed separation in el		<i>deg</i>	0.23	0.23
Beam widths (3 dB)		<i>deg</i>	0.33	0.33
Number of azimuth (T/R) feeds			2	2
Feed separation in az		<i>deg</i>	0.60	0.45
Feed separation in el		<i>deg</i>	<0.1	<0.1
Beam widths (3 dB)		<i>deg</i>	0.33	0.33
PRF		<i>Hz</i>	4900	6600
<b>C-band</b>				
Number of elevation feeds			1	1
<b>Fast spin</b>				
Beam widths (3 dB)		<i>deg</i>	0.86	1.11
Number of azimuth (T/R) feeds			2	2
Feed separation in az		<i>deg</i>	1.43	1.08
Feed separation in el		<i>deg</i>	<0.2	<0.3
PRF		<i>Hz</i>	1900	2500
<b>Slow spin</b>				
Beam widths (3 dB)		<i>deg</i>	0.86	1.04
Number of azimuth (T/R) feeds			2	2
Feed separation in az		<i>deg</i>	0.60	0.45
Feed separation in el		<i>deg</i>	<0.2	<0.3
PRF		<i>Hz</i>	1900	3200

### 5.3 Scatterometer Measurement Accuracy

The RMS error associated with the measurement of  $\sigma_0$ ,  $\Delta\sigma_0$ , is typically defined as

$$\Delta\sigma_0 = K_p \sigma_0, \quad (5.9)$$

where the  $K_p$  parameter is the normalized standard deviation of the measurement, and is thus defined by

$$K_p = \frac{\sqrt{\text{Var}[\sigma_0]}}{\sigma_0}. \quad (5.10)$$

For a radar measurement, the  $K_p$  parameter is, in general, given by

$$K_p = \sqrt{K_{pr}^2 + K_{pc}^2}, \quad (5.11)$$

where  $K_{pr}$  is the normalized standard deviation of the calibration error and  $K_{pc}$  is the radar precision due to random fading and noise. (Note that the subscript “c” in  $K_{pc}$  stands for “communication noise” and the subscript “r” in  $K_{pr}$  stands for “retrieval noise.” These rather confusing designations are used for historical reasons. Care should be taken to not associate them with “calibration” and “random,” respectively.)  $K_{pc}$  is given by:

$$K_{pc} = \frac{1}{\sqrt{N}} \left( 1 + \frac{2}{SNR} + \frac{1}{SNR^2} \right)^{1/2}, \quad (5.12)$$

where  $N$  is the equivalent radar looks associated with the measurement and  $SNR$  is the signal-to-noise ratio defined by

$$SNR = \frac{P_t G^2 \delta_{el} \delta_{az} \lambda^2 (n_p T_p) \sigma_0}{(4\pi)^3 R^4 L N_0}, \quad (5.13)$$

where  $P_t$  is the transmit power,  $G$  is the antenna gain in the direction of the measurement cell,  $\delta_{el}$  is the elevation (range) dimension of the measurement cell,  $\delta_{az}$  is the azimuth dimension of the measurement cell,  $\lambda$  is the wavelength,  $n_p$  is the number of pulses coherently averaged to form the measurement cell (note that  $n_p = 1$  for the real aperture case),  $T_p$  is the pulse length,  $R$  is the slant range to the resolution cell,  $L$  is the system loss, and  $N_0$  is the equivalent system noise power spectral density. In this section, we are primarily concerned with selecting the high level radar electronics parameters (transmit power, pulse modulation, processing, etc.), and thus are primarily concerned about optimization of the metric  $K_{pc}$ .

## Real Aperture Pencil-Beam Systems

Real aperture systems utilize range processing only to subdivide the footprint into elevation “slices.” The azimuth dimension of the footprint is determined by the azimuth width of the antenna footprint projected on the surface. This is the resolution approach utilized by the SeaWinds scatterometer (see Spencer, et al. 2000). For such a system, one relatively long radar pulse is transmitted, from which a single  $\sigma_0$  resolution cell (or a single set of  $\sigma_0$  elevation “slices”) is derived. These  $\sigma_0$  measurements, from different azimuth views of the surface, are then binned into a grid on the surface at the desired wind vector cell resolution for wind retrieval (see Naderi, et al. 1991).

For real aperture systems, the total number of looks per radar pulse,  $N_{rp}$ , is given by

$$N_{rp} = \frac{\Delta x_{el}}{\delta_{el}}, \quad (5.14)$$

where  $\Delta x_{el}$  is the elevation dimension of the useful portion of the antenna footprint as projected on the surface (typically defined as the 2-way 3 dB elevation footprint). The total number of looks within a wind resolution cell,  $N_{wc}$ , is then the product of the number of radar pulses which fall into this cell and the number of looks per pulse, or

$$N_{wc} = \left( \frac{\tau_{wc}}{PRI} \right) \times \left( \frac{\Delta x_{el}}{\delta_{el}} \right), \quad (5.15)$$

where  $\tau_{wc}$  is the total amount of time that the antenna boresight dwells in the wind cell bin and PRI is the pulse repetition interval (inverse of the PRF). The wind vector cell dwell time is in turn given by

$$\tau_{wc} = \left( \frac{\delta_{wc}}{v_g} \right) \times \left( \frac{\delta_{wc}}{2\pi d} \right) \times f(swath), \quad (5.16)$$

where  $\delta_{wc}$  is the wind vector cell resolution (i.e., grid size),  $v_g$  is the spacecraft ground velocity, and  $d$  is the radius of circle on the Earth traced out by the spinning antenna. The first term in Eq. 5.16 is how long it takes the spacecraft to move one resolution cell, the second term is the fraction of the time the antenna will dwell in a resolution cell on the nadir track, and the term  $f(swath)$  takes into account the increasing overlap of measurements towards the edge of the swath. The factor  $f(swath)$  is approximately 1 everywhere except on the very edge of the swath, so we can write

$$\tau_{wc} = \frac{\delta_{wc}^2}{v_g 2\pi d}. \quad (5.17)$$

Note that  $\tau_{wc}$  is independent of the antenna rotation rate. In Figure 5-11 below,  $\tau_{wc}$  is plotted vs. altitude for two incidence angles ( $54^\circ$  and  $60^\circ$ ) as well as two resolutions (25

km and 10 km). The dwell times are higher for lower resolution and lower incidence angles as expected from Eq. 5.17. Note that the dwell time decreases rapidly as a function of altitude up to a value of 3000 km, then starts to slowly increase again. This behavior is the same as noted for the area coverage rate analysis in Section 4, and is due to the product  $v_g d$  in the above equation for  $\tau_{wc}$ .

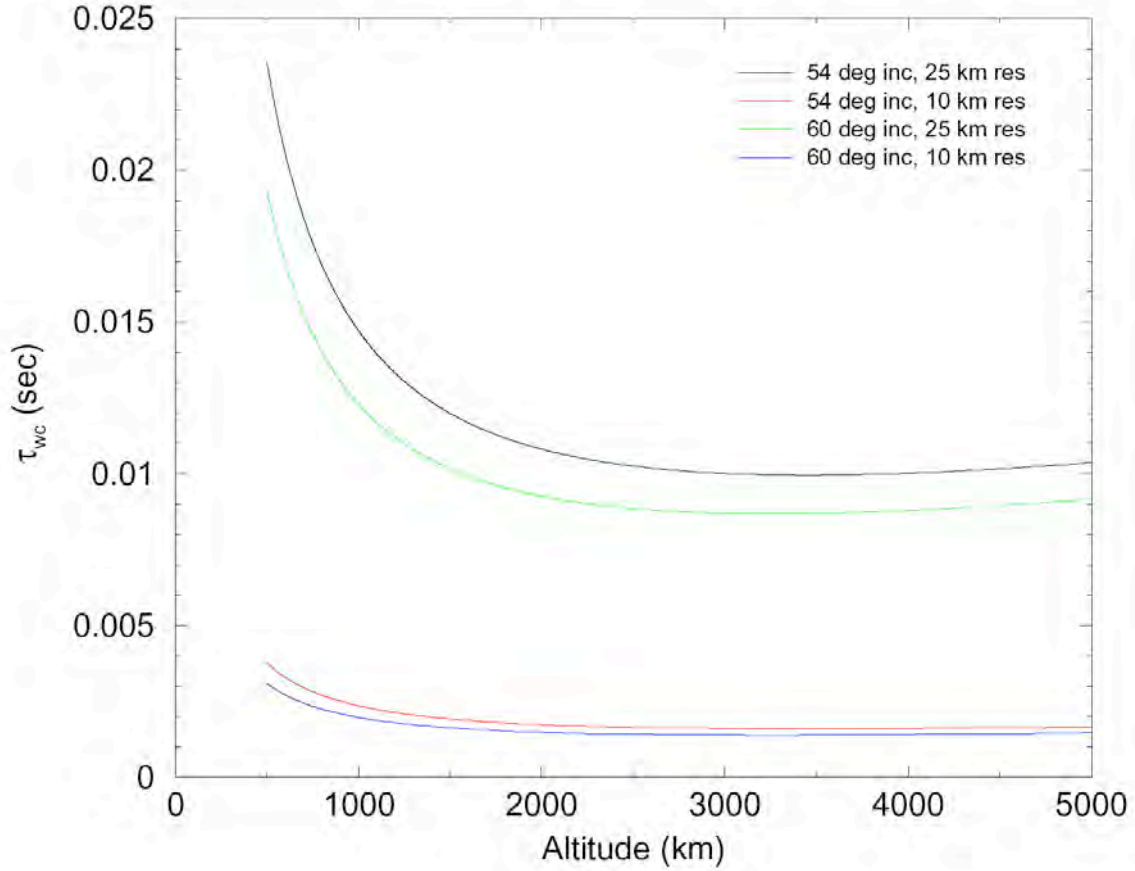


**Figure 5-11: Wind vector cell dwell time ( $\tau_{wc}$ ) vs. altitude.**

The number of looks associated with each pulse is related to the inherent elevation resolution on the ground associated with the transmitted bandwidth. The inherent elevation resolution,  $\delta_{el}$ , is given by:

$$\delta_{el} = \frac{c}{2 \sin \theta_i B_t}, \quad (5.18)$$

where  $\theta_i$  is the incidence angle and  $B_t$  is the transmitted bandwidth. Defining  $\gamma$  as the chirp rate, and  $T_p$  as the transmit pulse length,  $B_t = \gamma T_p$ , and

$$\delta_{el} = \frac{c}{2 \sin \theta_i \gamma T_p}. \quad (5.19)$$

Returning to Eq. 5.15, we therefore have that the product  $PRI\delta_{el}$  is given by

$$PRI\delta_{el} = \frac{cPRI}{2\sin\theta_i\gamma T_p}. \quad (5.20)$$

Assuming that  $f_d = T_p/PRI$ , where  $f_d$  is defined as the single beam duty factor, we then write

$$PRI\delta_{el} = \frac{c}{2\sin\theta_i\gamma f_d}. \quad (5.21)$$

Also, since  $\Delta x_{el}$  is given by

$$\Delta x_{el} = \frac{\Delta t_{el}c}{2\sin\theta_i} \quad (5.22)$$

(where  $\Delta t_{el}$  is the beam fill time), we can insert the expressions for Eq. 5.21 and Eq. 5.22 into Eq. 5.15 to obtain:

$$N_{wc} = \tau_{wc}\Delta t_{el}\gamma f_d = \tau_{wc}B_{bb}f_d \quad (5.23)$$

Where  $B_{bb}$  is the baseband bandwidth associated with a single de-chirped pulse (see Spencer, et al. 2000). This expression makes sense. Essentially it says that the number of looks is equal to the net baseband time-bandwidth product. As an alternate expression, consider that Eq. 5.19 can be reordered as an expression for  $\gamma$

$$\gamma = \frac{c}{2\sin\theta_i\delta_{el}T_p}, \quad (5.24)$$

and that

$$\Delta t_{el} = \frac{\Delta x_{el}2\sin\theta_i}{c}, \quad (5.25)$$

so that Eq. 5.23 becomes

$$N_{wc} = \frac{\tau_{wc}\Delta x_{el}f_d}{\delta_{el}T_p}. \quad (5.26)$$

As described in Spencer et al. 2000, there is an important trade-off between the number of looks taken and the  $SNR$ . For a given antenna and scan geometry, the product  $\tau_{wc}\Delta x_{el}f_d$  is fixed. As more looks are taken to decrease  $K_{pc}$  however, the above equation indicates that the product  $\delta_{el}T_p$  must necessarily decrease. As  $\delta_{el}T_p$  decreases, the  $SNR$

will also decrease, which will tend to *increase*  $K_{pc}$ . There is consequently a balance that must be obtained between increasing the number of range looks and decreasing  $SNR$ .

For this study, we wish to obtain design parameters for systems operating at higher orbits or higher resolution. In general, we wish the system to perform with approximately the same rain-free wind speed and direction accuracy as SeaWinds. Therefore, we desire a system that obtains the same number of looks per measurement cell and the same  $SNR$  as SeaWinds. Utilizing the equations developed above, we can “bootstrap” the SeaWinds performance to indicate how the radar parameters – specifically the transmit power and transmit bandwidth – will have to change in order to obtain the same performance as SeaWinds.

First consider the case where the wind vector cell resolution is improved by a factor of 2 over SeaWinds, but the orbit and incidence angles are held the same. For this case the antenna size must be a factor of 2 larger than SeaWinds (2 m as opposed to 1 m) in order to obtain the improved resolution. Note that because  $\delta_{wc}$  is a factor of 2 larger,  $\tau_{wc}$  is a factor of 4 smaller. Also note that the factor of 2 improvement in resolution implies that  $\Delta x$  is also smaller by a factor of 2. Assuming that the duty factor remains  $f_d = 0.16$ , in order to maintain the same number of looks that SeaWinds obtains ( $N_{wc} = 113$ ), the product  $\delta_{el}T_p$  must decrease by a factor of 8. Turning to the expression for  $SNR$ , we note that the product  $\delta_{az}\delta_{el}T_p$  will therefore decrease in total by a factor of 16. However, doubling the antenna size will increase the gain by a factor of 4, and hence the  $G^2$  term by a factor of 16, exactly compensating for the decrease in the other terms. Consequently, the same transmit power as employed on SeaWinds (100 W) may be used to get the exact same performance at the higher resolution.

For higher orbits the calculations must also take into account the variations in slant range, orbit period, etc., and are thus somewhat more complicated. One way of addressing the problem is to assume that the transmit power is held constant at the SeaWinds value (i.e.,  $P_t = 100$  W). We also assume that, regardless of orbit altitude and resolution, the same number of looks that SeaWinds achieves is maintained (i.e.,  $N_{wc} = 113$ ). We can then plot the  $\Delta SNR$  – the thermal  $SNR$  relative to that achieved by SeaWinds – as a function of altitude. Plots of  $\Delta SNR$  for incidence angles of  $54^\circ$  and  $60^\circ$  are shown in Figure 5-12. Note that these curves, like the curves for dwell time, decrease rapidly up to an altitude of 3000 km, then start to climb back up again.

As an example, consider an altitude of 1500 km. Here, a transmitter with the same power as SeaWinds, operating at the same duty cycle, with an antenna precisely larger in size to compensate for the higher altitude, and achieving the same number of looks within the wind vector cell, will have a thermal  $SNR$  that is 1.5 dB less than SeaWinds. Higher altitudes will have, at most, 2 dB less  $SNR$  than SeaWinds. Because other design approaches – such as decreased scanning loss, slightly increased antenna size, and/or higher duty factor – can be used to recoup this relatively small loss in  $SNR$ , we conclude that a SeaWinds-class transmitter (100 W peak transmit power) can be used successfully at any altitude, provided that the antenna size grows proportionately with the desired altitude and resolution.



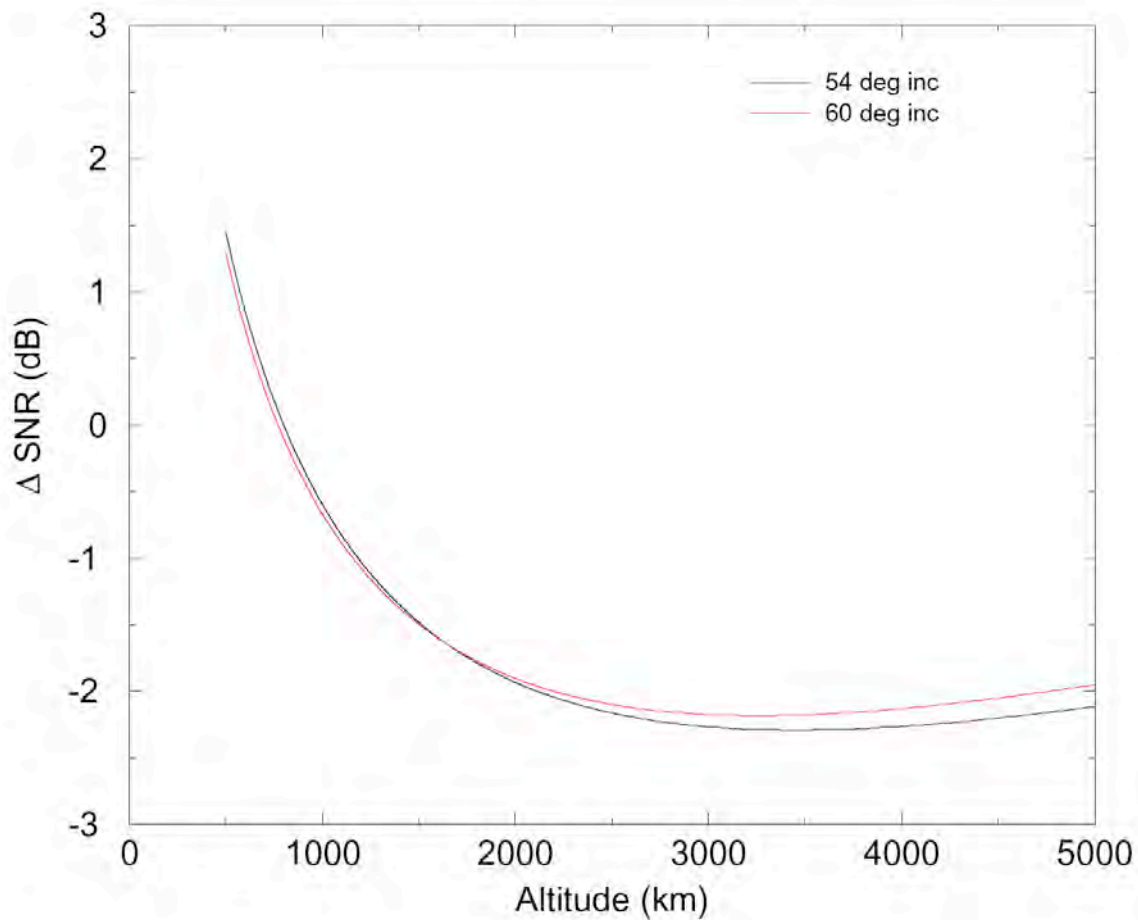


**Figure 5-12: Plot of  $\Delta$ SNR relative to SeaWinds as a function of altitude. The total number of looks per resolution cell is constrained to be the same as for SeaWinds.**

As another way to examine the transmit power and antenna aperture trade-offs, consider Figure 5-13. Here, the required transmit power to maintain the same number of looks and SNR as SeaWinds is plotted vs. the antenna diameter for a Ku-Band system at an orbital altitude of 1500 km. Note that there is a minimum antenna diameter that corresponds to resolutions of 10 km and 25 km respectively. Subjective limits of current antenna and Ku-Band transmitter technology are also indicated. Assuming that the desired resolution is 10 km, an optimal design point appears to be for an antenna size of 4.5 m and a transmit power of 120 W. Such a system would both meet performance requirements, and be achievable with current technology.

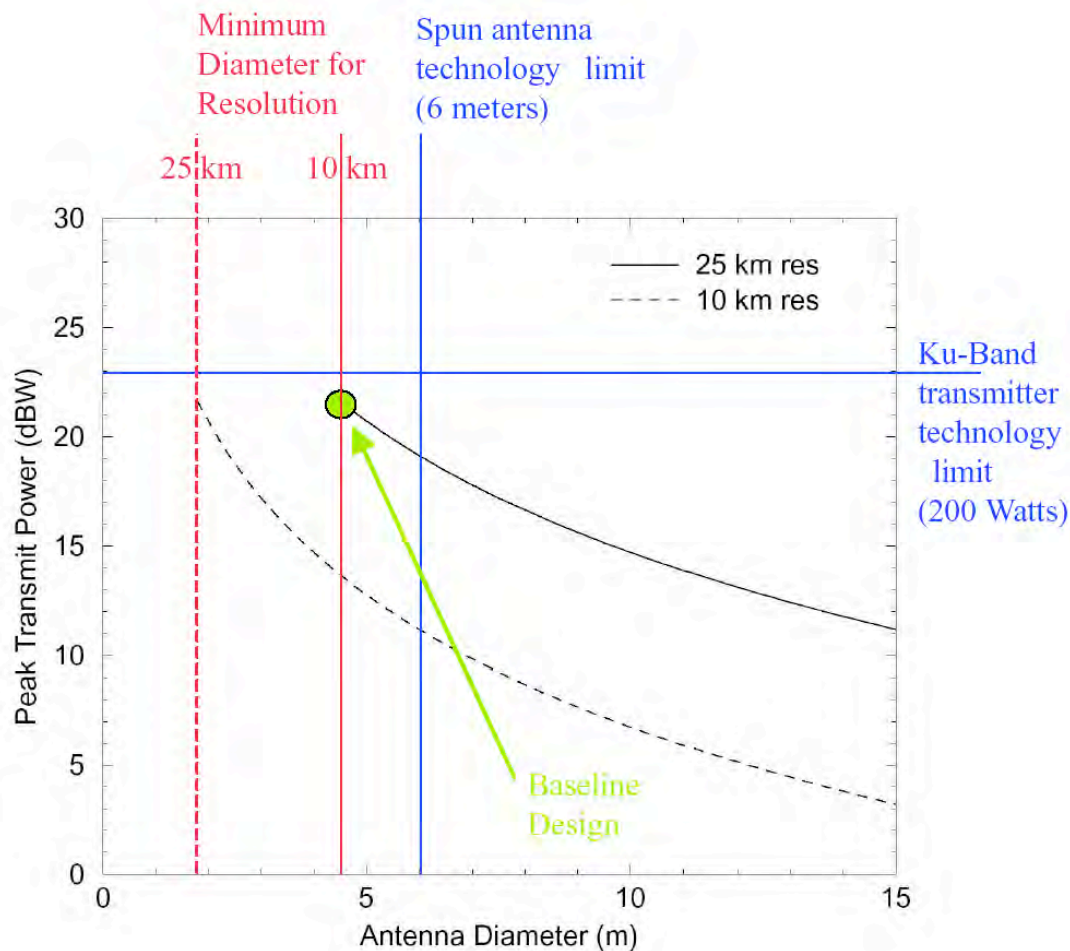


**Figure 5-13: Plot of required transmit power vs. antenna diameter for a Ku-Band system operating at 1500 km orbit. The two black curves are generated assuming that the number of looks and SNR are the same as the SeaWinds values (i.e., the same SeaWinds measurement performance). Note that there are minimum antenna diameters to achieve 10 and 25 km resolution respectively. Also note that a qualitative assessment of current antenna and transmitter technology limits have been indicated. For the desired resolution of 10 km, an optimal “baseline design” point is shown (antenna diameter of 4.5 m, and transmit power of 120 W), which meet performance requirements and is consistent with current technological capabilities.**

## 5.4 References

Naderi, F., Freilich, M.H., and Long, D.G., “Spaceborne Radar Measurement of Wind Velocity Over the Ocean – An Overview of the NSCAT Scatterometer System,” *Proceedings of the IEEE*, Vol. 79, No. 6, pp. 850–866, June 1991.

Spencer, M.W., Wu, C., and Long, D.G., "Improved Resolution Backscatter Measurements with the SeaWinds Pencil-Beam Scatterometer," *IEEE Trans. Geosci. and Remote Sensing*, Vol. 38, No. 1, pp. 89–104, January 2000.

Spencer, M.W., Wu, C., and Long, D.G., "High-Resolution Measurements With a Spaceborne Pencil-Beam Scatterometer Using Combined Range/Doppler Discrimination Techniques," *IEEE Trans. Geosci. and Remote Sensing*, Vol. 41, No. 3, pp. 567–581, March 2003.

## 6. Conically-Scanning Antenna Design Trade-Offs

### 6.1 General Antenna Design Characteristics

To illustrate the issues encountered in designing a reflector to operate at higher altitude and/or higher resolutions, we first consider the SeaWinds antenna design (see Figure 6-1). The SeaWinds instrument was designed to operate at an orbit of 800 km, and to have a real aperture resolution of 25 km on the Earth's surface. To meet these requirements, a reflector diameter of 1 meter was used. The antenna was a front-fed, axi-symmetric design, with the feeds supported near the focal point and an  $f/D$  ratio of 0.6. Two rectangular feed horns were used – an H-polarized horn to form the inner beam, and a V-polarized horn to form the outer beam (e.g., see Section 3). The inner and outer beams were scanned  $\pm 3^\circ$  from the antenna boresight, and were consequently somewhat offset from the focal point. The beams were designed to be slightly elliptical, but had a 3 dB width of approximately  $1.5^\circ$  in the elevation dimension. The SeaWinds beams were therefore scanned only about 2 beamwidths off of focus, and little beam degradation occurred. At the SeaWinds altitude, a rotation rate of 18 rpm was used to assure that the 2-way 3 dB footprints overlapped by 30% in the along-track direction.

As the altitude or resolution is increased beyond that used for SeaWinds, the reflector size must increase and the beamwidths must proportionately narrow. This improved antenna capability comes at the cost of increased antenna complexity. Three key design factors are discussed below: 1) beam scanning, 2) transmit/receive separation, and 3) increased spin rate and added elevation beams.

*1. Beam Scanning:* In order to obtain a minimum of three azimuth measurements of the surface with a conically scanning reflector antenna, at least two beams pointing at different look angles must be used (the inner and outer beams on SeaWinds, for example). Reflector antennas that use only one primary reflector surface, such as front-fed axi-symmetric and offset-fed designs, only come to focus at one point. As beams are scanned off of this focal point, the gain and beam shape degrade. This degradation is a function of how many beamwidths the antenna is scanned and what  $f/D$  ratio is used. SeaWinds, for instance, scans only 2 beamwidths from the focal point, and therefore still achieves good quality beams with an  $f/D$  ratio of 0.6.

As the altitude or resolution increases, the beamwidth narrows, but the angle that the antenna must scan stays the same. This means that the number of beamwidths scanned could increase significantly. For instance, at an altitude of 1500 km (roughly twice that of SeaWinds), and a real-aperture resolution of 10 km (a factor of 2.5 better than SeaWinds), the beamwidth needed is approximately 0.3 degrees, requiring an antenna with a diameter of approximately 4.5 meters. In order to achieve measurements on the surface with the same azimuth diversity as SeaWinds, the inner and outer beams must be scanned roughly the same  $\pm 3^\circ$  from the boresight, implying that the beams are scanned about 10 beamwidths. To form an acceptable beam with such a large scan requires a larger  $f/D$  ratio.

In Appendix A, a study is presented showing beam degradation as a function of  $f/D$  for the 4.5 m example introduced above. For an offset fed antenna, a minimum  $f/D$  of 1.5 is required to generate an acceptable gain and beam shape (see Appendix A). Note that, for our example where  $D = 4.5$  m, this would imply a focal length of 6.75 meters. Such larger structures could rapidly become impractical as the antenna size increases. For axisymmetric designs, a factor of 2 smaller  $f/D$  is required to achieve the same performance – requiring a focal length of 3.4 meters as opposed to 6.75 meters for our example (Ramat-Samii, personal communication). The structure required to support the feeds at this distance in front of the reflector still obviously becomes challenging as the aperture size increases. One approach for reducing the overall length and/or height of the structure is to employ secondary subreflector surfaces. This approach requires additional antenna elements, but allows the beam to focus over a shorter distance, providing for a more compact design. As described in the next subsection, the use of subreflectors appears optimum when large apertures are required.

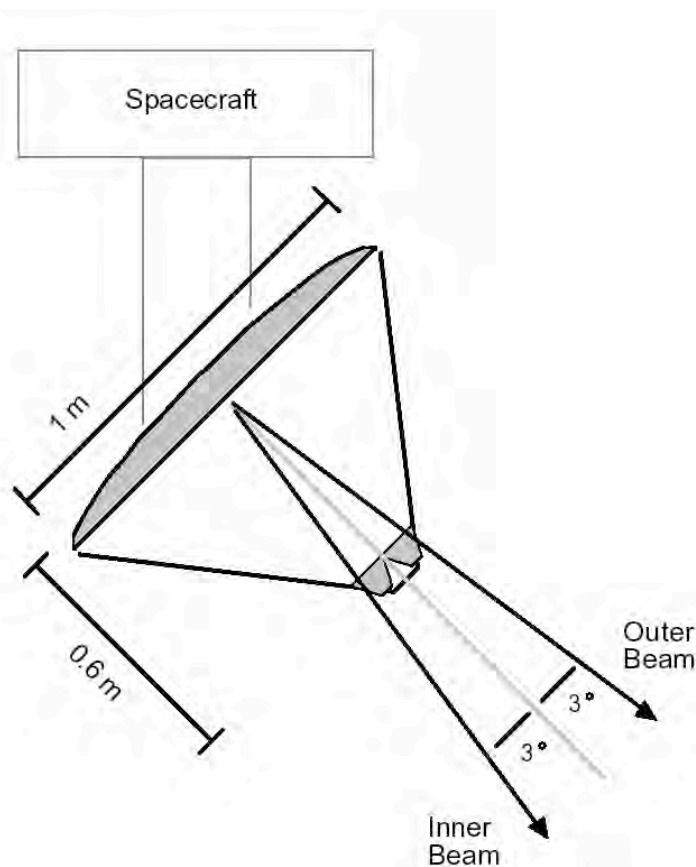


**Figure 6-1: SeaWinds front-fed axisymmetric antenna design showing reflector size, focal length, and scan angles of inner and outer beam.**

*2. Transmit/Receive Separation:* As discussed in Section 5, during the round-trip flight time of the pulse to the surface and back, the antenna beam will rotate away from the pointing direction at the time of transmit. For SeaWinds, this transmit/receive beam separation was a small fraction of the overall beamwidth, and consequently only a small loss in overall gain occurred. As the beamwidth narrows, the altitude increases, or the rotation rate increases, however, this separation can result in a near complete loss of the signal. Previous studies have shown (see Spencer, et al. 2003) that a transmit/receive separation of over 0.5 beamwidths will lead to a significant loss of SNR.

To compensate for beam separation under these circumstances, it will be necessary to use separate beams on transmit and receive. The simplest way to accomplish these separate beams is to use two physically separate feed horns offset in azimuth. Because of the required physical size of the horns, however, there is actually a minimum beam separation that can be accomplished with two separate feeds. In Appendix A, it is shown that the separation between two beams in azimuth must be at least 2.5 beamwidths in order for a good beam shape and gain to be obtained. Smaller separations would require smaller feeds, and the antenna spillover -- and consequently beam degradation -- would be excessive.

For the intermediate case where the separation is too large to use one feed (greater than 0.5 beamwidths) but smaller than that necessary to use two separate feed horns (less than 2-2.5 beamwidths) then some type of overlapping feed design must be used. Such a feed design is described in Appendix A, and utilizes an array of smaller feeds appropriately switched to create either the transmit or receive beams. Such an array feed approach adds significant complexity to the overall antenna design.

*3. Increased Spin Rate, Added Elevation Beams:* As discussed in Section 5, the larger the antenna diameter, the smaller the footprint on the surface (at a given altitude), and the faster the antenna must spin in order to guarantee that footprints from successive scans will overlap in the along-track direction. More rapid antenna spin rates, however, generate a higher angular momentum and larger dynamic disturbances due to residual imbalances. One strategy for reducing the antenna spin rate, also discussed in Section 5, is to place additional beams in the elevation dimension in order to allow for a slower spin rate (see Figure 6-2). Although this strategy lowers the rotation rate, it comes at the expense of additional antenna complexity. For a large antenna such as our 4.5 meter example above, the addition of an elevation beam now means that four feeds are required -- two for transmit and receive, and another set at the additional elevation -- at both the inner and outer swath locations, as opposed to the single feed used by SeaWinds.

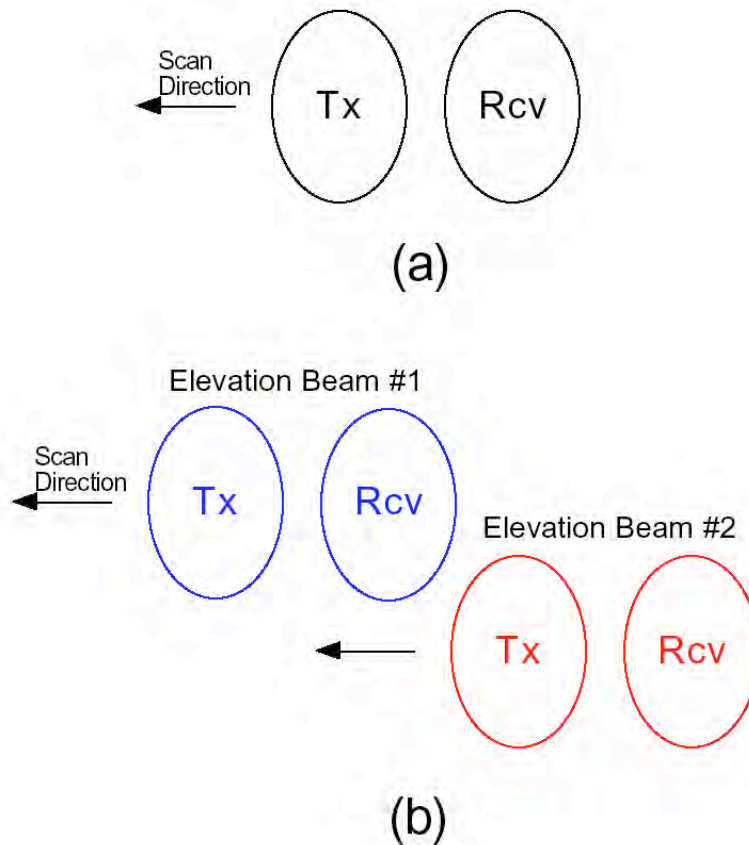


**Figure 6-2: a) Footprints associated with a single elevation beam with separate transmit and receive beams in azimuth, and b) Footprints associated with two elevation beams with separate transmit and receive beams in azimuth.**

## 6.2 Conically-Scanning Antenna Design Options

In Figure 6-3, various reflector antenna design approaches are illustrated. As discussed in the previous subsection, the front-fed axi-symmetric antenna design has the advantage of a relatively short focal length. The structure required to support the feeds in front of the reflector, however, may grow to be prohibitively large as the antenna diameter increases. As the feed support structure grows, so do the lengths of the transmission lines needed to connect the feeds to the radar electronics, increasing loss. It may also be difficult to incorporate a radiometer function into this design because: 1) Excessive losses are incurred in the transmission lines if the radiometer electronics are not located at the feeds, 2) Excessive weight and blockage exist if the radiometers are located at the feeds, 3) Excessive degradation occurs in beam efficiency due to the blockage associated with the feeds and supporting structure. For this study it was concluded that, due to the size of the required feed structure, a front-fed antenna design is not optimum beyond a dish diameter of 2.5 m. Reflectors of this size are easily implemented as solid dishes, typically manufactured from composite material. In Figure 6-4, a 2.5 m, front-fed, solid dish antenna concept produced for this study is shown. Note that the front-fed design



easily lends itself to being mounted on the nadir facing side of the spacecraft, similar to the manner in which SeaWinds was mounted.

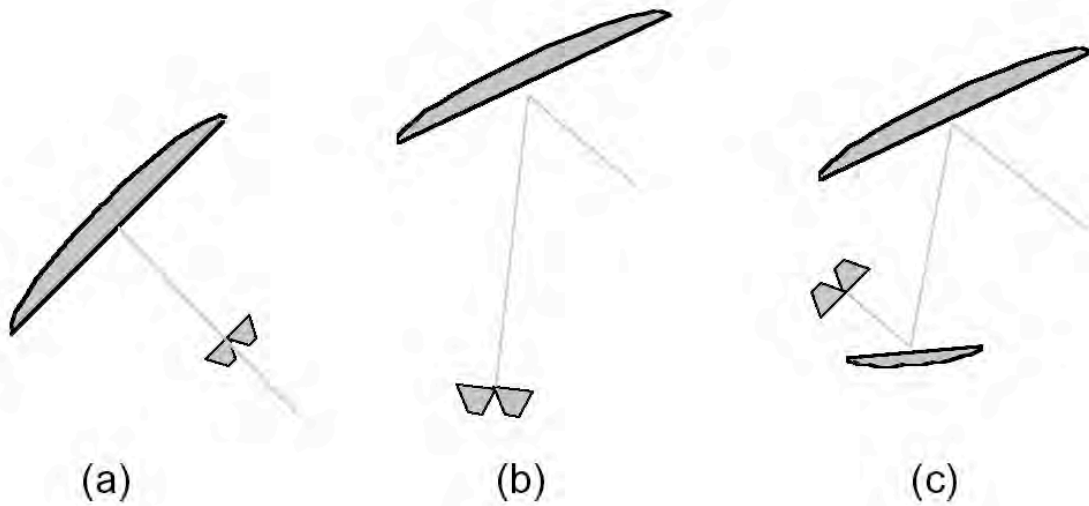


**Figure 6-3: Antenna design concepts: a) Front-fed axi-symmetric, b) Offset fed, c) Offset fed with sub-reflector(s).**

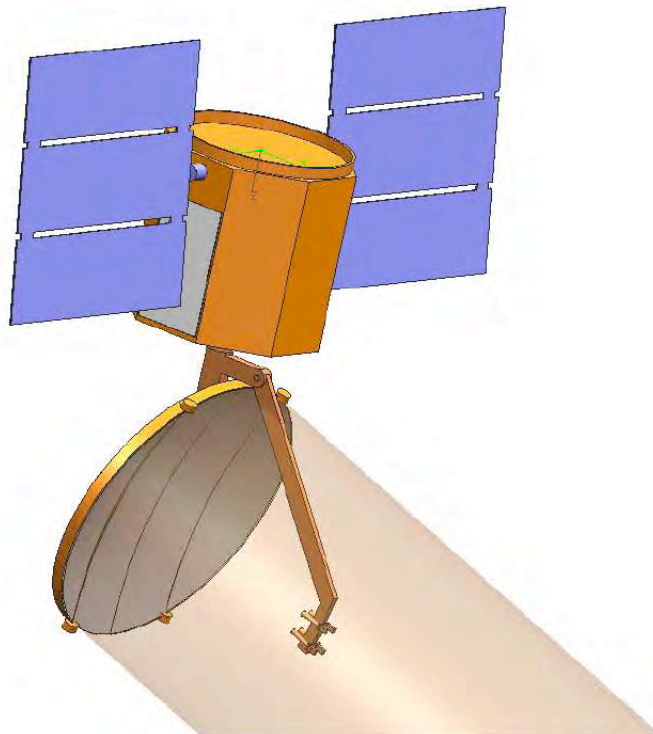


**Figure 6-4: Design example for a 2.5 m, solid dish, front-fed, axi-symmetric antenna mounted on the spacecraft nadir side.**

For offset fed antennas, the focal length required is considerably longer (see Appendix A). For these antennas, there is no obstruction due to the feeds or associated support structure. The offset feed design is the standard approach for spaceborne radiometer instruments (i.e., SSM/I, WindSAT, etc.). This architecture lends itself to being mounted on the zenith deck of the spacecraft, which allows the feeds to be positioned close to the spacecraft structure rather than being supported some distance away. The primary disadvantage of the zenith deck mounting approach is that a  $360^\circ$  field of view must be maintained around the nadir direction to allow an unobstructed conical scan of the surface. As mentioned in the previous subsection, offset antennas require a relatively long focal length in order to achieve the desired beam quality. As the antenna diameter increases, this can lead to quite a long structure.

In Figure 6-5, an example zenith-mounted offset design is shown where the reflector diameter is 4.5 meters. Note the relatively long structural elements needed to achieve the required focal length. The large reflector must be deployable in order to fit within the spacecraft launch fairing. A high-heritage, light-weight approach to such antennas is to use a gold-plated molybdenum mesh material, appropriately shaped by a deployable supporting structure. Such designs have been used on communications satellites since the 1970's, and have been demonstrated up to Ku-Band (see Njoku et al. 2001).

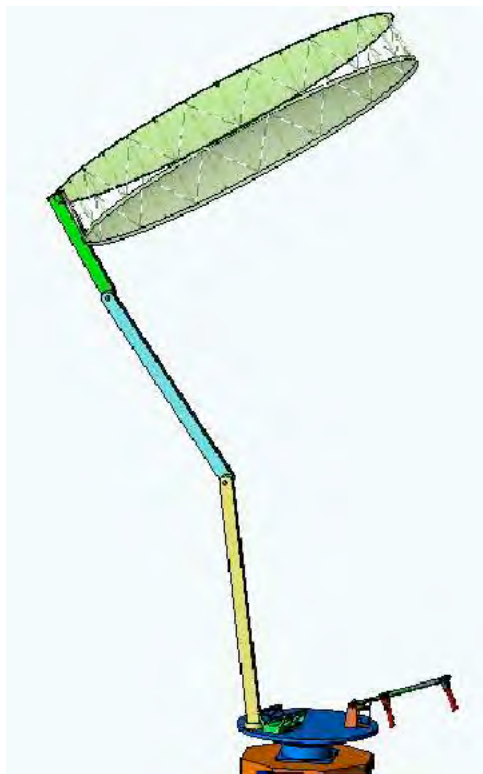


**Figure 6-5: Example 4.5 m, zenith-deck mounted, offset-fed antenna. Note long structure required to accommodate 6.75 m focal length necessary to obtain good beam quality.**

When one or more subreflectors are employed with a parabolic primary reflector, a design is achieved that incorporates the advantages of both the front-fed and offset-fed approaches. Because the antenna is still inherently an offset design, there is no structural blockage and the feeds can be placed near the spacecraft when the antenna is zenith-deck mounted. Like the axi-symmetric approach, subreflector(s) allow a much more compact antenna structure. The optimal design for large antennas was found to be the use of two subreflectors – one each to bring the inner and outer beams to focus at the desired location. This design is illustrated for the case of a 4.5 meter reflector in Figure 6-6. Note that, again, the large reflector diameter dictates the use of a deployable mesh antenna approach. This design also has the advantage that, as the aperture size grows, all elements of the antenna (subreflectors, structural dimensions, etc.) are scaled proportionately. This is in contrast to the offset fed case where, as the aperture size increases, the focal length needs to be scaled more than the proportionality factor because the  $f/D$  also must increase with increasing diameter in order to form an acceptable beam.

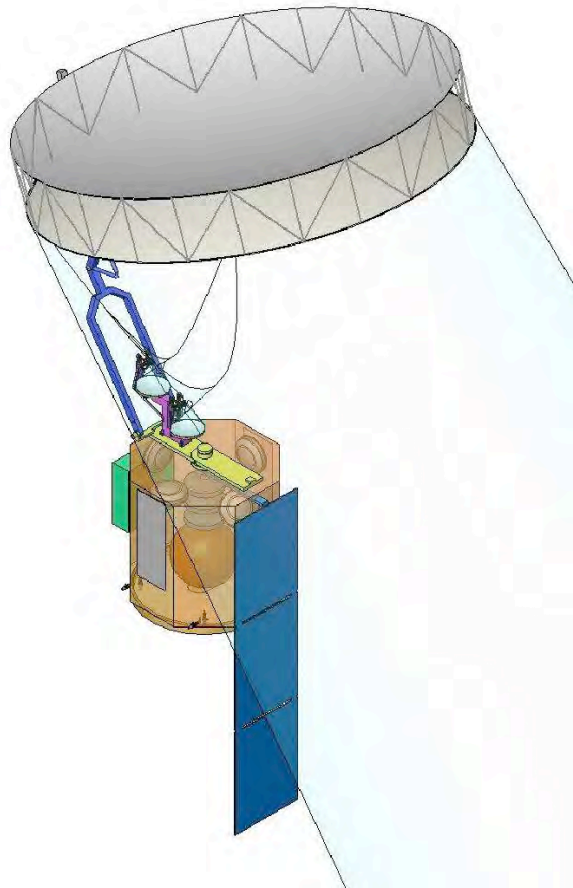


**Figure 6-6: 4.5 m dual-subreflector, offset antenna design. Note the more compact length relative to the simple offset design in Figure 6-5.**

### 6.3 References

Njoku, E. Wilson, W., Yueh, S., Freeland, R., Helms, R., Edelstein, W., Sadowy, G., Farra, D., West, R., Oxvenad, K., Campbell, T., Lawrence, W., Rahmat-Samii, Y., Feingold, H., Didinsky, G., Rauwolf, J., Thompson, M., Konicke, G., "Spaceborne Microwave Instrument for High Resolution Remote Sensing of Earth's Surface Using a Large-Aperture Mesh Antenna," JPL Publication 01-09, September 2001.

Spencer, M.W., Tsai, W., and Long, D.G., "High-Resolution Measurements With a Spaceborne Pencil-Beam Scatterometer Using Combined Range/Doppler Discrimination Techniques," *IEEE Trans. Geo. Sci. and Remote Sens.*, Vol. 41, No. 3, March 2003.

## **7. Summary, Conclusions, and Recommendations**

### **7.1 Study Summary**

In this study, the “trade-space” of advanced scatterometer concept options to operate in the post-SeaWinds era has been described. Drawing upon published requirements and other existing documentation, a preliminary set of wind measurement goals designed to meet the future needs of both scientific and operational communities has been put forth. In brief, these goals call for improved scatterometer capability in the areas of temporal revisit, spatial resolution, and the ability to measure winds under high-wind and/or rainy conditions.

Design constraints governing allowable scatterometer measurement frequencies, azimuth geometries, and incidence angles were established. The measurement duration was identified as a key measurement constraint not considered in previous scatterometer studies. As higher altitudes are considered for future scatterometers, the length of time it takes to collect all the azimuth measurements necessary to retrieve the wind vector also increases. The de-correlation of the surface wind from the first azimuth measurement to the last azimuth measurement becomes a limiting factor on the maximum altitude at which a scatterometer can operate.

A survey of potential scatterometer antenna architectures was performed. It was concluded that the architecture with the widest range of performance advantages is the conically-scanning pencil-beam reflector concept. A thorough analysis of the design issues associated with conically-scanning scatterometers was presented, including an analysis of how the design parameters must change as a function of altitude. As the antenna size grows to compensate for higher altitude or to achieve higher resolution, significant antenna design challenges are encountered. Strategies for dealing with these antenna design challenges were presented.

A primary focus of this study has been the investigation of higher, medium earth orbit (MEO) altitudes to improve the temporal revisit time. To this end, a detailed study of the revisit time associated with a single satellite in a variety of different orbits was performed. A key finding was that, in general, revisit statistics improve rapidly up to an altitude of 1500 km, then level-out thereafter. Orbital inclination can be adjusted to perform trade-offs between average revisit time and the portion of the Earth covered. Ultimately, however, it was determined that no single-satellite scatterometer system can simultaneously achieve full ocean coverage (to  $\pm 70^\circ$  latitude) and provide regular samples at 6-hour intervals. It was briefly demonstrated how constellations of satellites could meet this requirement. Lastly, the issue of radiation environment as a function of altitude and inclination was addressed. The severity of the radiation environment was shown to vary significantly throughout the MEO range of interest, with relatively mild conditions prevailing below 1500 km.

## 7.2 Recommendations for Future Work

As stated in the introduction, this Phase-I report is intended to be an initial study to “flesh out” the high-level design issues associated with an advanced scatterometer system. During this study, certain key areas were identified for future work in order to further develop a MEO scatterometer system:

*Science and Operational Requirements:* In this report, a general set of wind measurement goals designed to meet the future needs of the scientific and operational communities was adopted. As stated, these goals were derived purely from existing requirements documentation and position papers, with only informal clarification being provided by a few members of the science and operational communities. In order to move forward with a next generation scatterometer concept, a more formal, more authoritative, more detailed development of science requirements should be performed by the science/operational community itself. These requirements would then serve as input to the next level engineering design studies, and, ultimately, to a down-selection process where a specific scatterometer mission concept is selected for development.

*Measurement Duration:* In this report, limits on the allowable scatterometer measurement duration were developed from a “rule-of-thumb” analysis based on a simple motion blurring argument and a single value for the wind feature advection speed (10 m/s). The result of this preliminary analysis suggested a rather severe limitation on allowable altitudes, particularly when high resolution measurements are desired. Due to the complex nature as well as the criticality of this requirement, it is recommended that more detailed analysis be performed to address this issue. Such analysis should consider the actual spatial and temporal behavior of surface wind features under a range of different conditions, and in a variety of different geographic locations.

*Optimal Channel Suite:* In Section 2, the allowable scatterometer frequencies, and their associated advantages and disadvantages were described. Also, the potential for passive radiometer channels for improving the wind direction accuracy and correcting for the presence of rain was discussed. What was not evaluated was the *optimal* set of scatterometer and radiometer channels to achieve a given level of wind measurement performance. It is recommended that a detailed study be performed to investigate the wind retrieval performance as a function of which active/passive measurement channels are implemented. Such an investigation should use the well-established Ku-Band and C-Band scatterometer model functions, in addition to the data recently returned from the AMSR radiometer aboard ADEOS-II and the Windsat mission.

*Synthetic Aperture Processing for High Resolution:* In Section 5, it was shown how, in theory, synthetic aperture radar (SAR) processing could be applied to a conically scanning scatterometer system in order to obtain backscatter at a resolution significantly higher than that allowed by the real-aperture limit. This analysis was performed using idealized antenna patterns and certain simplifying assumptions. To fully demonstrate the potential of adapting SAR techniques to wind scatterometry, more detailed modeling and analysis must be performed. It is recommended that a point target simulator that includes

all the effects associated with a continuously rotating antenna be constructed and used for this purpose.

*RF Design for Large Reflector Antennas:* In Sections 5 and 6, the RF design complexities associated with large, rotating reflector antennas were introduced. These issues included the formation of multiple beams to make measurements at different incidence angles on the surface, the necessity of having separately steered transmit and receive beams to compensate for the effect of rotation, and the inclusion of multiple elevation beams to allow for slower rotation rates. Reflector concepts capable of meeting these requirements were identified, but no detailed antenna designs were developed for this report. Future work should further mature the candidate antenna designs, leading to the generation of full antenna patterns to confirm the acceptability of the various implementation options.

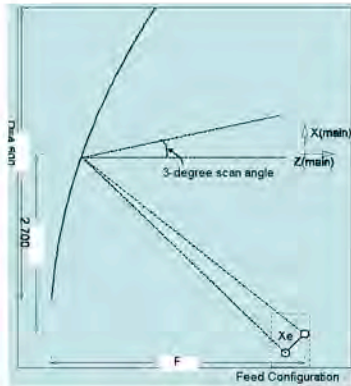
*Dynamics of Large Spinning Antenna Structures:* As discussed throughout this study, in order to operate at higher orbits or to achieve higher resolution, the antenna size must increase. For rotating reflector antennas, an increase in antenna size leads to an increase in angular momentum, and an increase in the magnitude of the disturbances imparted to the spacecraft. As a critical part of future work, the overall rotational dynamics associated with large spinning scatterometer antennas should be studied. The feasibility of implementing large deployed antennas should be evaluated as a function of antenna size and spin rate.

## **Appendix A**

On the following pages, charts from a study performed by Dr. Yahya Ramat-Samii are presented. This study evaluates how the inner and outer beam patterns for an example 4.5 m offset reflector change as a function of focal length. Another issue addressed is how closely spaced the separate transmit and receive beams can be constructed using a simple feed horn. When the beams are too close to be implemented with separate feed horns, an overlapping array-type feed is considered.



# Various Design Options for 4.5 m Offset Parabolic Reflector Antenna: MeoSat Project

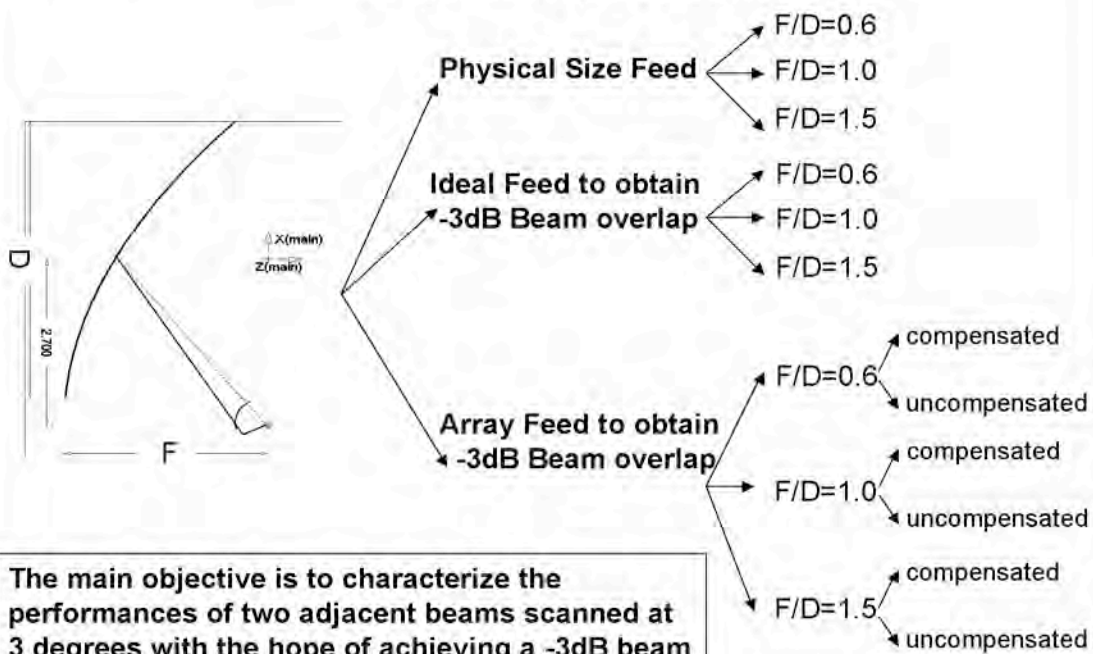


**Yahya Rahmat-Samii**

[rahmat@ee.ucla.edu](mailto:rahmat@ee.ucla.edu)

November 17, 2003

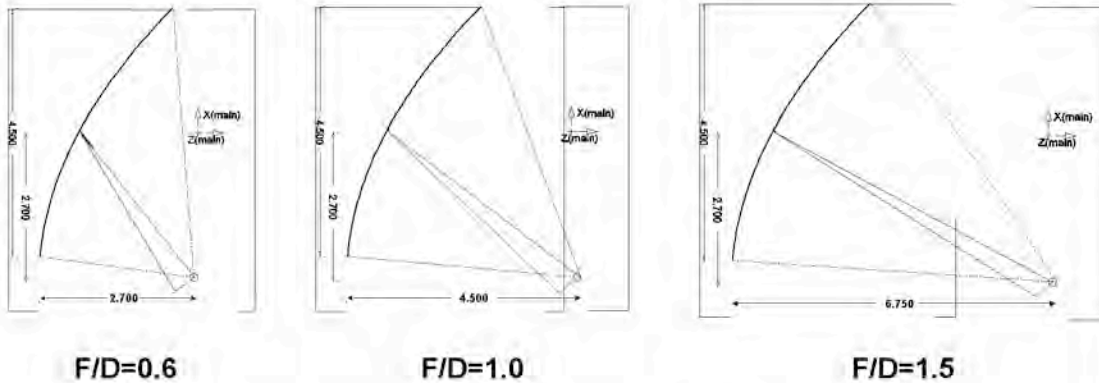
## 4.5 meter Offset Parabolic Reflector (Ku Band, 13.6GHz): Various Design Options



The main objective is to characterize the performances of two adjacent beams scanned at 3 degrees with the hope of achieving a -3dB beam overlap. Many options have been considered.

YRS-2003

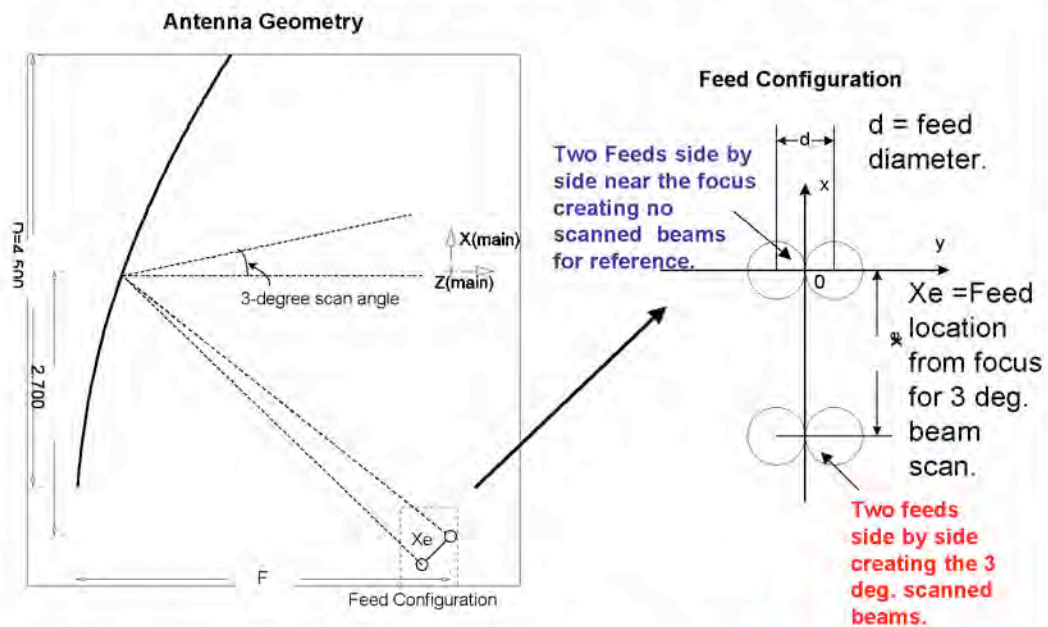
## 4.5 meter Offset Parabolic Reflector (Ku Band, 13.6GHz): Reflector Configuration versus F/D's



**Note:** As F/D gets larger the feed subtended angle becomes smaller.  
Larger physical feeds are required for a given edge taper.

YRS-2003

## 4.5 meter Offset Parabolic Reflector – Feed Configuration



**Challenge:** To obtain 3-degree scan angle and -3-dB beam overlap with acceptable overall antenna directivity.

YRS-2003

## Feed Patterns with Various Edge Tapers

- (a) **Physical size feed:** In order to maximize the antenna directivity at Ku band, -10 dB edge tapered feed illumination were used. In all cases the simple  $\cos^q$  feed pattern models were applied. In the future one may use an actual feed configurations. Due to the limited duration of this project, the actual feed options were not considered.
- (b) **Ideal feed/Array cluster:** Small size feed to allow -3 db beam overlaps for two adjacent feed. In this case also  $\cos^q$  feed pattern is used. Here  $q$  is smaller than the physical size feed case. These small feeds are also used as elements of the 7-element array feed cluster.

YRS-2003

## Computational Methodology

There are many different numerical techniques that can be used to analyze the radiation performance of reflector antennas. In this report the Physical Optics (PO) method is used for the analysis of the reflector antenna system.

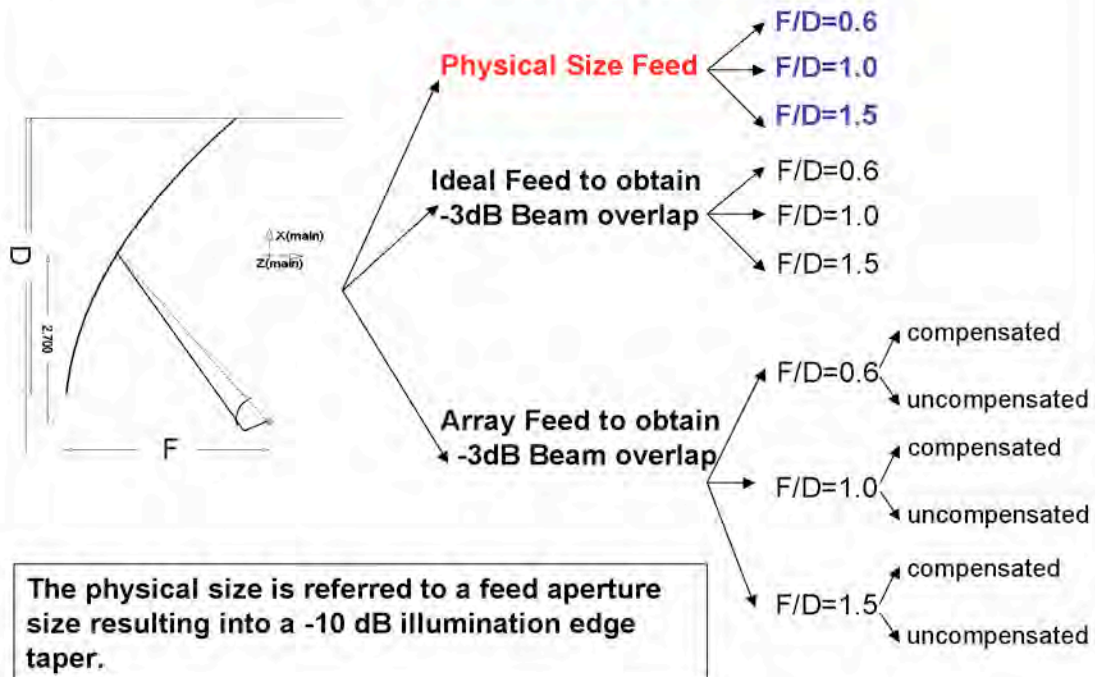
Physical optics has been a primary technique used to analyze reflector antenna performance. This method assumes that the induced current on the reflector equals twice the tangential component of the incident magnetic fields over the illuminated region and then performs numerical integration of the vector potential integral.

YRS-2003



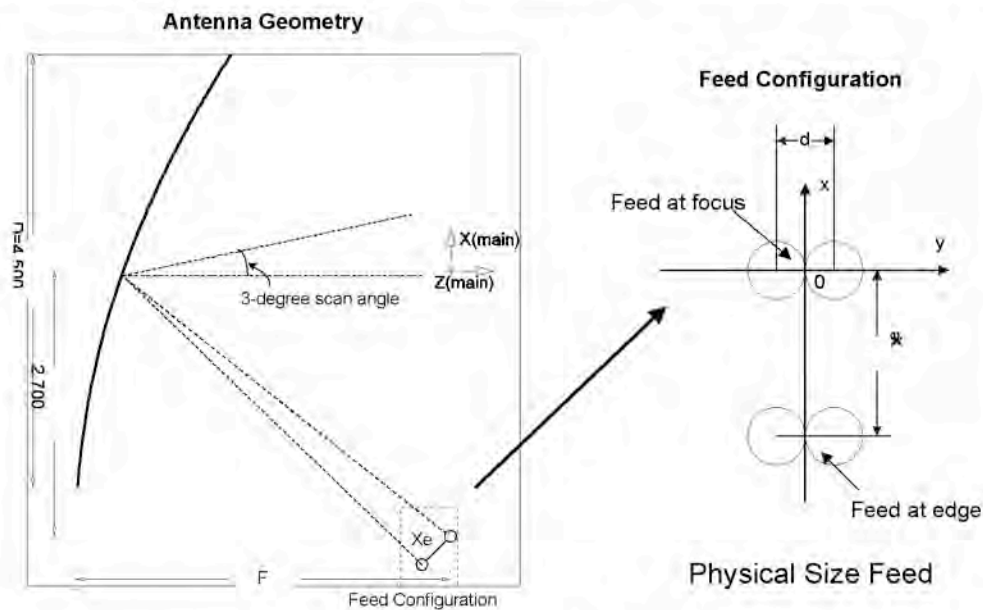
## 4.5 meter Offset Parabolic Reflector (Ku Band, 13.6GHz):

### Various Design Options



YRS-2003

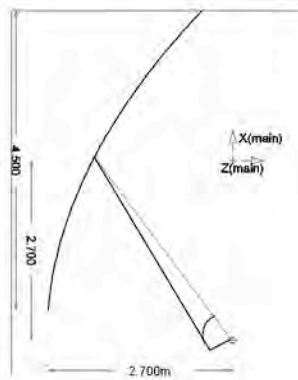
## 4.5 meter Offset Parabolic Reflector – Physical Size Feed



**Challenge:** To obtain 3-degree scan angle and -3-dB overlap at the same time.

YRS-2003

## 4.5 meter Offset Parabolic Reflector – Physical Size Feed

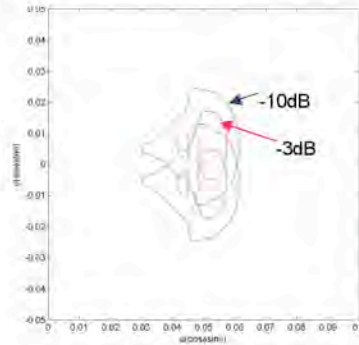
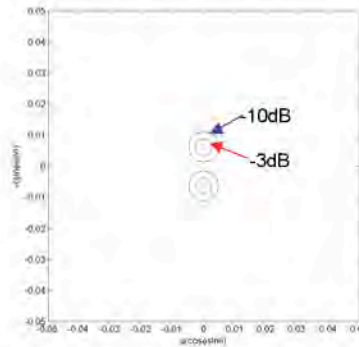


$$F/D=0.6$$

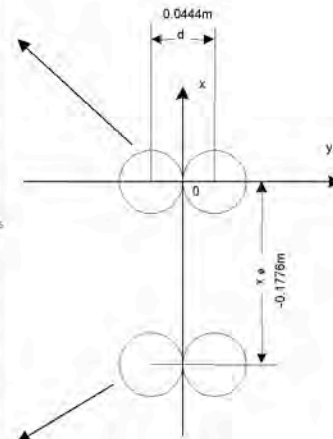
$$d=0.0444\text{m}, X_e=-0.1776\text{m},$$

$$q_x=q_y=4.73$$

$q_x=q_y$  = Parameters to define feed pattern for  $\cos^*q$  model.



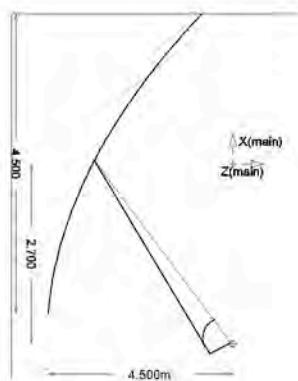
Directivity=54.87(dB)  
Beamshift=0(deg)



Directivity=45.60(dB)  
Beamshift=3.04(deg)

YRS-2003

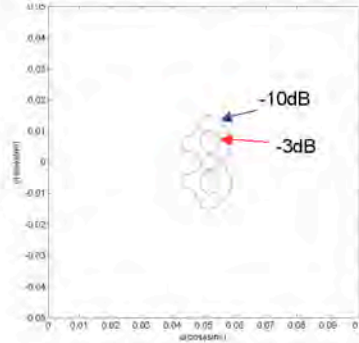
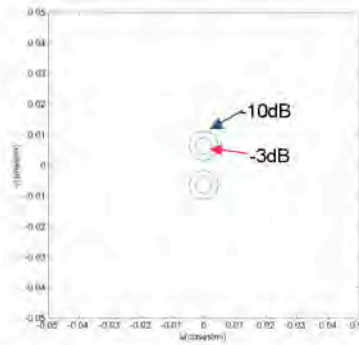
## 4.5 meter Offset Parabolic Reflector – Physical Size Feed



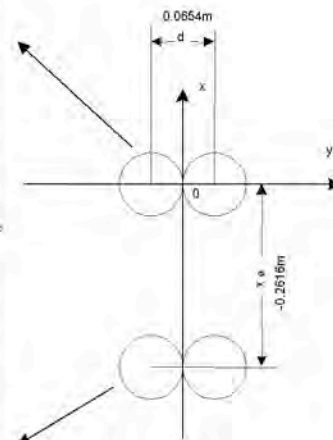
$$F/D=1.0$$

$$d=0.0654\text{m}, X_e=-0.2616\text{m},$$

$$q_x=q_y=10.83$$



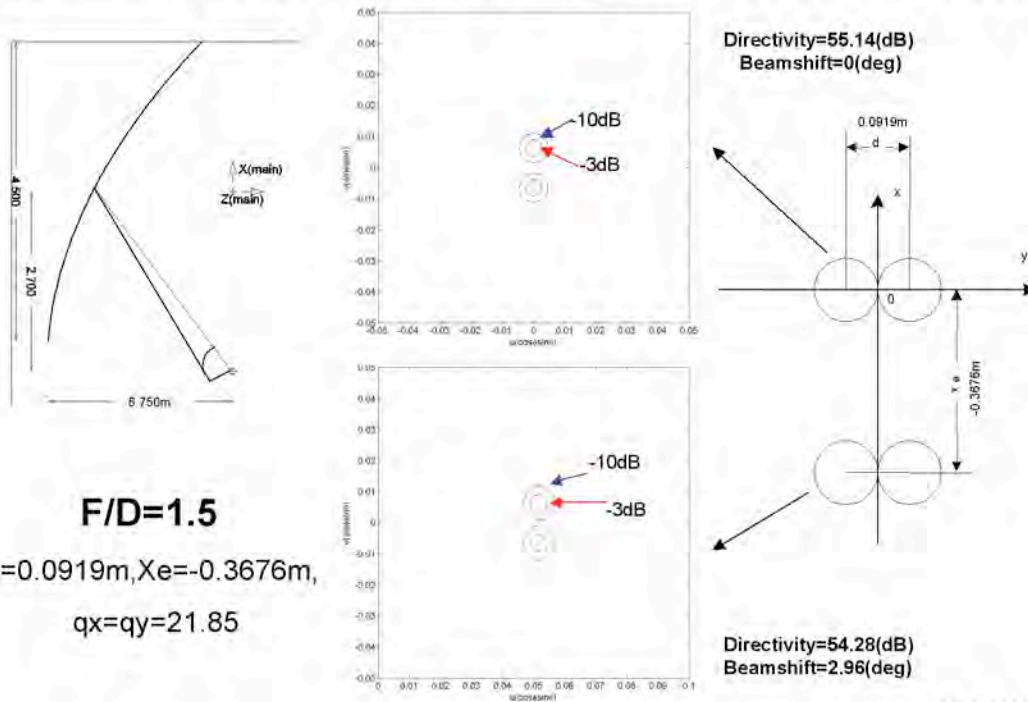
Directivity=55.09(dB)  
Beamshift=0(deg)



Directivity=52.00(dB)  
Beamshift=2.96(deg)

YRS-2003

## 4.5 meter Offset Parabolic Reflector – Physical Size Feed



YRS-2003

## 4.5 meter Offset Parabolic Reflector – Physical Size Feed

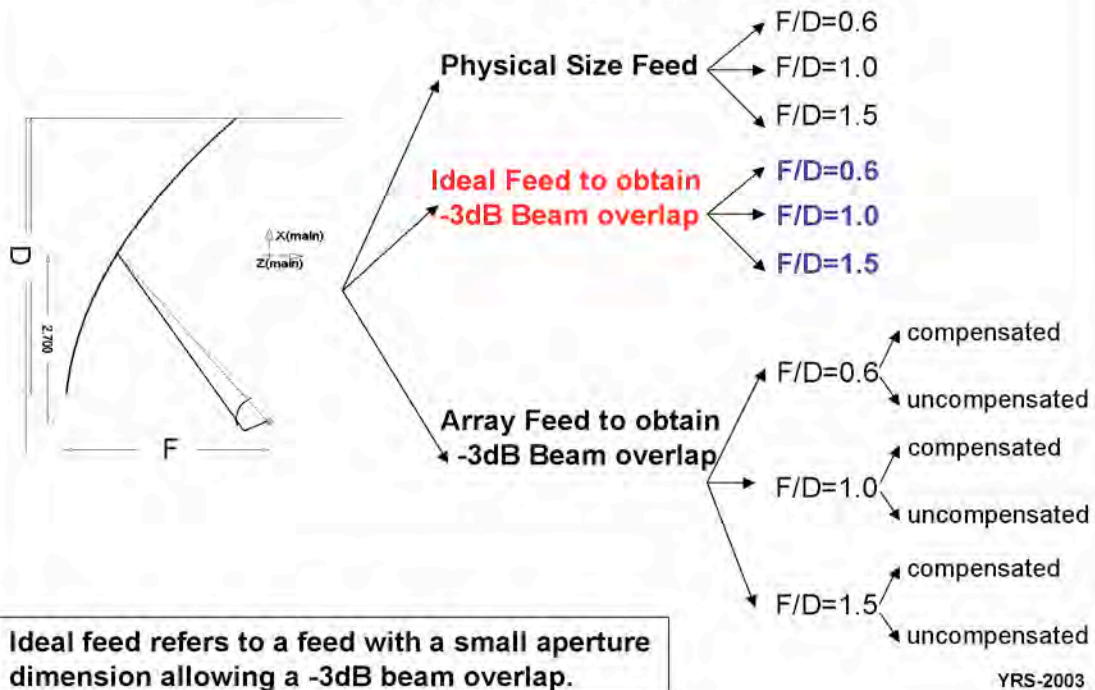
### By applying Physical Size Feed:

- 3-degree scan angle is achieved.
- No -3-dB beam overlap is observed. The actual overlap depends on the  $F/D$ .
- Larger  $F/D$ 's improves the quality of the 3-deg. scanned beams.  $F/D = 1.5$  is needed for a clean scanned beam.

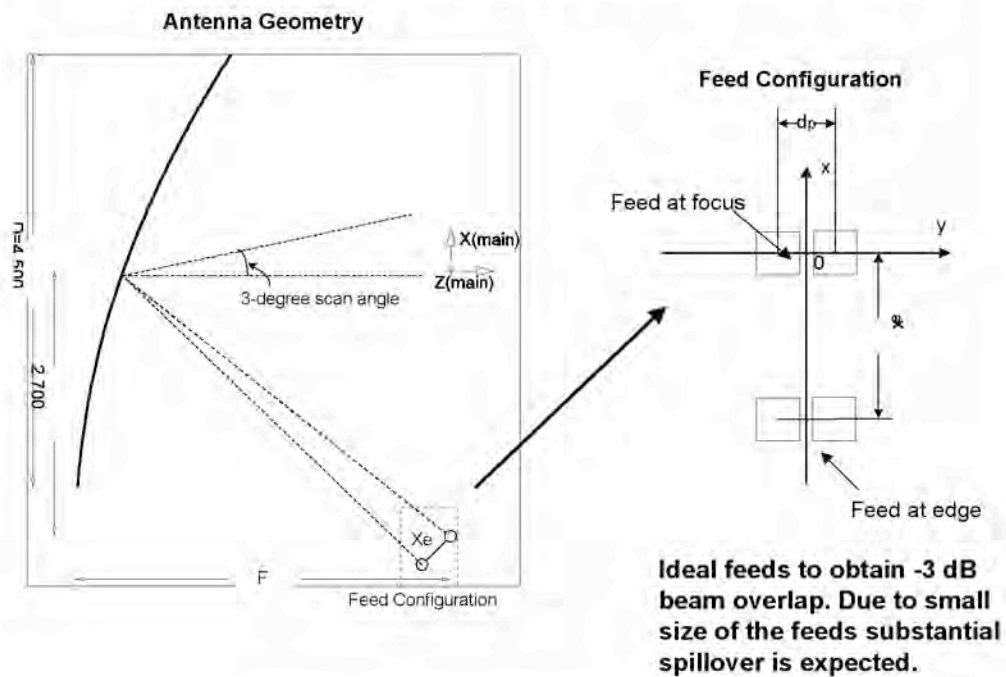
YRS-2003

## 4.5 meter Offset Parabolic Reflector (Ku Band, 13.6GHz):

### Various Design Options

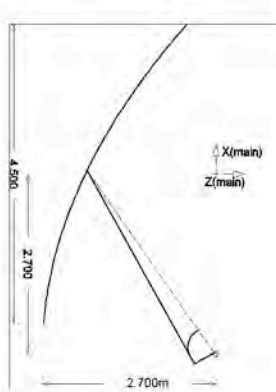


## 4.5 meter Offset Parabolic Reflector – Ideal Feed



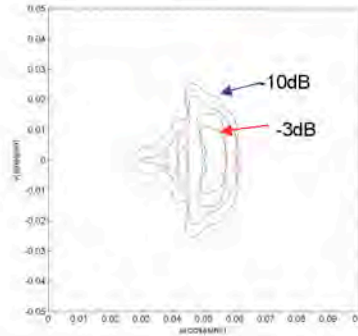
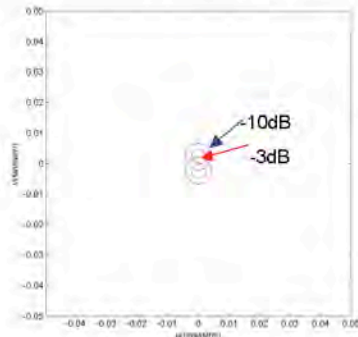


## 4.5 meter Offset Parabolic Reflector – Ideal Feed

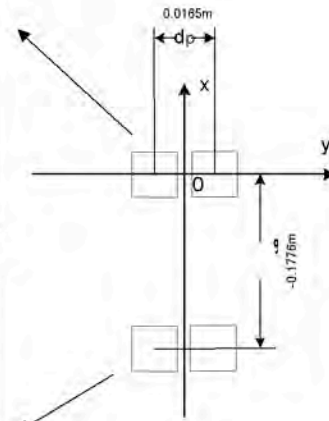


**F/D=0.6**

$d=0.0165\text{m}$ ,  $X_e=-0.1776\text{m}$ ,  
 $q_x=0.8$ ,  $q_y=1.1$



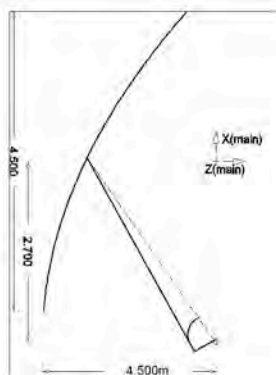
Directivity=52.70(dB)  
Beamshift=0(deg)



Directivity=42.15(dB)  
Beamshift=3.04(deg)

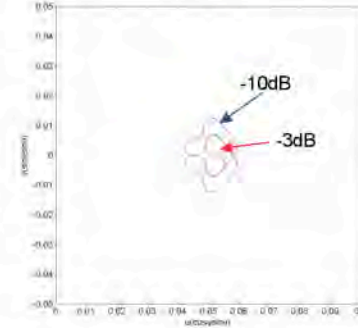
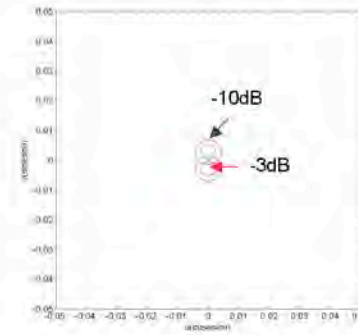
YRS-2003

## 4.5 meter Offset Parabolic Reflector – Ideal Feed

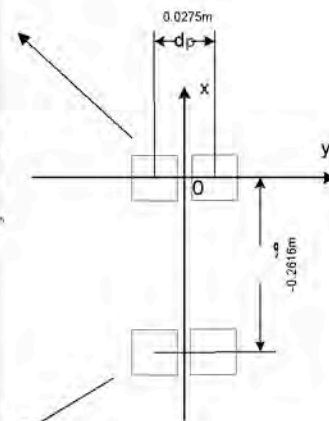


**F/D=1.0**

$d=0.0275\text{m}$ ,  $X_e=-0.2616\text{m}$ ,  
 $q_x=2.2$ ,  $q_y=2.2$



Directivity=52.24(dB)  
Beamshift=0(deg)

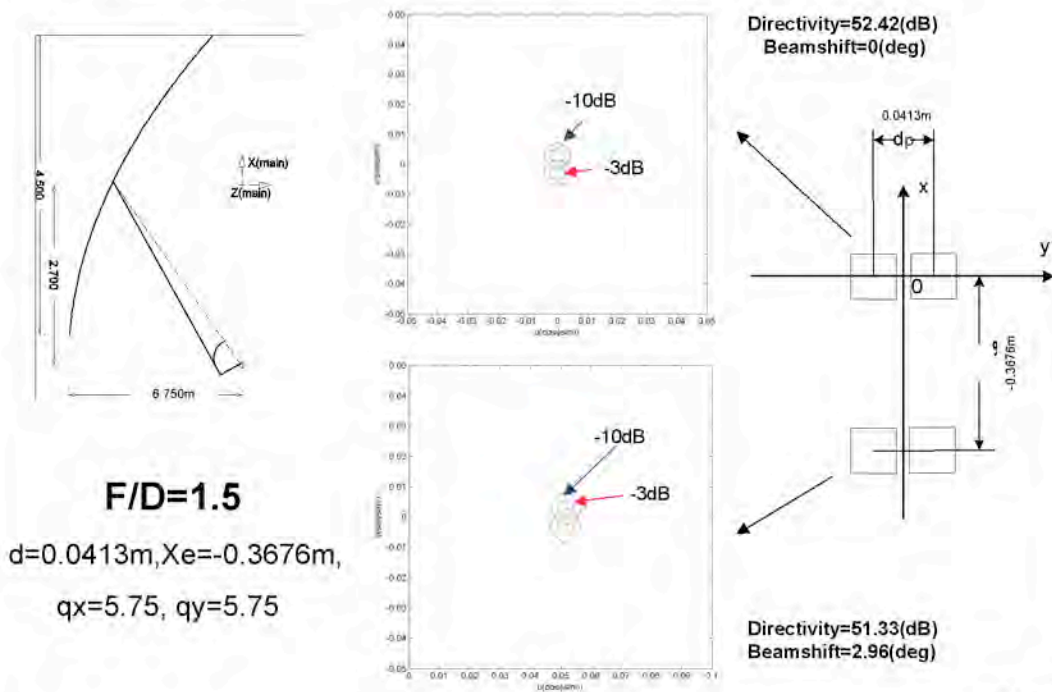


Directivity=48.23(dB)  
Beamshift=2.96(deg)

YRS-2003



## 4.5 meter Offset Parabolic Reflector – Ideal Feed



YRS-2003

## 4.5 meter Offset Parabolic Reflector – Ideal Feed

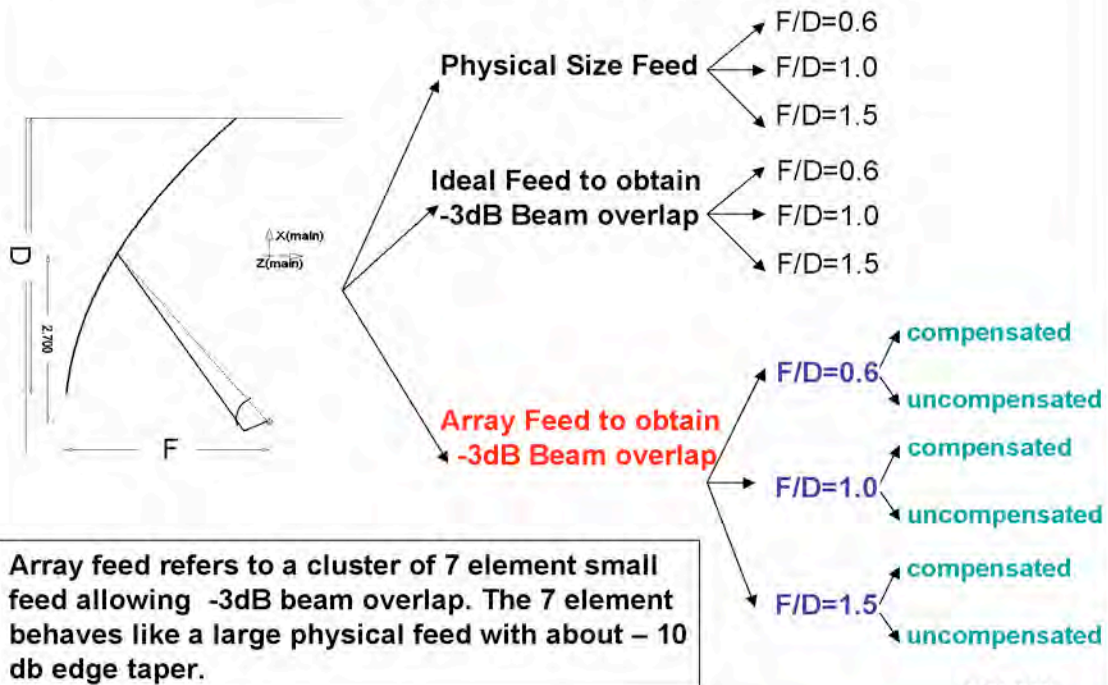
### By applying Ideal Feed:

- 3-degree scan angle is achieved.
- 3-dB beam overlap is obtained.
- Excessive directivity loss due to the small size of the ideal feed resulting into unaccepted amount of spillover.
- Larger F/D's improves the quality of the 3-deg. scanned beams. F/D=1.5 is needed for a clean scanned beam.

YRS-2003

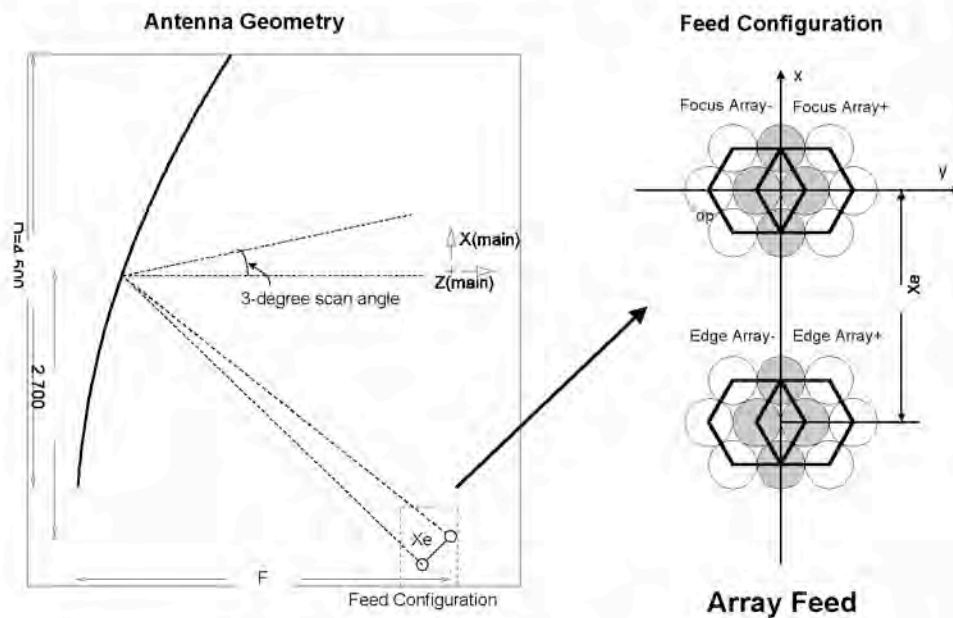
## 4.5 meter Offset Parabolic Reflector (Ku Band, 13.6GHz):

### Various Design Options



YRS-2003

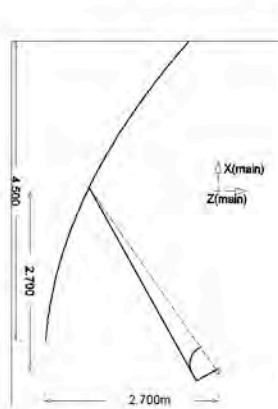
## 4.5 meter Offset Parabolic Reflector – Array Feed



Note: The 7-element overlap array feed generates -3db beam overlap.

YRS-2003

## 4.5 meter Offset Parabolic Reflector – Array Feed

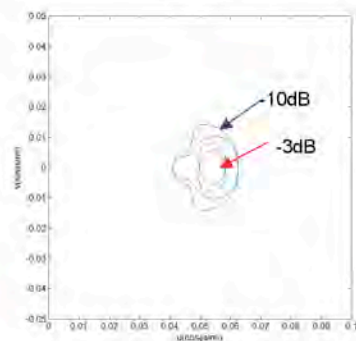
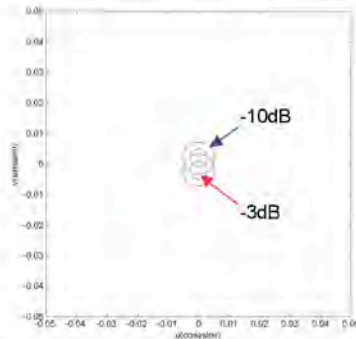


$$F/D=0.6$$

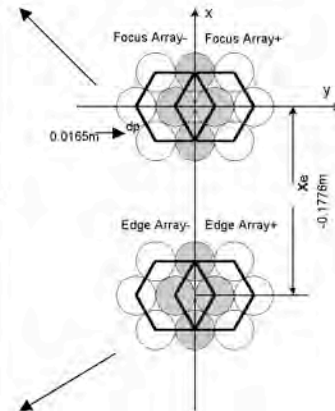
$$d=0.0165\text{m}, X_e=-0.1776\text{m},$$

$$q_x=0.8, q_y=1.1$$

Phase Compensated



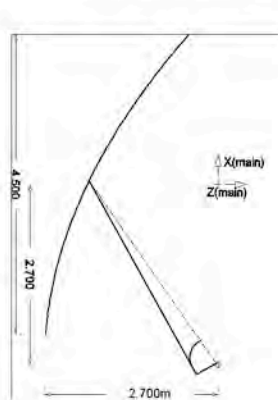
Directivity=54.64(dB)  
Beamshift=0(deg)



Directivity=48.49(dB)  
Beamshift=3.04(deg)

YRS-2003

## 4.5 meter Offset Parabolic Reflector – Array Feed

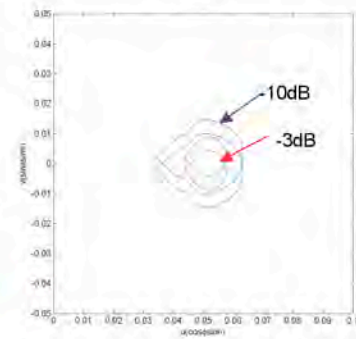
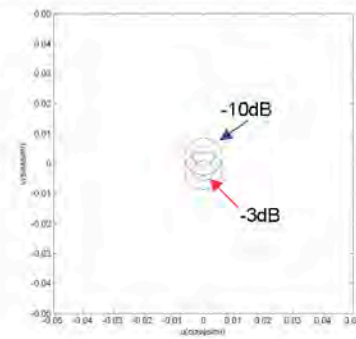


$$F/D=0.6$$

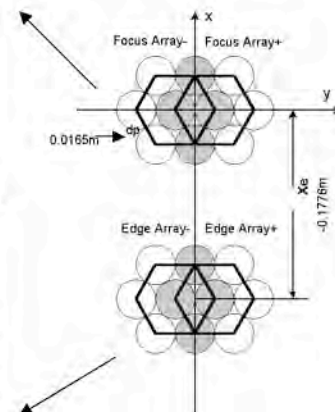
$$d=0.0165\text{m}, X_e=-0.1776\text{m},$$

$$q_x=0.8, q_y=1.1$$

Phase Uncompensated



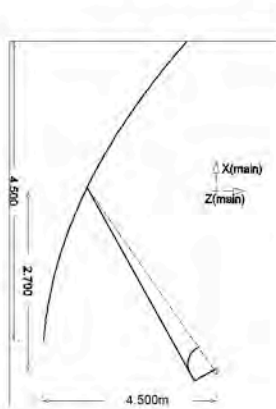
Directivity=52.85(dB)  
Beamshift=0(deg)



Directivity=47.34(dB)  
Beamshift=3.04(deg)

YRS-2003

## 4.5 meter Offset Parabolic Reflector – Array Feed

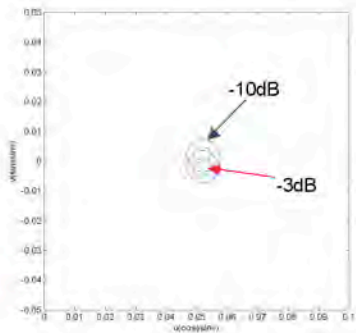
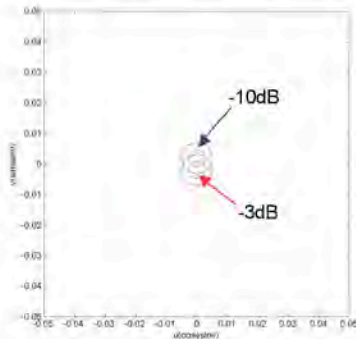


**F/D=1.0**

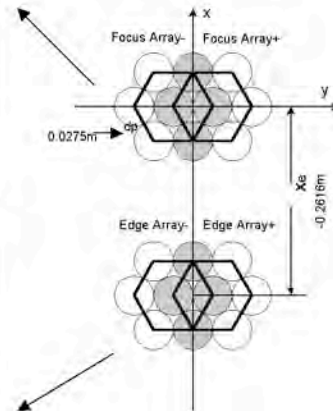
$d=0.0275\text{m}$ ,  $X_e=-0.2616\text{m}$ ,

$q_x=2.2$ ,  $q_y=2.2$

**Phase Compensated**



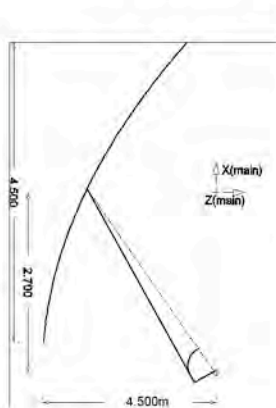
Directivity=52.92(dB)  
Beamshift=0(deg)



Directivity=52.25(dB)  
Beamshift=2.96(deg)

YRS-2003

## 4.5 meter Offset Parabolic Reflector – Array Feed

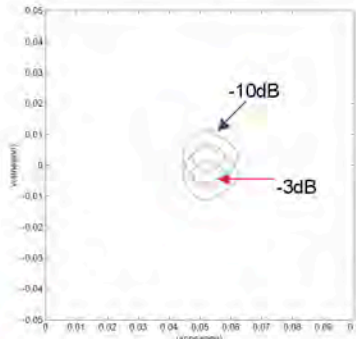
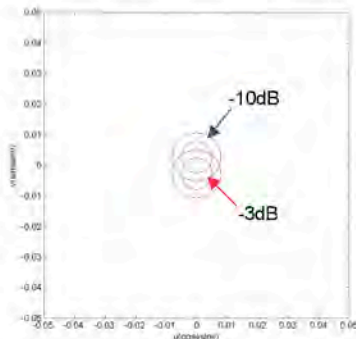


**F/D=1.0**

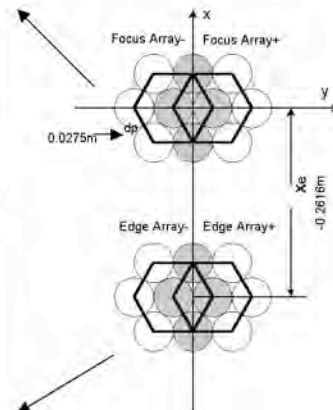
$d=0.0275\text{m}$ ,  $X_e=-0.2616\text{m}$ ,

$q_x=2.2$ ,  $q_y=2.2$

**Phase Uncompensated**



Directivity=48.87(dB)  
Beamshift=0(deg)

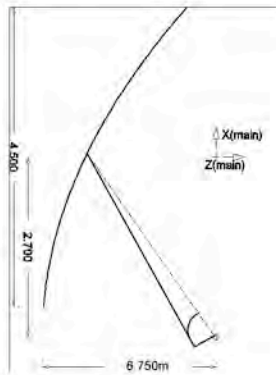


Directivity=48.99(dB)  
Beamshift=2.96(deg)

YRS-2003



## 4.5 meter Offset Parabolic Reflector – Array Feed

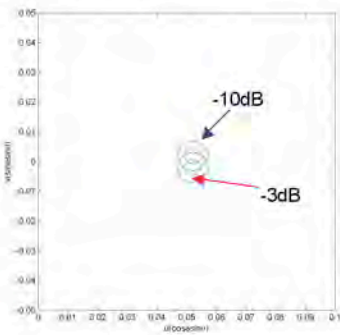
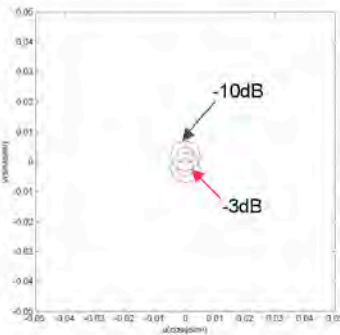


**F/D=1.5**

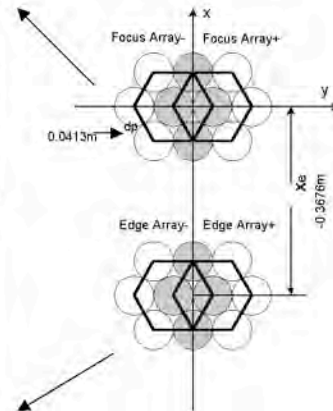
$d=0.0413\text{m}$ ,  $X_e=-0.3676\text{m}$ ,

$q_x=5.75$ ,  $q_y=5.75$

**Phase Compensated**



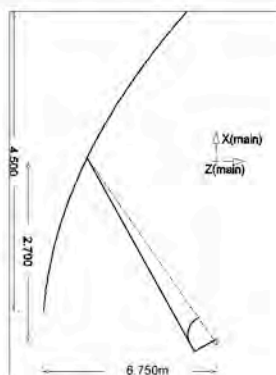
Directivity=52.63(dB)  
Beamshift=0(deg)



Directivity=52.43(dB)  
Beamshift=2.96(deg)

YRS-2003

## 4.5 meter Offset Parabolic Reflector – Array Feed

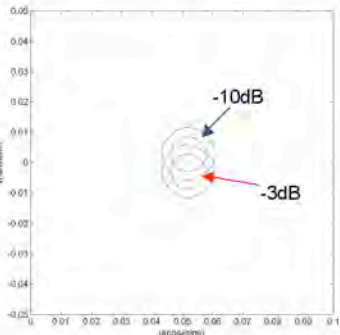
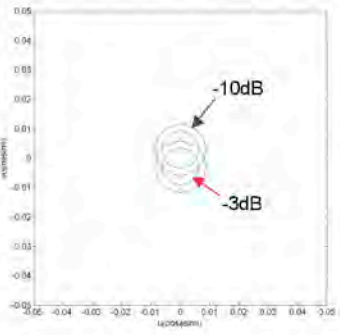


**F/D=1.5**

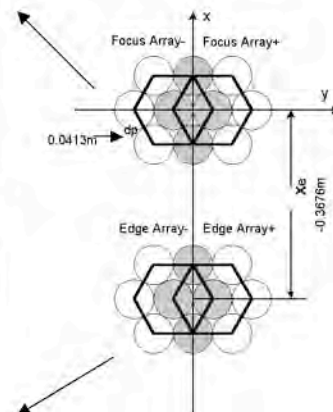
$d=0.0413\text{m}$ ,  $X_e=-0.3676\text{m}$ ,

$q_x=5.75$ ,  $q_y=5.75$

**Phase Uncompensated**



Directivity=47.05(dB)  
Beamshift=0(deg)



Directivity=47.53(dB)  
Beamshift=2.96(deg)

YRS-2003

## **4.5 meter Offset Parabolic Reflector – Array Feed**

### **By applying array Feed:**

- . 3-degree scan angle is achieved.
- . -3dB beam overlap is obtained.
- . Relatively high directivity and less beam distortion.
- . Overall improved performance is observed using phase compensated array.
- . Larger F/D's improves the quality of the 3-deg. scanned beams. F/D=1.0 provided good results.
- . DSP implementation of the array approach requires further study.

YRS-2003